Transverse Mass and Rapidity Spectra of Pions and Protons from Au+Au Collisions at the Alternating Gradient Synchrotron

BY

Jennifer Lynn Klay

B.S. (University of California, Los Angeles) 1994

M.S. (University of California, Davis) 1998

DISSERTATION

Submitted in partial satisfaction of the requirements for the degree of

DOCTOR OF PHILOSOPHY

in

Physics

in the

OFFICE OF GRADUATE STUDIES

of the

UNIVERSITY OF CALIFORNIA

DAVIS

Approved:

_____

_____

_____

Committee in Charge

2001

i

Jennifer Lynn Klay
June 2001
Physics

Transverse Mass and Rapidity Spectra of Pions and Protons from Au+Au Collisions at the Alternating Gradient Synchrotron

Abstract

Relativistic Heavy Ion Collisions allow earth-bound scientists to study the dynamics of the hot, dense nuclear matter found in astrophysical environments such as neutron stars, supernova explosions and the early universe. Systematic studies of the particles emerging from these collisions carry global information about the nature and dynamical evolution of the interaction region. By reconstructing the final state momentum spectra of observed particles such as pions and protons, information about the collision dynamics may be inferred.

For this dissertation, pion and proton transverse mass and rapidity spectra from fixed target Au+Au collisions at the Alternating Gradient Synchrotron are presented. Mechanisms for pion production are discussed and the 4π yields of pions are used to infer the initial state entropy produced in the collisions. Proton rapidity density distributions, analysed in a hydrodynamical context, provide a measure of the longitudinal expansion of the system after collision. A beam energy excitation function of the average longitudinal flow velocities is extracted and compared to data from other experiments.

Acknowledgments

Of all the words that I have poured into this dissertation, these are the hardest to write. My undying gratitude extends to everyone who has helped me achieve this goal. There are so many people to thank, I apologize for not mentioning every one of you by name.

First and foremost, I want to acknowledge the very most important people in my life, my family: my mom ("who taught her everything she knows...") and dad, my sisters, my brothers-in-law, my nephews, my amazing and beloved husband, Tom, and his family. Thank you for all of your wonderful encouragement and support throughout these years. Without them, I would never have made it this far.

For five years I have had the honor and privilege to be a part of the UC Davis Nuclear Physics Group. From the very beginning I have been surrounded by enthusiastic, interesting and helpful people, all dedicated to the same goal: to understand just a little bit better the complicated workings of our Universe in the laboratory of relativistic heavy ion collisions. I am very grateful to my advisor, Daniel Cebra, who challenged me to work hard and rewarded my efforts with lots of encouragement and visibility among the greater scientific community. I have gained a friend and mentor for life. Thanks, Daniel.

I am also grateful for the kindness and dedication of Jim Draper. The hours he spent with me one-on-one going through Wong's book on Heavy Ion Physics before my

oral exam was probably the best physics course I have ever taken. This dissertation is a far better document than it would have been without his careful reading and suggestions and our many stimulating discussions. Thank you also to Juan Romero and Paul Brady. Paul encouraged me to explore the topics on entropy production and baryon stopping which have become such an important part of this research.

As the last in the current line of NPG graduate students, I have many fellow students (who have since moved on) to thank: Mike Anderson, Bill Caskey, Hollie Cooper, Ian Johnson, Jen Kurzweg, Ayoub Tartir, Lynn Wood. I learned something from everyone and I am glad that we had the chance to work together. Very special acknowledgment is owed to Mike Heffner. From discussions of physics to computers to our outside interests, he was always a great source of information and stimulating conversation. Our work on parallel topics made our interactions so fruitful, I don't know how I managed this last year without him.

Additional thanks are due the members of the E895 Collaboration for giving me the chance to join an exciting experiment. I learned a lot from this group of outstanding scientists.

Contents

List of Figures

ix

List of Tables

Chapter 1

Introduction

1.1   Overview

This dissertation presents a summary of extensive analyses of charged pion production and proton longitudinal flow in 2 to 8 GeV per nucleon (AGeV) central Au+Au collisions. The goal of this work is to characterize the final-state redistribution of the initial available energy by studying the pion and proton transverse mass spectra over all of rapidity space. A "thermal" analysis of the pion m_t-m_0 spectra, with additional effects included to account for long-range electromagnetic interactions and resonance decay influences will be presented. From the proton m_t-m_0 spectra, an excitation function of the longitudinal collective motion of the collision system is extracted.

The dissertation is organized as follows: Chapter 1 presents an overview of the field of Relativistic Heavy Ion Physics and motivates the analysis performed; Chapter 2 discusses the experimental setup and details of the detector operation; Chapter 3 reviews the first pass data analysis performed on the raw data; Chapter 4 covers the fundamentals of particle identification in a time projection chamber and some of the specific details considered in this experiment; Chapter 5 builds on the foundations of Chapter 4, discussing the kinematic variables of interest and the methods of extracting the raw pion and proton yields as a function of these variables; Chapter 6 introduces detector efficiency and acceptance and the methods for correcting the raw yields; Chapter 7 presents the fully corrected final results of pion and proton production over all momenta at each of the four incident beam energies; finally in Chapter 8,

discussion of the models used to interpret the results and comparisons to data from other experiments are presented.

1.2 Relativistic Heavy Ion Physics

The field of relativistic heavy ion physics is concerned with the study and characterization of nuclear matter under extreme conditions. This hybrid field utilizes the instruments and techniques of high-energy particle physics to build on our understanding of the fundamental properties of the nucleus. The extremely hot and/or dense material produced in heavy ion collisions provides an earth-bound laboratory for studying the interiors of neutron stars, the dynamics of supernova explosions and primordial hadrosynthesis, as well as probing some details of the non-Abelian gauge theory of the strong interaction, Quantum Chromodynamics (QCD).

Figure 1.1 represents the Phase Diagram for nuclear matter, with temperature plotted versus baryon density. Just as with water, distinct phases of nuclear matter can be identified. Measuring the critical parameters governing the transitions among these phases is crucial to building a theory of the nuclear equation of state. Normal nuclear matter, at a density of approximately $\rho_0 = 0.13$ fm^{-3} and temperature near zero lies at the bottom left on the figure ($\rho/\rho_0 = 1$), near the liquid-gas transition boundary. This low-temperature, low-density ($0 < \rho/\rho_0 < 1$) region, the domain of low-energy nuclear physics research, was extensively characterized during the twenti-
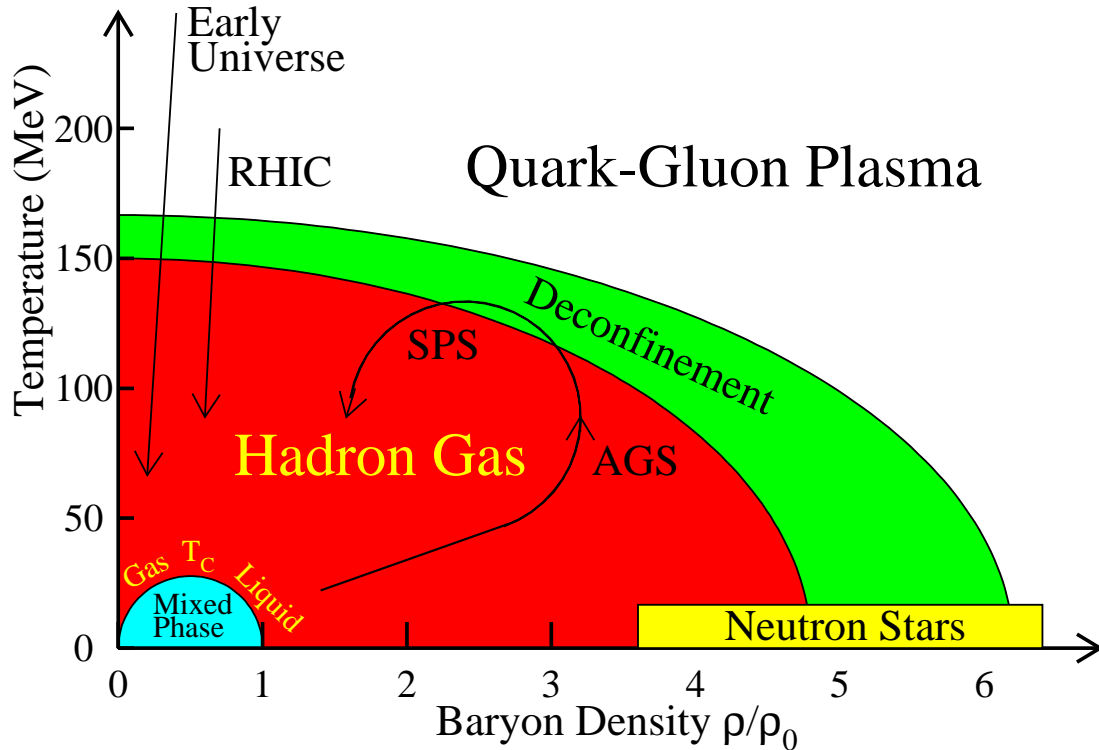
Figure 1.1: Nuclear matter phase diagram.

eth century.

The two extremes of the deconfinement transition curve plotted on the phase diagram have been established by studies using models of the strong interaction under the most extreme conditions. Lattice QCD calculations with two quark flavors at zero baryon density have fixed the deconfinement temperature at zero baryon density to 150 MeV.[Blum95] Estimates of the zero-temperature baryon density roughly 5 times

that of normal nuclear matter required for deconfinement to occur are estimated from the bag model of quark confinement.[Wong94] In this model, the quark constituents of hadrons are essentially confined inside a bag whose outward pressure is generated by the random motion of the quarks in the bag. When the inward pressure becomes higher than the outward pressure, as is the case when hadrons are squeezed tightly together (as in a neutron star), the bag "melts" and the quarks become deconfined.

It is quite interesting to note that the temperatures achieved in heavy ion collisions are the highest temperatures ever created by humans in the laboratory. In collisions studied at the Brookhaven National Laboratory Alternating Gradient Synchrotron, a typical final-state temperature is on the order of 100 MeV. This is after the system has expanded and cooled from an earlier, hotter state. For comparison, room temperature T=300 K is approximately 1/40 eV. In degrees Kelvin, 100 MeV is on the order of a trillion degrees! ($\sim 10^{12}$ K) The next nearest man-made conditions that come close are those generated in thermonuclear explosions, on the order of 10 million degrees ($\sim 10^7$ K). The size (~ 1000 fm^3) of the matter[Lisa00] created at this temperature is extremely small, but the number of individual particles can be on the order of a few hundred to a few thousand, which makes a statistical approach to defining an Equation of State (EOS) quite natural.
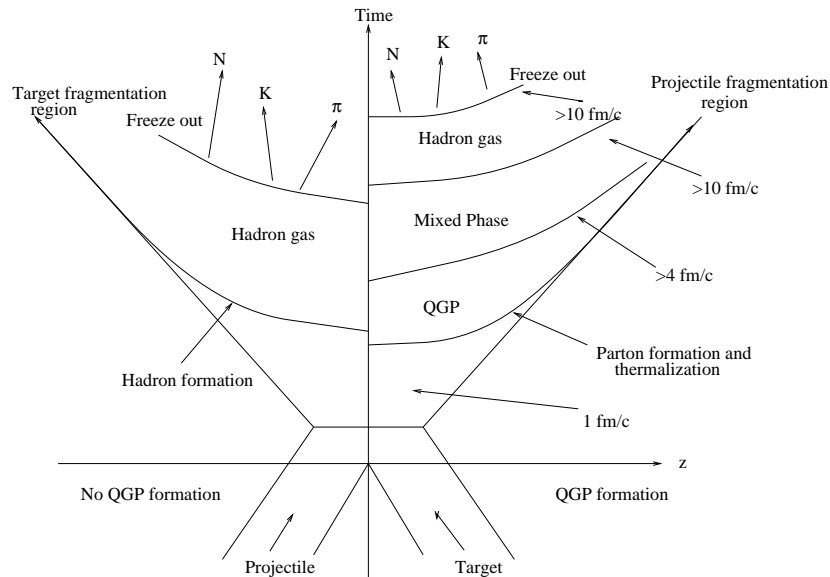
Figure 1.2: Bjorken space-time evolution of heavy ion collision for two scenarios: QGP formation on the right, no QGP formation on the left.[Dunn97]

1.3 Space-Time Evolution of a Collision

A simple model of the space-time evolution of a heavy ion collision is presented in Figure 1.2. The collision axis along the direction of the beam (generally defined as the "z" direction) is represented on the horizontal axis of the plot, with increasing time following the instant of collision indicated along the vertical axis. In this scenario, the incoming nuclei, traveling at nearly the speed of light, collide at the origin. The left-hand side of the diagram indicates the evolution of the system if no Quark-Gluon-Plasma is formed. A hyperbola in this space represents a constant proper time. Hadrons emerge at proper time of approximately 1 fm/c with a temperature, T. The interacting gas of hadrons expands and cools to the freeze-out point, where

interactions cease. At this point, the particles free-stream toward the detector. The thermal energy, as measured by particle momentum spectra in heavy ion collisions, is indicative of the temperature of the system at the freeze-out point.

In the extremely relativistic case proposed by Bjorken[Bjor83], the wounded nucleons from the incident nuclei recede from the collision zone at nearly the speed of light, leaving a baryon-free, high energy density vacuum in the central region. This phenomenon has been dubbed transparency, for it appears that the colliding nuclei or nucleons are able to "pass through" one another losing only some fraction of their initial longitudinal momenta. Within the central vacuum region, a plasma (on the order of the transverse size of the colliding nuclei) of free quarks and gluons (QGP) forms. This is shown schematically on the right hand side of Figure 1.2.

Normally, quarks and gluons are confined inside hadrons of two types - mesons (one quark and one anti-quark plus gluons) and baryons (three quarks plus gluons). The strong nuclear force which binds them together is strongest at large separation distances and decreases at very small distances. Attempting to pull a quark free from its bound state inside a hadron results in the creation of a new hadron rather than a free quark. Only when nuclear matter is highly excited and/or extremely compressed, such as in high energy heavy ion collisions, can the quarks and gluons roam freely in the nuclear medium, unbound inside the hadrons from which they originated. As this medium (on the order of the nuclear size) cools and expands, the free quarks and

gluons "hadronize" into a gas of interacting hadrons which then evolves similarly to the case when no QGP is formed. However, the initial state of some aspects of this evolution will be altered by the presence of a quark-gluon plasma.

How then to distinguish these two scenarios?: by systematically studying all observable phenomena emerging from heavy ion collisions over a broad range of beam energies, system sizes and relative impact parameters. In the absence of a smoking gun, only a consensus of experimental measurements of various observables can provide evidence for the creation of a deconfined phase. This includes establishing the baseline behaviour of nuclear matter under conditions in which a QGP is not formed.

1.4   Brief History of the Field

Many earth-bound laboratories, covering a wide range of collision characteristics, are devoted to the study of hot, dense nuclear matter. The lower energy regime consists of the Bevalac at Lawrence Berkeley National Laboratory and SIS (Heavy Ion Synchrotron) at GSI in Darmstadt Germany, among others. These facilities are capable of accelerating gold (Au) ions up to 1.0 GeV per nucleon (AGeV). In the intermediate high-energy range, the Alternating Gradient Synchrotron (AGS) at Brookhaven National Laboratory collides Au beams on Au targets in the range 2.0 AGeV to 11.6 AGeV, while the top energy heavy beams (Pb) of the CERN SPS (Super Proton Synchrotron) reach 160 AGeV. All of these facilities collide ion beams with

fixed targets, in contrast to the extremely high energy, newly completed Relativistic Heavy Ion Collider (RHIC) at Brookhaven. RHIC achieves center of mass energies for Au collisions of 200 AGeV by colliding two counter-circulating Au beams at 100 AGeV each. The range of collision energies from the Bevalac to RHIC represents a span of over four orders of magnitude in the center of mass! In addition, all of these facilities can study system size dependence by varying the ions from the lightest possible (Hydrogen) to the extremely heavy (Gold, Lead, Uranium). Beyond the currently existing facilities, the Large Hadron Collider (LHC) at CERN, which will collide ion beams at 3 ATeV, is scheduled to begin data taking in 2007-2008. With such a diverse collection of experimental conditions available, we have the capacity to obtain a broad understanding of how these collisions mirror the conditions of the real-world processes they attempt to re-create.

1.5 Motivations

Much can be learned by observing the dynamics of the matter formed in relativistic heavy ion collisions. Some of the questions we must answer are: What are the initial conditions immediately after a collision? How does the system (microscopically and macroscopically) evolve from these initial conditions? What do the analyses of the particles observed by our detectors tell us about the collision dynamics? Is there a solid indication that thermal equilibration of the produced matter is achieved?

In order to address some of these questions, consider a collision between two ^{197}Au nuclei. The number of constituent nucleons in this collision make it an ensemble system that we can model thermodynamically. The energy deposited in the collision region is shared among various modes: particle production, thermal motion and collective motion.

In general, pions constitute the dominant fraction of the produced particles. A systematic study of the multiplicities and momentum distributions of pions can help to characterize particle production under the extreme conditions achieved in these collisions. As early as the 1950's, Fermi[Ferm50] and Landau[Land53] suggested that the number of pions created in a collision might be used to infer the entropy produced in the early stages of the reaction. Assuming adiabatic expansion, one might then be able to determine the early stage entropy from the final state particles. Gaździcki more recently proposed using this model to establish the deconfinement phase transition to a QGP in a heavy ion collision.[Gaźd95b] In a QGP, the color degrees of freedom of the quarks and gluons increase the entropy of the system, compared to the entropy for a hadron gas. Discontinuities in the pion multiplicities as a function of beam energy might indicate a phase transition. Studies of pion multiplicities over a wide range of energies, including those presented in this dissertation, help establish the baseline from which such a scenario might be deduced.

Fluid dynamics can successfully predict the emission patterns of particles emerg-

ing from heavy ion collisions.[Stöc86] Evidence for hydrodynamical flow has been reported by many experiments which are capable of measuring the momenta of a significant fraction of the emerging particles.[Herr96],[Schn93],[Brau95],[Barr94] The type of collective motion depends on a number of factors, including the size and shape of the colliding nuclei, the impact parameter of the collision, the incident energy of the beam particles and the evolutionary stage of the collision.

Collective motion along the longitudinal direction is one of the topics explored in this dissertation. Elongated rapidity [1] density distributions of the observed final state particles emerging from central heavy ion collisions cannot be explained by isotropic emission from a stationary thermal source. [Herr96], [Schn93], [Brau95], [Appe99]

A feature particular to the proton rapidity densities measured at the CERN SPS[Appe99] is a double-humped structure. In contrast, the pion rapidity densities are peaked at the center of mass rapidity. [Schn93] At these beam energies, the protons appear to retain a significant fraction of their initial longitudinal momenta. This may be an indication of partial nuclear transparency, where the incoming nuclei are slowed down significantly but are not completely stopped at the center of the reaction zone.[Busz84], [Vide95], [Back01] In addition, the system may develop a significant hydrodynamical expansion due to the buildup of pressure from a highly excited,

---

[1]Rapidity is defined as $y \equiv \frac{1}{2}ln\frac{(E+p_z)}{(E-p_z)} = \frac{1}{2}ln\frac{(1+\beta_z)}{(1-\beta_z)}$ where E is the particle's energy, p_z is the longitudinal component of the particle's momentum and $\beta_z(\equiv \beta_L)$ is the longitudinal velocity of the particle in units of c. In the nonrelativistic limit rapidity is equivalent to β_L. Rapidity is widely used in relativistic dynamics because it has the appealing property of being an additive quantity under a Lorentz boost.

stopped nuclear matter fireball.[Schn93],[Stac96],[Siem79] This latter explanation is supported by observations at the AGS and SPS that other particles, including pions and Λ hyperons, also exhibit collective behaviour along the beam axis.[Schn93], [Wess97] Regardless of its origin, the elongation of the rapidity densities can be used to infer an average longitudinal velocity of the system. For this dissertation, an energy excitation function of the average longitudinal velocity will be extracted from the proton rapidity densities at 2, 4, 6, and 8 AGeV.

Chapter 2

Instrumentation

2.1   E895 Experimental Setup

The E895 Experiment was performed at the Brookhaven National Laboratory Alternating Gradient Synchrotron (AGS). The 250 m diameter accelerator is capable of accelerating gold ions up to a maximum of 10.8 AGeV. E895 collected data from a series of runs with gold, silver, copper, and beryllium targets at four different beam energies. For this dissertation, data collected from ^{197}Au beams at kinetic energies of 1.85 AGeV, 3.91 AGeV, 6 AGeV and 8 AGeV colliding with a ^{197}Au target were analysed. For simplicity, throughout this dissertation, the low energy beams will be referred to by the nominal values 2 AGeV and 4 AGeV.

The E895 detector configuration (Figure 2.1) consisted of a set of triggering scintillators, a large volume Time Projection Chamber (TPC), situated inside the Multi-Particle Spectrometer (MPS) magnet[MPS95], and a MUltiple Sampling Ionization Chamber (MUSIC)[Chri87],[Baue97]. The TPC, also known as the EOS (Equation of State) TPC, which was built at Lawrence Berkeley National Laboratory in 1990[Rai90] for the EOS Experiments at the Bevalac,[Pugh86] was the major component of the E895 detector system. For the E895 experiment, the magnetic field was set at 0.75 or 1.0 Tesla in order to optimize the rapidity acceptance for both pions and protons. In addition, the gas gain of the TPC was set as high as possible to maximize performance for minimum ionizing particles.
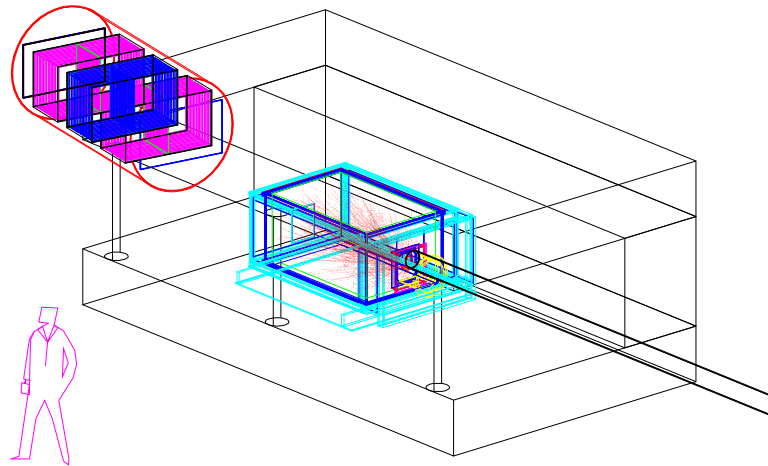
Figure 2.1: GEANT drawing of E895 Detector setup inside the MPS Magnet on the A1 line of the AGS. MUSIC is shown on the upper left. The beam enters the experimental area from the lower right.

2.2   Triggering

Time projection chambers are 'slow' detectors, compared to other common charged particle detectors. This is because the electrons left in the trail of ionization along the particle's trajectory must first drift through the gas to the amplification region. In addition, due to the sheer quantity of data, the digitization and readout time are considerable. In order to avoid space-charge build-up, the amplification region is normally kept closed with a gating grid. Therefore, it was necessary to employ a set of triggering detectors to determine precisely when an event occurred and to allow pre-selection of events. Figure 2.2 shows a schematic drawing of the E895 triggering hardware.

A series of beam detecting scintillators approximately three meters upstream of
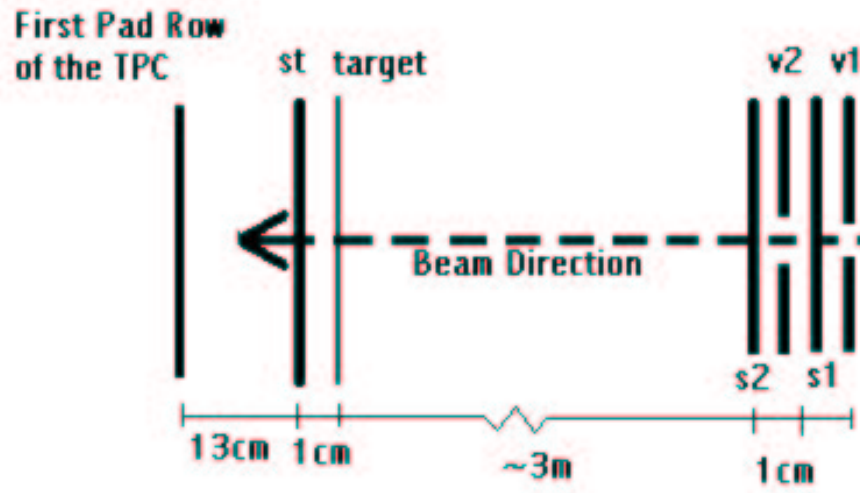
Figure 2.2: E895 Triggering Scintillators. Beam signals in S1, S2 and no signal in V1 and V2, combined with an event signal in ST alert the TPC to collect the event.

the target identifies every good incident particle. Spurious cosmic ray background is excluded by requiring a coincidence between S1 and S2. Off axis incident beam particles are rejected using V1 and V2. Fragmentation of the incident beam particle is rejected by requiring a valid beam amplitude signal in both S1 and S2.

Scintillators produce photons from the energy loss of charged particles passing through them. The signal is proportional to the sum of the squares of the charges of the particles. A signal with amplitude proportional to $Z^2 = 79^2$ (Z=79 for ^{197}Au) in S1 and in S2, combined with no signal in the "veto" scintillators, V1 and V2, ensures that a gold ion is delivered intact to the target. (V1 and V2 have ~ 1 cm diameter holes in their centers. If the beam passes through the hole, no signal is produced.)

If a beam-target interaction occurs, the ST scintillator signal reflects the fragmen-

tation due to the interaction. The magnitude of the signal from a large collection of small-Z fragments ($\propto \sum_i Z_i^2$) is smaller than the signal from a smaller collection of high-Z fragments. The ST scintillator provides a gross measurement of the impact parameter of the collision, since more fragmentation is expected from a head-on collision compared to a grazing collision. In this way, the triggering hardware can be used as an online centrality selector. Raising or lowering the signal threshold on ST distinguishes "minimum bias" from "central" triggers. The combined scintillator outputs are fed to a logic circuit which determines whether the event should be read out by the TPC and written to tape.

2.3   Time Projection Chamber Operation

Charged particles are detected in a TPC by the ionization produced from their interactions with gas molecules in the active volume of the detector. The average number of electrons produced in an ionization event is proportional to the energy loss of the ionizing particle. The ionization is forced to drift toward a multi-wire proportional chamber (MWPC) by a controlled uniform electric field. The ionization is proportionately amplified in the MWPC. The positive ions produced by this amplification linger in the region after the electrons have been absorbed by the anode wire, and induce a signal on a segmented pad plane beneath the MWPC. The front end electronics provide further amplification, time sampling, and digitization of

the information, which is then sent through fiber-optic lines to the data acquisition system (DAQ), located in the counting house, for storage.

Particle tracks are reconstructed from the projection of their ionization on the 2-d (x-z) pad plane and the drift distance in the y direction, calculable from the measured drift time and the known drift velocity. The curvature of the charged particle trajectories in the magnetic field (0.75 Tesla at 2 AGeV and 1.0 Tesla at the other beam energies) inside the detector is used to calculate the particle momenta. More details regarding the detection of charged particles with drift chambers are available in References [Blum94],[Fern86],[Leo94].

2.3.1 Drift Volume

The drift region of the EOS TPC measures 150 cm $\times$ 96 cm $\times$ 75 cm, and is terminated at the bottom of the chamber by the MWPC and pad plane. A mixture of 90% Argon (Ar) and 10% Methane (CH_4), called P10, at ambient temperature and pressure flowed continuously through the TPC. Argon is desirable for its low working voltage in the amplification region and its high gain. The methane acts as a quenching gas by absorbing photons emitted from excited argon, which might otherwise produce spurious signals.[Leo94]

The 125 V/cm electric field (chosen for the stability of the drift velocity against minor field variations) that caused the ionization electrons to drift to the MWPC

region was created by biasing the top cathode plate at -10 kV while grounding a wire plane immediately above the amplification region. An electric field cage surrounding the outer edge of the drift volume defined the potential along the boundaries of the drift volume, insuring the uniformity of the electric field. The drift velocity of ionization in P10 at S.T.P. for this field strength is nominally 5.5 cm/μs. (See Section 2.4) The maximum drift time for a cloud produced near the top of the drift volume is approximately 20 μs. Accurate measurement of the drift time and the drift velocity are required to reconstruct the y-components of particle trajectories. A useful side-effect of the magnetic field (oriented in the same direction as the electric field) is the reduction of transverse diffusion of the electron clouds as they drift parallel to the field lines toward the amplification region. A not-so-useful side-effect of the magnetic field is distortion in the projected track positions due to edge effects; the magnetic field lines are not perfectly parallel everywhere in the detector. These distortions are corrected offline during the first stage data processing.

2.3.2 Multi-Wire Proportional Chamber and Read-out

After the ionization clouds from a charged particle track drift to the bottom of the TPC, they reach the MWPC (Figure 2.3). The entrance to the MWPC is guarded by a Gating Grid (Figure 2.4). In the closed configuration, the potential on adjacent wires alternates, terminating the electric field lines on the grid wires. The electrons

TPC PAD PLANE

Ionizing Track

Drifting Electrons

Gating Grid

Ground Grid

12 X 8 mm Pads

Field/Anode Grid
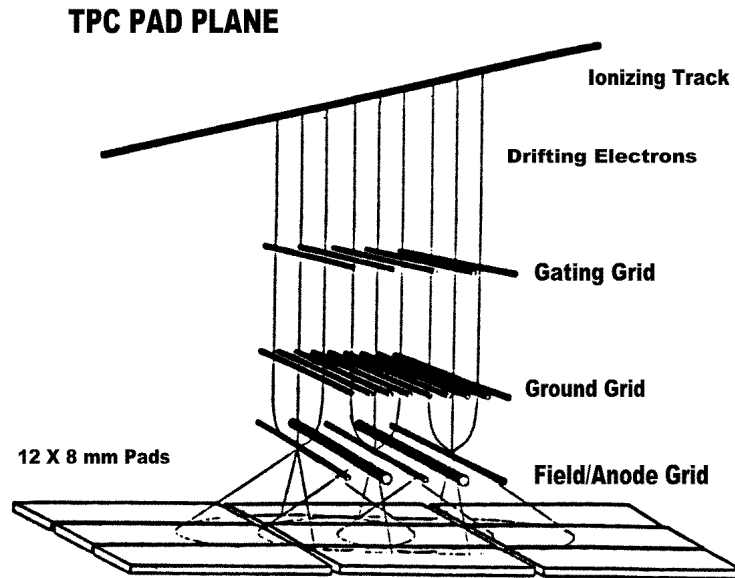
Figure 2.3: Diagram of the Multi-Wire Proportional Chamber with pad-plane read-out. [Rai90]

follow the field lines to the wires and travel through the wires out of the TPC to the power supply. The gating grid remains in the closed position until the trigger signals that an event is on its way and that the DAQ is prepared to read it out.

In the open configuration, the gating grid wires are held at the drift potential that would be present if the grid were absent, allowing the ionization to continue drifting toward the amplification region. Separating the drift volume from the amplification region is the ground plane. The ground plane terminates the drift field and serves to prevent ions produced during ionization amplification from traveling into the drift volume. Excess positive charge build-up in the drift volume would distort the electric
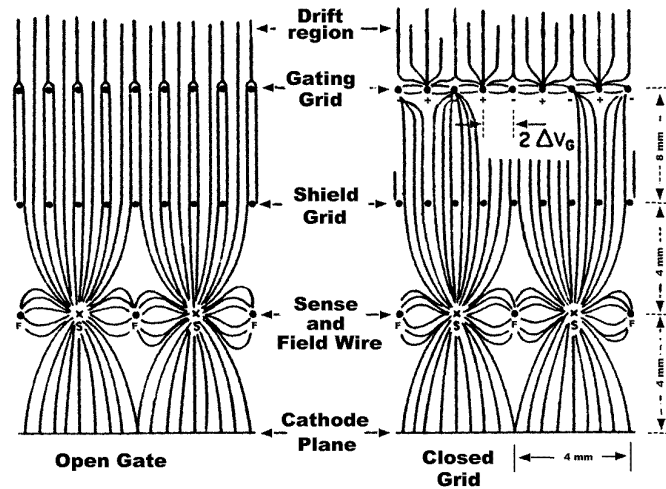
Figure 2.4: Field lines for the two configurations of the gating grid: open and closed.[Lohse]

field, causing spatially dependent variations in the drift velocity.

The amplification plane is composed of alternating sense and field wires. The field wires are thicker than the sense wires, and serve to shape the electric field and reduce electronic crosstalk between the high voltage sense wires. The 20 μm diameter sense wires are held at 1.2 kV, producing a 1/r electric field which accelerates the ionization electrons as they approach the wires. The acceleration causes an avalanche of ionization around the wires which is proportional to the number of incoming electrons (Gain $\sim$ 3000). The avalanche electrons are carried away to ground by the sense wires, leaving heavy positive ions in the region. These ions drift very slowly with the field lines toward the ground plane. Before they are neutralized, they induce an

image charge on the pad plane which is collected by read-out electronics, digitized and stored on magnetic tape. Details of the readout electronics and DAQ used in this experiment can be found in References [Cask99],[Rai90].

2.4 Calibrations

The detector must be calibrated to prevent arbitrary distortions in the tracks reconstructed for each event. Variations in the drift velocity as well as distortions of the primary ionization clouds due to run-to-run pressure and temperature variations, gas impurities, and field distortions must all be measured and corrected.

Reference tracks whose trajectories are not curved by the magnetic field were introduced using a Nd:YAG laser. Since the beams ionize the gas in straight lines, comparison of the detected trajectory with the expected trajectory can be used to correct for spatial distortions in the TPC. Laser runs were performed intermittently with real data taking to provide real-time information about changing distortions.

In addition to the laser calibration system, a second, smaller drift chamber called the Canary was used to monitor gas purity and drift velocity. Since the detector ran with a continuous gas flow, impurities such as O_2 and H_2O might be introduced through leaks or supply bottle variations. Ionization electrons which encounter O_2 or H_2O molecules are absorbed, attenuating the final collected signal, or their drift velocity is changed. By diverting some of the exhaust gas of the TPC to the Canary,
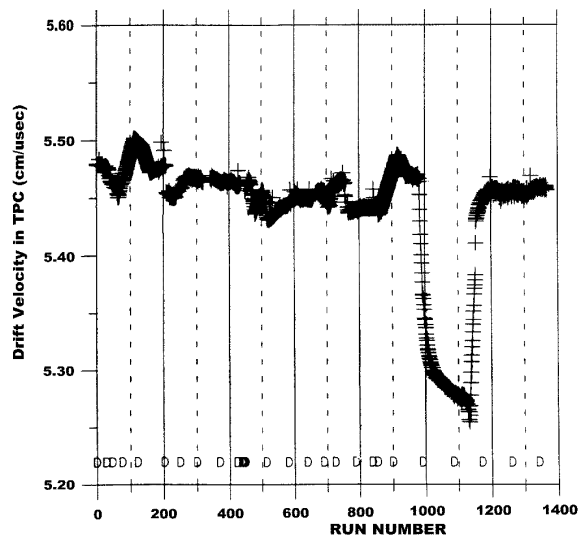
Figure 2.5: Run-to-run drift velocity measurements in the Canary, courtesy J.E. Draper.

this effect could be characterized. The Canary measures drift velocity by comparing the arrival times of a reference laser signal on the wire chamber with the drift time of photo-electric ionization produced at the top of the chamber by the laser. This is also done run-to-run (Figure 2.5) so that real-time conditions may be matched with the data.

Chapter 3

Pass 1 Data Analysis

3.1 Track reconstruction

The raw ADC signals collected by the DAQ cannot be directly analysed to extract physics information from the collisions. Approximately two million individual ADC signals (128 padrows × 120 pads per row × 130 time buckets) are read out in each event. The process of reconstructing particle trajectories (tracks) and the average ionization for each track from this pixel information must first be performed. The steps involved in this process are described in the following sections.

3.1.1 Hit-finding

The first step in track reconstruction is determining the three dimensional origin of the ionization produced along the particle's trajectory through the TPC. The initial clouds of ionization suffer some diffusion as they drift toward the MWPC, spreading the signal across multiple time buckets and pads. The hit-finding software looks for clusters of ionization in the 2-dimensional x-y plane for each of the 128 padrows along the z-direction. Figure 3.1 shows an example of three hits found in two clusters. Deconvolution must be performed if a cluster contains more than one probable hit. At this stage, the tracks are assumed to cross the padrows perpendicularly, so the integrated ADC signal from each hit is stored as the energy deposited (dE) for the hit.

The position resolution of a TPC depends on the ionization clouds being dis-
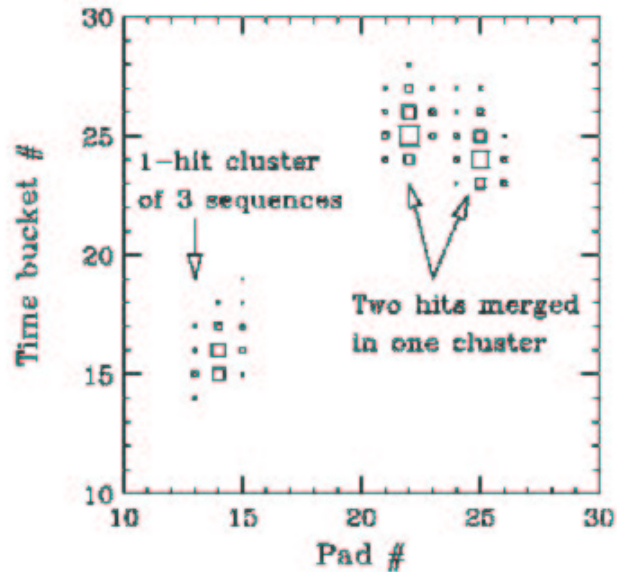
Figure 3.1: An example of 2-d hitfinding for three tracks crossing a given padplane. [Lisa96]

tributed over several pixels in both the x and y directions. (Since the tracks generally lie in the z-direction, the software was written to search for hits only in the x-y plane, therefore the spatial resolution in the z-direction is the pad length - 1.2 cm for the EOS TPC.) Single pad hits (in the x-direction) have the worst position resolution (0.8 cm) since the the most probable crossing point must be taken as the center of the pad. Finer resolution is achieved when a hit is distributed over multiple pads, as the maximum of the ADC signal can be determined more precisely. With a drift velocity of 5.5 cm/μs, a drift length of 75 cm, and 130 time samples, the spatial resolution in the y-direction is generally 0.7-0.8 mm. Multiple sampling improves the determination of the Gaussian centroid. Resolution is worse in the y-direction

because longitudinal diffusion of the ionization clouds is larger than the transverse diffusion. Once the hit-finding is complete, a correction is applied to account for magnetic field distortions which displace hits from their assumed straight-line projections in the drift direction.

3.1.2 Track-finding

The tracking algorithms used in E895 employ the pattern recognition technique of a Kalman Filter (Fitter)[Liko92] to systematically project from padplane to padplane the most probable paths of the charged particles. The tracker starts at the last padplane in the TPC, where the hit density is the lowest, and makes a straight line projection between nearby hits in consecutive padrows. Once approximately five consecutive hits have been found, the straight line projection is replaced by a helix fit to the hits using the magnetic field map. This helix can then be projected back toward the target through the higher hit density padrows, with a reasonable estimate of the location of the next hit. The track is extended in this way until no likely hit candidates are found for eight padrows. A track must have a minimum of seven hits to get a reliable helix fit.

Once hits are assigned to a track they are removed from the sample of candidate hits to prevent multiple assignments. After the tracker has exhausted the hit sample, hit-finding and tracking are re-done, using the information gained in the first pass

about the crossing angles of the found tracks. This information makes it possible to produce a more reliable position and dE measurement for a given hit. A model of the dE which includes the crossing angles and most probable hit position are fit to the ADC signals to produce a dE/dx for each hit. This eliminates threshold problems and improves in the deconvolution of signal from overlapping hits.

The radius of curvature (ρ) of a track is combined with the magnetic field map to determine the magnitude of the rigidity:

$$r = \rho * B. \tag{3.1}$$

The rigidity is directly related to the momentum through the particle's charge:

$$p = r * Z. \tag{3.2}$$

In general, momentum resolution depends on the spatial resolution of the detector, the particle momenta, magnetic field and the number of track fitpoints, N_{hits}. However, at very low momentum, resolution is dominated by multiple Coulomb scattering effects, the second term in the following.[STAR92]

$$\left(\frac{\delta p}{p}\right)^2 = \frac{p^2\sigma^2 720}{e^2 B^2 s^4 (N_{hits} + 6)} + \frac{3x10^{-3}}{B^2 s L_R \beta^2} \tag{3.3}$$

$$
\begin{aligned}
p &= Momentum\ (GeV/c) \\
\sigma &= spatial\ resolution\ (m) \\
e &= 0.2998\ GeV\ Tesla\ m/c \\
B &= Magnetic\ Field\ (Tesla) \\
s &= Track\ length\ (m)
\end{aligned}
$$

$$
\begin{aligned}
N_{hits} &= Number\ of\ track\ samples \\
L_R &= Radiation\ length\ of\ Argon\ at\ STP\ (m) \\
\beta &= Particle\ velocity\ (c)
\end{aligned}
$$

Tracks with fewer N_{hits} have less well-determined momenta than tracks with more hitpoints. Since the resolution depends on the momentum of the particle in question, it is difficult to declare a single number the nominal resolution for the TPC. However, for certain regions of phase space and bounds on N_{hits}, E895 has reported momentum resolution of between 1.5% and 3%.[Lisa00]

3.1.3 ⟨dE/dx⟩ Calculation

⟨dE/dx⟩ for a given track must be determined from the discrete ionization samples collected by the TPC along a track's trajectory through the drift gas. The amount of ionization (dE/dx) in any one sample is stochastic, but the probability of obtaining a specific value of dE in an ionizing encounter can be modeled[Alli80]. The probability distribution is characterized by a peak around the most probable value with a high dE tail. The tail is due to the fact that large energy transfers from single collisions (delta rays) are possible, though improbable, skewing the distribution toward high dE. The asymmetry in this distribution shifts the mean dE value above the peak value. The exact position of the mean depends on the maximum allowable energy transfer, W_{max}. This cut-off is kinematically limited and depends on the mass of the ionizing particle, but there is a W_{max} even if the encounter is with a free electron. In
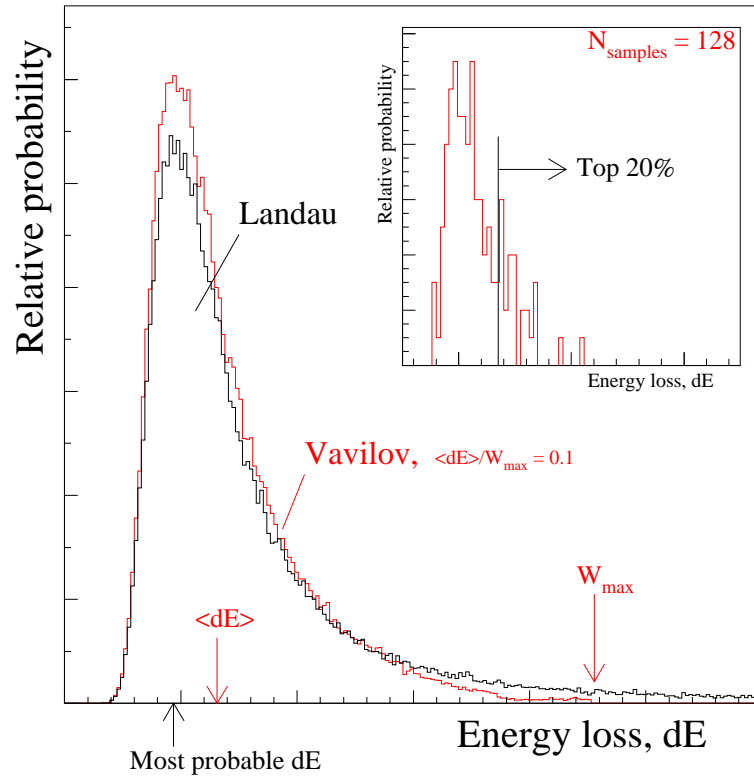
Figure 3.2: Comparison of Landau and Vavilov theories of energy loss in a thin absorber. The inset shows an example of the Vavilov distribution for 128 samples.

the limit as W_{max} approaches infinity, the mean becomes undefined.

Landau calculated the energy loss distribution in this limit (Figure 3.2), making the additional assumptions that the energy transfers are large enough to use a Rutherford scattering approximation (essentially free electrons) and that the incident particle velocity is negligibly affected by the energy loss.[Land44] Vavilov attempted solutions for the energy loss distribution by utilizing the correct expression for the cut-off energy.[Vavi57] If the energy loss distribution is parameterized by the ratio of

mean to maximum energy transfer, $\langle dE \rangle / W_{max}$, in the limit as this ratio approaches zero, Vavilov's theory approaches the Landau limit and in the limit as this ratio approaches infinity, the distribution approaches a Gaussian.[Leo94] The best approximation is probably somewhere between. While the Vavilov approximation can be fit to the dE/dx data to obtain a mean value of the energy loss, the calculation is still sufficiently complicated that a simpler approach is desired.

Typically, $\langle dE/dx \rangle$ is calculated by applying the truncated mean technique. This technique is an attempt to exploit a feature of the central limit theorem, which says that the distribution of the average values (for a large number of samples) of any parent distribution should be a Gaussian. Fewer samples are required to satisfy this theorem if the initial distribution is close to a Gaussian. Therefore, the top N% of energy loss samples is removed before averaging, reducing the effect of the high dE/dx tail and causing the remaining distribution to become more Gaussian (see inset of Figure 3.2). The optimum truncation range lies somewhere between 35% and 70%[Blum94]. As long as the truncated distribution is fairly Gaussian, the simple average of the remaining samples is a reasonable approximation to the mean.

From the Central Limit Theorem, distributions of $\langle dE/dx \rangle$ for ensembles of tracks sampled from the same parent distribution set should be fairly Gaussian-distributed. However, if enough skew still remains after the truncation is performed, the calculated mean will also be skewed away from the true mean. Attempting to combine $\langle dE/dx \rangle$

values for an ensemble of tracks from truncated distributions of different skew results in a non-Gaussian distribution.

In E895, the top 20% of samples for each distribution were removed from the sample used to determine $\langle dE/dx \rangle$. Secondary offline processing uncovered the unfortunate fact that even distributions of $\langle dE/dx \rangle$ for ensembles of tracks within a narrow momentum window and a narrow range of N_{hits} do not form a Gaussian distribution. They exhibit the residual high $\langle dE/dx \rangle$ tail, suggesting that the choice for the truncation parameter was not sufficiently optimized.

Since the second-stage data files do not retain the necessary hit information to allow the track-by-track reprocessing of $\langle dE/dx \rangle$, it would be necessary to repeat first-stage data processing to re-optimize the $\langle dE/dx \rangle$ determination. Considering the large amount of CPU time necessary to reprocess all of the raw data, the decision was made to parameterize the shapes of the existing distributions instead. Details of this parameterization will be described in Chapter 4 and Appendix A.

An empirical relationship to describe the $\langle dE/dx \rangle$ resolution for minimum ionizing particles was developed by Allison and Cobb[Alli80].

$$
\begin{aligned}
\sigma_{dE/dx} &= 0.47 N_{hits}^{-0.46}(Ph)^{-0.32} < dE/dx >_{trunc} \\
P &= Pressure(atm) \\
h &= Samplelength(cm)
\end{aligned}
\tag{3.4}
$$

The more samples, N_{hits}, the better the $\langle dE/dx \rangle$ is determined. Since E895 was a fixed target experiment, the expected number of samples on a given track roughly

depends on the momentum. Tracks with a lot of momentum along the beam direction carve straighter paths through the detector than low momentum tracks bent out of the TPC by the magnetic field. Equation 3.4 predicts a resolution of 7% in the best case. For comparison (see Figures A.1 and A.2), with the quality cuts used in this analysis and the integration over N_{hits}, the best attainable experimental resolution is approximately 8.5%.

3.2 Event Characterization

The last step before physics analysis begins is the classification of events into centrality ranges. Since a head-on (central) collision is expected to be more energetic and produce more particles than a peripheral collision, the total number of detected particles is a good way to separate different event samples. In order to evaluate accurately the number of particle tracks originating from the collision, the event vertex must be reconstructed. Exclusion of particles not originating from the event vertex eliminates contamination from decay products and false tracks produced through interactions in the detector material.

3.2.1 Vertex-finding

The primary event vertex can be reconstructed by projecting track helices back toward a common origin within the target, approximately 13 cm upstream of the
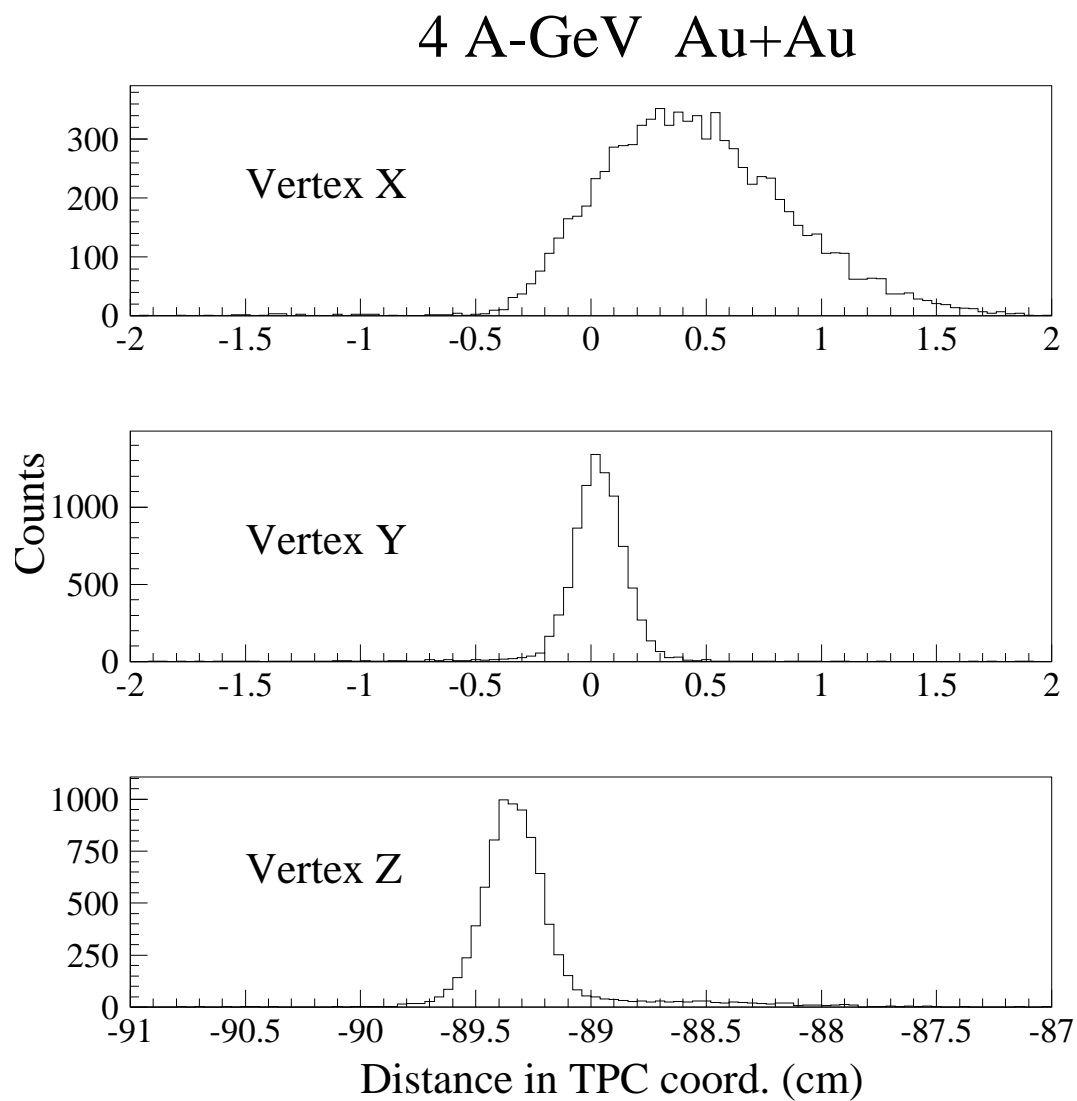
Figure 3.3: 4 AGeV vertex distributions in the x, y, and z directions.
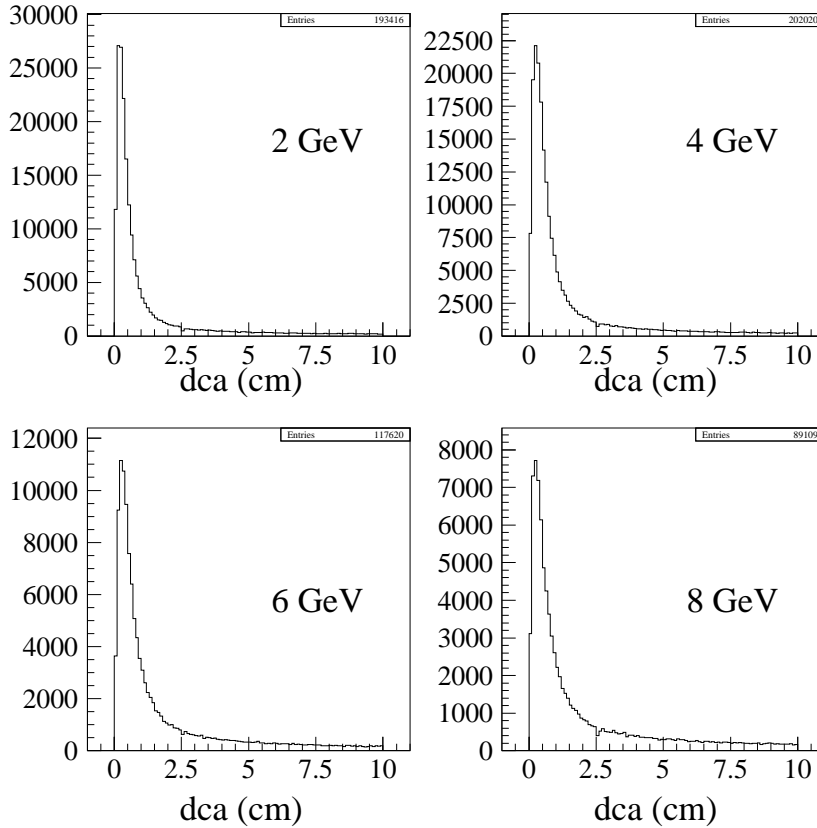
Figure 3.4: DCA distributions at each energy. The quality cut applied for this analysis is DCA < 2.5 cm.

active edge of the TPC. A least-squares fit to the sum of the squares of the distances of closest approach of each track determines the single point identified as the primary event vertex. The vertex resolution in the z-direction, constrained by the target thickness, is approximately 1 mm (Figure 3.3), making it possible to distinguish target-related events from those originating in the ST scintillator, ~ 1 cm downstream of the target.

A quality cut on the 3-dimensional distance of closest approach (DCA) of each track to the found vertex for a given event is the standard method of determining the total primary charged particle multiplicity. Figure 3.4 shows the DCA distributions at each beam energy. The standard cut adopted by the collaboration to define primary tracks is DCA < 2.5 cm. All tracks which fall outside this cut are considered secondary or aberrant and are therefore excluded from the centrality analysis.

3.2.2   Centrality determination

The impact parameter for a heavy ion collision is defined as the vector connecting the transverse projection of the center of the projectile nucleus with the transverse projection of the center of the target nucleus. In a central Au+Au collision, the two nuclei overlap completely; the magnitude of the impact parameter vector is zero. In a peripheral or near miss collision, the magnitude of the impact parameter is roughly twice the nuclear radius, approximately 15 fm (15×10^{-13} cm). The impact parameter cannot be directly measured, nor can it be controlled experimentally. Instead it must be inferred from an assumption of a monotonic relationship between charged particle multiplicity and the geometric collision cross-section.

Since the experiment used an interaction trigger to improve data-taking efficiency, the detector did not record every event nor every beam particle. There is an inherent trigger bias in the data sample which must be accounted for before determining

% Cross-section	Impact Parameter	2 AGeV	4 AGeV	6 AGeV	8 AGeV
1.8%	2fm	190	260	285	320
4.2%	3fm	175	235	260	290
7.4%	4fm	160	210	230	260
12%	5fm	140	180	200	225
17%	6fm	125	155	170	190
23%	7fm	105	120	135	145
30%	8fm	85	90	95	105
38%	9fm	60	60	60	60

Table 3.1: Charged particle multiplicity ranges for different impact parameters at each beam energy. The percent cross-section is compared to the total cross-section measured at 10.8 AGeV[Cebr99] of 6.78 barns.

absolute centrality. The inclusive trigger cross-section can be calculated from the total measured beam rate, the total interaction triggers stored with the raw data, and details of the target thickness. Table 3.1 shows the multiplicity ranges from the minimum bias trigger and the percentage cross-section. This percentage is calculated using the total cross-section for Au+Au measured by the E866 Collaboration at 10.8 AGeV [Cebr99] of 6.78 barns[1] and the corresponding impact parameters for each beam energy. The systematic uncertainties in the multiplicities are $\pm$ 4 counts, so the numbers are rounded to the nearest 5 counts. This corresponds to an error in the impact parameter of approximately 0.5 fm.

The target-related cross-section is obtained by excluding events rejected by a selection on the event vertex. Figure 3.5 shows the target-related minimum bias multiplicity distributions for each beam energy and the corresponding impact parameter

---

[1]For comparison, the geometric cross-section for two gold nuclei of radius r=7.1 fm would be 6.33 barns.
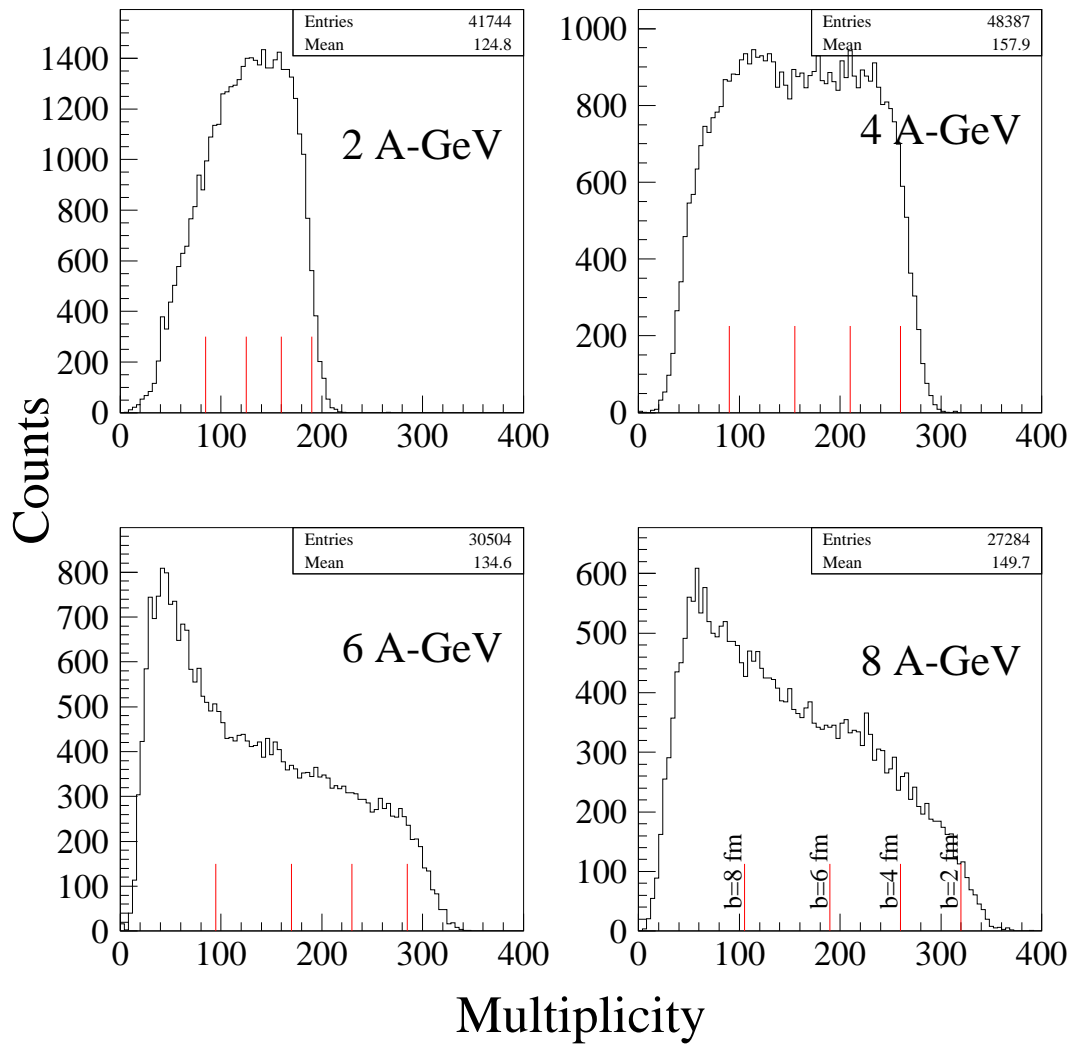
Figure 3.5: Impact parameter ranges associated with the charged particle multiplicities for each beam energy.[Cask99]

E$_{beam}$	Multiplicity Range	N$_{events}$
2 AGeV	> 170	19054
4 AGeV	> 225	21502
6 AGeV	> 250	28385
8 AGeV	> 280	17918

Table 3.2: Number of events analysed for the top 5% most central collisions with multiplicity cuts, corresponding to an impact parameter range of 0 < b < 3.3 fm.

ranges determined from the inclusive trigger cross-section. DCA < 2.5 cm was the only quality criterion applied to obtain the adduced multiplicities. Appendix E of Reference [Cask99] provides a detailed description of both the trigger cross-section determination and the impact parameter calculation.

The data analysed for all physics analyses presented in the following chapters correspond to the top 5% most central collisions. The associated impact parameter range is approximately 0 < b < 3.3 fm. The multiplicity cuts for each beam energy, along with the total event sample analysed are presented in Table 3.2.

Chapter 4

Particle Identification

4.1   Bethe-Bloch Theory

Relativistic charged particles traveling through a medium suffer energy losses primarily due to ionization. The number of ionizing encounters that occur in a given traversed distance is stochastically distributed but characterized by the mean free path of the particle in the medium. The average amount of ionization produced by a particle with a given $\beta\gamma$ in a single ionization encounter can be reasonably well described by the Bethe-Bloch equation,[Barn96]

$$-\left\langle \frac{dE}{dx} \right\rangle = 4\pi N_A r_e^2 m_e c^2 z^2 \frac{Z}{A} \frac{1}{\beta^2} \left(\frac{1}{2} ln \left(\frac{2m_e c^2 \beta^2 \gamma^2 W_{max}}{I^2} \right) - \beta^2 - \frac{\delta}{2} \right) \qquad (4.1)$$

where

$$W_{max} = \frac{2m_e c^2 \beta^2 \gamma^2}{1 + 2\gamma m_e/M + (m_e/M)^2} \approx 2m_e c^2 \beta^2 \gamma^2 \qquad (4.2)$$

is the maximum energy transferred to an electron in an ionizing collision. The approximation holds for heavy (compared to the electron) incident particles at moderate energies $2\gamma m_e/M \ll 1$.

The function drops as $1/\beta^2$ for particles with $\beta\gamma \leq 3$, reaches a minimum (called minimum ionizing) near $\beta\gamma = 3$ and rises again as $\ln(\gamma)$ beyond that. For P10 gas (90% Ar + 10% CH_4) at S.T.P., the density effect correction δ must be included to accurately predict the energy loss of particles with $\beta\gamma \geq 100$.[Ster71] Since the majority of fast particles (high-rigidity pions) detected in E895 did not exceed $\beta\gamma \approx 17$, no density effect correction was required.

4.2 Bethe-Bloch Parameterization

The Bethe-Bloch equation is useful once $\langle dE/dx \rangle$ has been determined, as one can combine reconstructed track rigidity and $\langle dE/dx \rangle$ information to identify particles through their mass using the relationship p = m$\beta\gamma$. Figure 4.1 shows the $\langle dE/dx \rangle$ versus rigidity (= p_{lab}/Z) at 6 AGeV. Each band corresponds to a different mass particle. Negatively charged particles are shown on the left, while the positively charged particles appear on the right. The broad width of the bands in the $\langle dE/dx \rangle$ direction is the result of loose track quality cuts. The plot is shown for all primary tracks (DCA < 2.5 cm), integrated over N_{hits}.

Since many thousands of events are analysed together to minimize statistical errors, a relative gain calibration must be applied to the data to normalize $\langle dE/dx \rangle$ to a common reference value. The electronic gain for a given run reached a stable value after the first few recorded events but varied from experimental run to run. The calibration was performed by projecting a histogram of $\langle dE/dx \rangle$ for negatively charged particles in a rigidity window around the pion minimum ionizing rigidity ($\sim$ 0.4 GeV/c) for a set of events in the stable gain region of each run. The mean values extracted from this window are all compared to the reference mean of 0.2236629E-04 from run 1109 at 4 AGeV. A table of normalization parameters prepared from this study is used in offline analyses to calibrate all events to the reference value.

Since the detector measures relative energy loss rather than absolute energy loss,

E895 Particle Identification
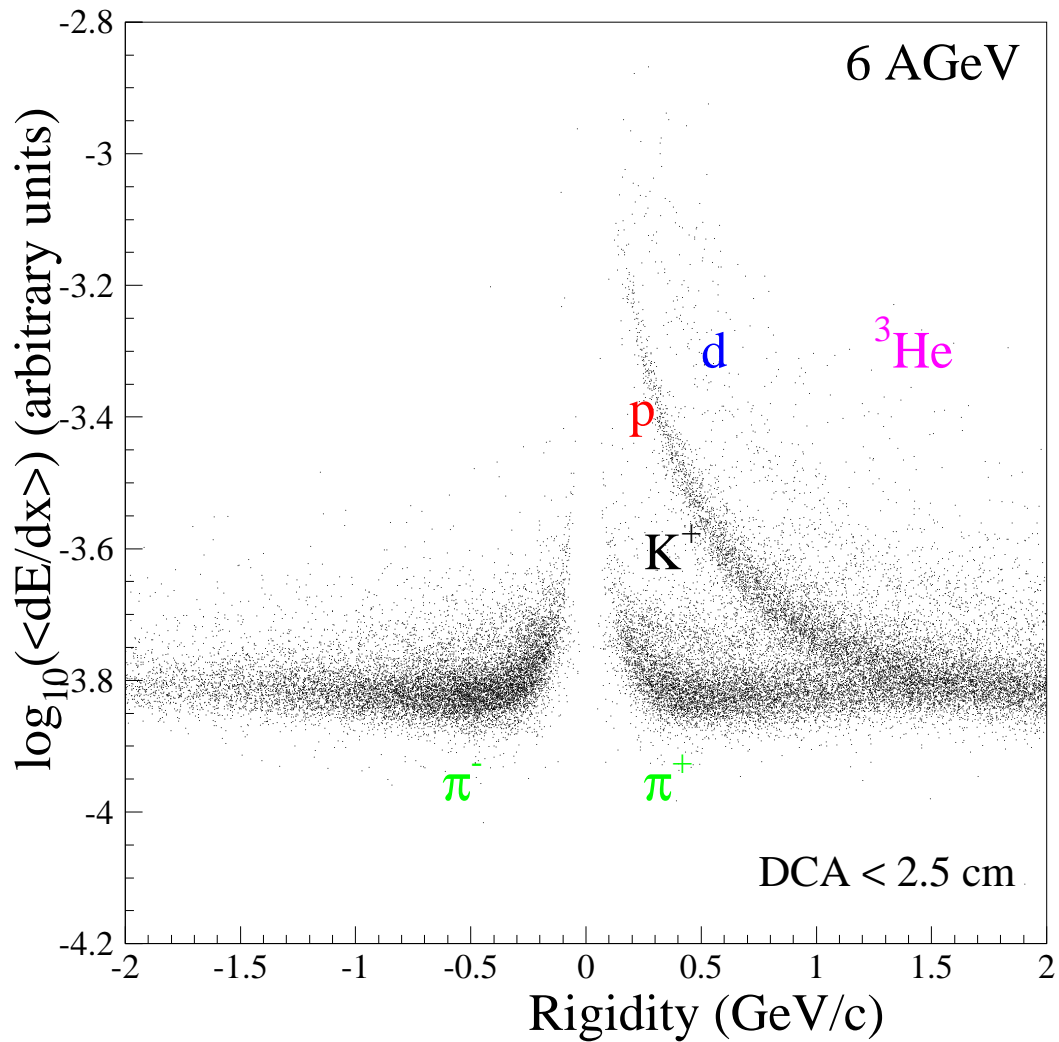
Figure 4.1: Relative energy loss as a function of rigidity (= p_{lab}/Z) at 6 AGeV measured by the TPC. The separation of the energy loss into bands is a function of the particle mass.

the $\langle dE/dx \rangle$ from the data is not directly predictable from the Bethe-Bloch theory. Instead, the theoretical curve is re-expressed as a function of two extractable parameters, ζ and κ, that are fit to the measured data. This method is preferred over a renormalization to the predicted curve to account for possible detector biases which are not included in the theoretical prediction. In fact, the EOS experiment found that an additional correction for electronic saturation due to restrictions on the gain for high-$\langle dE/dx \rangle$ particles was necessary to accurately reproduce the energy loss measured in the data. An empirical relation developed by Scott[Scot95] includes two additional parameters, A and B, to describe the behaviour of this saturation effect.

$$-\left\langle \frac{dE}{dx} \right\rangle = \frac{\zeta}{\beta^2}(\kappa + ln(\beta^2\gamma^2) - 2\beta^2) \qquad (4.3)$$

$$\left\langle \frac{dE}{dx} \right\rangle' = \left\langle \frac{dE}{dx} \right\rangle(Alog_{10}(\left\langle \frac{dE}{dx} \right\rangle x10^{-6}) + B) \qquad (4.4)$$

The four parameters, ζ, κ, A and B, are obtained by fitting $\langle dE/dx \rangle$ (truncated mean determined by rejecting the top 20% of samples) histograms projected for narrow slices in rigidity. Only the regions in which all particle bands are clearly separated were sliced into $\langle dE/dx \rangle$ projections. For positively charged particles, the rigidity range was restricted to 0-1 GeV/c, while the negatively charged particles (mostly pions) were fit over the range 0-15 GeV/c. The width of these slices is narrowest at low rigidity to account for the rapidly changing $\langle dE/dx \rangle$ and broader beyond minimum ionizing, where $\langle dE/dx \rangle$ is fairly flat as a function of rigidity.

Two additional track quality cuts were applied to the data used to extract the

Bethe-Bloch parameters. Tracks with fewer than 50 hits were excluded from the projections. In addition, a cut was made on the fraction of observed hits compared with the number of expected hits for a given track. Tracks with fewer than 50% of their expected hits observed by the TPC were excluded from the projections. The combination of these two cuts improves the $\langle dE/dx \rangle$ resolution, which in turn improves the determination of the mean value.

The projections were fit with a Gaussian model of the single particle mean energy loss to obtain the height, width and mean value for each particle type in a given rigidity slice. By converting the mean rigidity of each slice to $\beta\gamma$ for a given mass, the mean values for all particles can be plotted together on Figure 4.2 and fit with the Scott parameterization, Equation 4.4.

The results of these fits are used to extend particle identification (PID) into the region where the particle bands overlap on the $\langle dE/dx \rangle$-rigidity plot by fixing the mean value for each particle. This technique greatly improves upon the standard PID method of drawing graphical bands around particles in the well-separated regions.

4.3 $\langle dE/dx \rangle$ Distribution Parameterization

In the beam energy range studied here, the predominant contribution to the negative particle yields over all rigidity comes from π^-. Electrons contribute approximately 10% in the worst case and fall significantly as a function of their transerve

6 GeV/A Au+Au

ζ_1: 0.141002
κ_1: 6.69746
A_1: 1.36289E-05
B_1: -6.29191E-05

ζ_2: 0.100089
κ_2: 14.8185
A_2: 2.74838E-06
B_2: -4.94447E-06

$\langle dE/dx \rangle$ (arbitrary units)

10^{-3}

10^{-4}

10^{-5}

○ π^+
● π^-
▲ p
■ d
★ k^+

$(dE/dx)_{raw} = \zeta/\beta^2\{\kappa + \ln(\beta\gamma)^2 - 2\beta^2\}$

$(dE/dx)_{corr} = (dE/dx)_{raw}(A\log_{10}((dE/dx)_{raw} \times 10^6) + B)$

10^{-1} 1   10

$\beta\gamma$
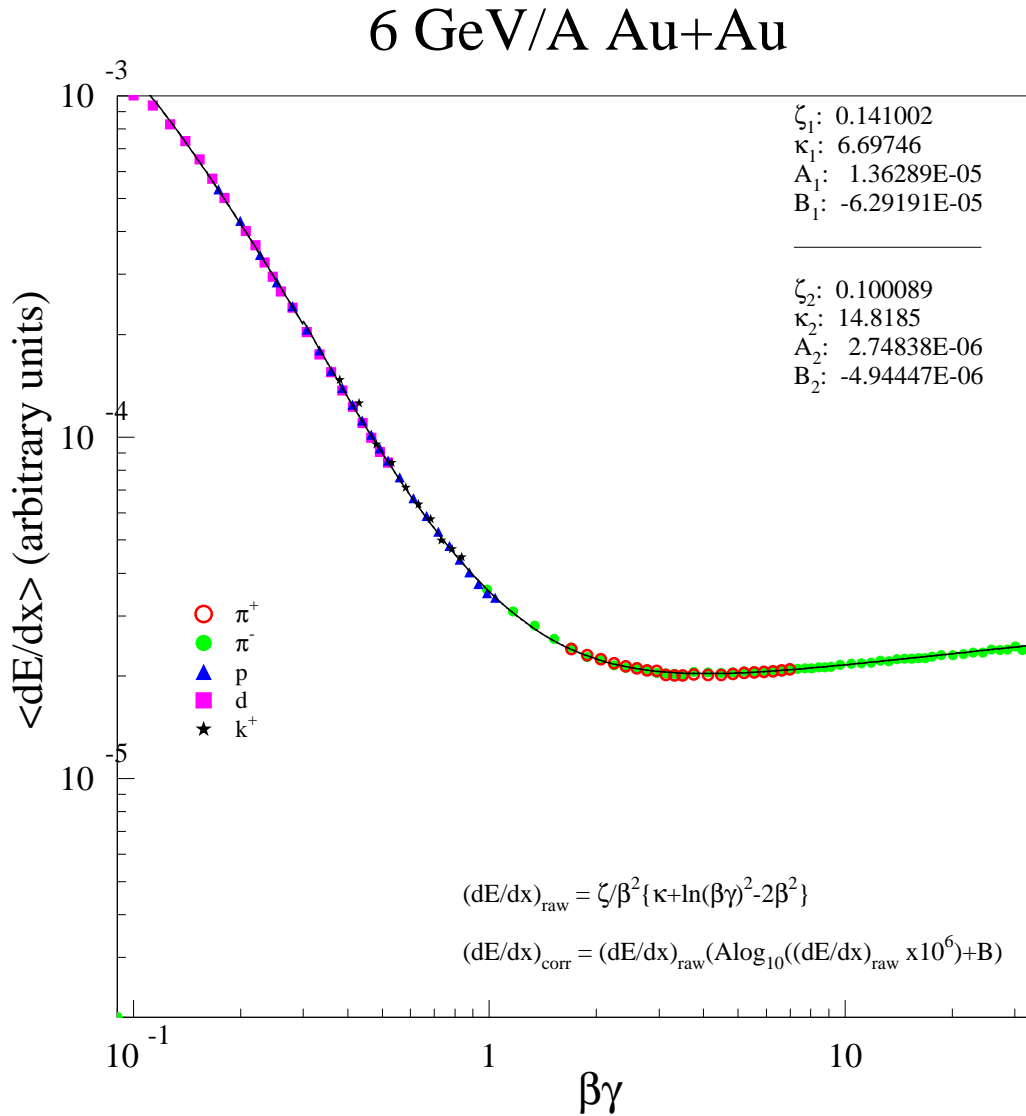
Figure 4.2: Parameterized Bethe-Bloch function (Equation 4.4) of the average energy loss, fit to extracted mean values for pions (both positive and negative), kaons, protons and deuterons at 6 AGeV. The first set of Scott parameters is used for $\beta\gamma < 0.3$, while the second set of parameters applies for $\beta\gamma \geq 0.3$.

momentum. A comparison of the total number of mid-rapidity π^- measured in E895 and K^- measured by E866/E917 for the same beam energy range[Dunl99] indicates that kaons are a 0% to $\sim$2% contaminant (for 2 - 8 AGeV). This naturally suggests that the π^- are the best candidate for studying the shapes of the $\langle dE/dx \rangle$ distributions. Since the $\langle dE/dx \rangle$ resolution depends on the number of hits used to compute the mean, and the number of hits is a function of the particle's rigidity, the behaviour of the $\langle dE/dx \rangle$ distributions as a function of rigidity must be explored.

4.3.1   Two-Gaussian Model

The shapes of the individual particle distributions are optimized from an extensive iterative study of the relatively clean π^- distributions. Since the truncation technique applied to obtain $\langle dE/dx \rangle$ did not remove all of the high-dE/dx tail, and our data are integrated over N_{hits}, a simple Gaussian function is inadequate to describe the single-particle distributions. The asymmetry is smaller if narrow N_{hits} ranges are used, but due to our already limited statistics, the decision was made to parameterize N_{hits} integrated shapes. A two-Gaussian model was chosen to best fit the observed distributions. The main Gaussian characterizes the majority of the distribution, while the high-$\langle dE/dx \rangle$ tail is approximated by the second, smaller offset Gaussian. The "shoulder" Gaussian is related to the main Gaussian through three shape parameters: ϵ, the ratio of the shoulder Gaussian mean to the main Gaussian mean, α, the ratio

of their amplitudes, and ρ, the ratio of their widths.

$$N_{\pi^-} = A \left[e^{-0.5\left(\frac{x-<x>}{\sigma}\right)^2} + \alpha e^{-0.5\left(\frac{x-\epsilon<x>}{\rho\sigma}\right)^2} \right] \qquad (4.5)$$

As mentioned above, the pions dominate the negative particle species, with some contribution from kaons and electrons. In addition, pairs of pions with nearly the same momenta that are nearby in space ionize with twice the signal of a single pion. The total number of these correlated pions is observed at a level about 5% of the single pion yield. Each $\langle dE/dx \rangle$ distribution projected from the negative particles is therefore fit with a sum of four single-particle two-Gaussian models.

$$N_{neg} = \sum_{i=1}^{4} N_i \qquad (4.6)$$

The positively charged species contributing to the distributions include positrons, pions, correlated pions, kaons, protons, correlated protons, deuterons (Z=1,A=2), tritons (Z=1,A=3), and helions (Z=2,A=3). The probability for alpha (Z=2,A=4) formation is reduced by a factor of $\sim$1000 compared to helion formation at these energies, so all Z=2 particles are tagged as helions.

$$N_{pos} = \sum_{i=1}^{9} N_i \qquad (4.7)$$

Since particle identification via $\langle dE/dx \rangle$ depends on the region of rigidity space studied, more details of how this model is used will be discussed in Chapter 5 and in Appendix A.

Chapter 5

Obtaining Particle Spectra

5.1 Kinematic Variables

In accelerator experiments, all the initial energy is directed along the beam axis (longitudinally), but a significant portion of this energy is redistributed into transverse motion during the violent collision process. The collision is asymmetric in a fixed target experiment where the target is at rest with respect to a beam particle. However, in the center of momentum frame, the collisions are longitudinally symmetric. By boosting to this frame, the analysis can take advantage of the forward/backward directional symmetry.

The TPC measures the Cartesian rigidity components, r_x, r_y and r_z, in the laboratory frame. The momentum is related to the rigidity by $\vec{p}=Z*\vec{r}$. For charge $|Z|=1$ particles, rigidity and momentum are identical. The center of mass velocity, gamma boost and rapidity of the collision can be computed from the beam kinetic energy (Table 5.1)

$$\beta_{cm} = \frac{\sqrt{((E_{kin} + 0.9315)^2 - 0.9315^2)}}{E_{kin} + 2(0.9315)} \tag{5.1}$$

$$\gamma_{cm} = \frac{1}{\sqrt{1 - \beta_{cm}^2}} \tag{5.2}$$

$$y_{cm} = \frac{1}{2}ln\left(\frac{1 + \beta_{cm}}{1 - \beta_{cm}}\right). \tag{5.3}$$

The "natural" variables used for studying the momentum spectra of particles emitted from heavy ion collisions are transverse mass, a scaled p_t variable, and rapidity, a longitudinal relativistic velocity variable, in the center of momentum (CM).

	2 AGeV	4 AGeV	6 AGeV	8 AGeV
E_{kin} (AGeV)	1.85	3.91	6.00	8.00
β_{beam}	0.9425	0.9813	0.9909	0.9945
γ_{beam}	2.9860	5.1975	7.4412	9.5883
y_{beam}	1.7598	2.3320	2.6956	2.9510
$\sqrt{s}$ (AGeV)	2.630	3.279	3.838	4.289
β_{cm}	0.7059	0.8230	0.8741	0.9006
γ_{cm}	1.4117	1.7600	2.0600	2.3010
y_{cm}	0.8789	1.1660	1.3478	1.4755

Table 5.1: Beam and Center of Momentum variables at each beam energy.

This is because some of the collision energy, initially directed totally along the beam direction, is re-directed during the collision into the transverse direction. For a large ensemble of events, the direction of the impact parameter vector is randomly distributed in azimuth. In addition, any azimuthal asymmetries due to finite impact parameter should be small for the centrality range of interest, b $\simeq$ 3.3 fm. Therefore, the data analysed for this thesis are integrated over all azimuthal angles.

Although p_t is unaffected by a boost between the lab and CM frames,

$$p_t = \sqrt{p_x^2 + p_y^2} \tag{5.4}$$

$$m_t - m_0 = \sqrt{p_t^2 + m_0^2} - m_0 \tag{5.5}$$

$$p_z^{cm} = \gamma_{cm}(p_z^{lab} - \beta_{cm}E_{tot}) \tag{5.6}$$

rapidity depends on p_z, and therefore must be transformed between frames.

$$E^2 = p_x^2 + p_y^2 + p_z^2 + m_0^2 \tag{5.7}$$

$$y = \frac{1}{2}ln(\frac{E + p_z}{E - p_z}) \tag{5.8}$$

$$y^{cm} \quad = \quad y + y_{cm} \qquad (5.9)$$

The advantage of using the rapidity variable is that it is additive under a Lorentz boost, so transforming between frames is simple compared to the conversion for p_z. Both m_t-m_0 and rapidity depend on mass, which requires a PID assignment before these variables can be computed.

5.2 Mass hypothesis and data binning

In early explorations of extracting the particle momentum spectra, we attempted to use a probabilistic determination of the PID for a given track based on total momentum, a prescription dubbed UCDPID. (See Appendix B) After assigning the mass, the spectra variables were computed and the data sorted into $(m_t$-$m_0,y)$ bins. Unfortunately, this posed significant contamination problems, due to the fact that two tracks with the same total momentum might have radically different p_t and rapidity:

$$p_{tot} = \sqrt{p_t^2 + p_z^2}$$
$$m_t = \sqrt{p_t^2 + m_0^2} \qquad (5.10)$$
$$p_z = m_t \sinh(y)$$

For a given momentum, the relative population in $\langle dE/dx \rangle$ of different particles depends on the m_t-m_0 and rapidity. In order to correctly determine the $\langle dE/dx \rangle$ relative populations, the particle identification needs to be determined *after* the m_t-m_0 and

rapidity are calculated. There is a Catch-22, however, since the calculation of m_t-m_0 and rapidity requires knowledge of the particle mass.

To address this issue, an alternative PID method (called the "Mass Assumption" Method) was developed, which builds on the general ideas of UCDPID, but which does not employ that method directly. For each particle of interest (pions and protons), a "mass and charge assumption" [1] is made by tentatively assigning to all tracks in an event the mass and Z of the particle of interest. Using this mass and Z and the rigidity components from the TPC, the postulated center of momentum rapidity and m_t-m_0 are computed and the data are sorted into bins of m_t-m_0 and rapidity. (To go to the (m_t-m_0,y) coordinates the particle mass and charge must be known.) The rapidity bins are each 0.1 units wide, with the mid-rapidity slice covering -0.05 < y - y_{cm} < 0.05. In order to cover the entire range from beam to target rapidity, there are (19,25,29,31) rapidity bins at (2,4,6,8) AGeV. The m_t-m_0 bins are 25 MeV/c^2 wide and span the range $0 < m_t\text{-}m_0 < 1.0$ GeV/c^2. Similar to UCDPID, $\langle dE/dx \rangle$ histograms are projected out of the data in these bins and fit for the total yield of the particle of interest. Particles of the wrong mass and/or charge in a given (m_t-m_0,y) bin are recognized and later rejected by the relationship between their momenta and $\langle dE/dx \rangle$. In contrast to UCDPID, the data are binned in (m_t-m_0,y) first, and then

---

[1]It is important to note that in the pion and proton mass assumptions, momentum and rigidity ($\vec{r}=\vec{p}/Z$) are identical since |Z|=1 for pions and protons. For a given proton or pion "assumption" (m_t-m_0,y), the helion contaminants (Z=2) come from a total momentum that is a factor of two larger than the pion and proton momenta.

$0 < \mathrm{m}_t\text{-}\mathrm{m}_0 < 1.0$ GeV/c^2	2 AGeV	4 AGeV	6 AGeV	8 AGeV
$\Delta\mathrm{p}_{tot}(\pi)$ (GeV/c)	0.14 - 1.60	0.20 - 2.00	0.25 - 2.34	0.29 - 2.62
$\Delta\mathrm{p}_{tot}(\mathrm{k})$ (GeV/c)	0.49 - 2.05	0.72 - 2.58	0.89 - 3.03	1.02 - 3.40
$\Delta\mathrm{p}_{tot}(\mathrm{p})$ (GeV/c)	0.94 - 2.57	1.36 - 3.28	1.68 - 3.87	1.94 - 4.36
$\Delta\mathrm{p}_{tot}(\mathrm{d})$ (GeV/c)	1.87 - 3.60	2.72 - 4.70	3.37 - 5.60	3.89 - 6.35

Table 5.2: Lab momentum ranges for mid-rapidity particles with $0 < \mathrm{m}_t\text{-}\mathrm{m}_0 < 1.0$ GeV/c^2.

their PID is determined. In all, over 16,000 individual histograms are fit multiple times to extract the final momentum spectra for π^-, π^+ and protons.

By computing the mean total momentum at the center of the bin, the $\langle \mathrm{dE/dx} \rangle$-momentum trajectory can be mapped. Table 5.2 lists the range of lab momentum spanned for particles at mid-rapidity within the m_t-m_0 range of interest. A comparison with Figure 4.1 reveals that these mid-rapidity ranges extend into regions where the positive particle bands merge. The contribution to the total observed yield from each particle type is deconvoluted using the Bethe-Bloch parameterization and a table of shape parameters (see Appendix A) to fix the distribution shapes. The only free parameters in the fits are the total yield of each species and an overall $\langle \mathrm{dE/dx} \rangle$ gain parameter. The kaon yields, which contaminate the π^-, π^+, and proton distributions, are fixed in all of the fits using information from the E866/E917 experiments. (Details of these yields and how they are determined are contained in Appendix C.)

5.3   Pion Fitting

The complexity of this analysis is a function of the particle of interest. Of the particles of interest, the negative pions are the simplest to extract, since they have the least contamination due to other particle species. The $\langle dE/dx \rangle$ fits require the fewest assumptions and can be fit over the entire range of momentum we are interested in characterizing. The $\langle dE/dx \rangle$ distribution shape parameters are extracted from the data (Appendix A) and then fixed, along with the kaon yields in a subsequent fit for the final pion yields. Figure 5.1 shows an example of a negatively charged particle $\langle dE/dx \rangle$ projection in the pion mass hypothesis (described in the previous section) at 6 AGeV mid-rapidity for $0.125 < m_t\text{-}m_0 < 0.150 \,\text{GeV}/\text{c}^2$. By combining the extracted yields from each $(m_t\text{-}m_0,y)$ bin, the raw spectra of π^- over all momentum space can be assembled.

Since the shape parameters are primarily a function of the momentum, through their dependence on N_{hits}, the positive pion $\langle dE/dx \rangle$ distributions are assumed to have the same shapes as the negative pions. Consequently, the positive pions can be similarly extracted, fixing the kaons and applying the negative pion shape parameters for all $(m_t\text{-}m_0,y)$ bins with $p_{lab} < 1.2 \,\text{GeV}/\text{c}$. Figure 5.2 shows the positively charged particle $\langle dE/dx \rangle$ projection in the same $(m_t\text{-}m_0,y)$ bin as in Figure 5.1: the pion mass hypothesis at 6 AGeV mid-rapidity for $0.125 < m_t\text{-}m_0 < 0.150 \,\text{GeV}/\text{c}^2$. The only difference is the particle charge. For $p_{lab} > 1.2 \,\text{GeV}/\text{c}$, the π^+ yields are

falling exponentially while the proton yields are significant, making it impossible to separately determine the small pion contribution to the merged distribution. Despite this cut-off, the raw yields from the positive pions as a function of (m_t-m_0,y) in the limited momentum range, $0 < p_{lab} < 1.2$ GeV/c can be successfully extracted.

5.4   Pion Ratios

Experimentally, the TPC particle detection efficiency is independent of the sign of the particle charge. Corrections for positive and negative particles studied with simulations and with empirical forward to backward rapidity comparisons are identical to all attainable levels of precision. Therefore, ratios of like-mass, oppositely charged particles need not be corrected for detection efficiency. Figures 5.3, 5.4, 5.5, and 5.6 show the ratio of positive to negative pion yields as a function of m_t-m_0 for mid-rapidity (black triangles in the first panel) and each successive rapidity bin (forward bins are shown as green squares, while backward bins are plotted as red circles on the same panel).

A functional form to fit the observed ratios may be derived if the asymmetry between the charged pion momentum spectra is interpreted as the result of an electromagnetic interaction with the net positive charge deposited in the collision zone by the incoming nuclei. In the simplest assumption, the nuclear matter is completely stopped at impact and forms a sphere of uniform charge density at the center of mo-

6 AGeV, Mtbin 6, ybin 0
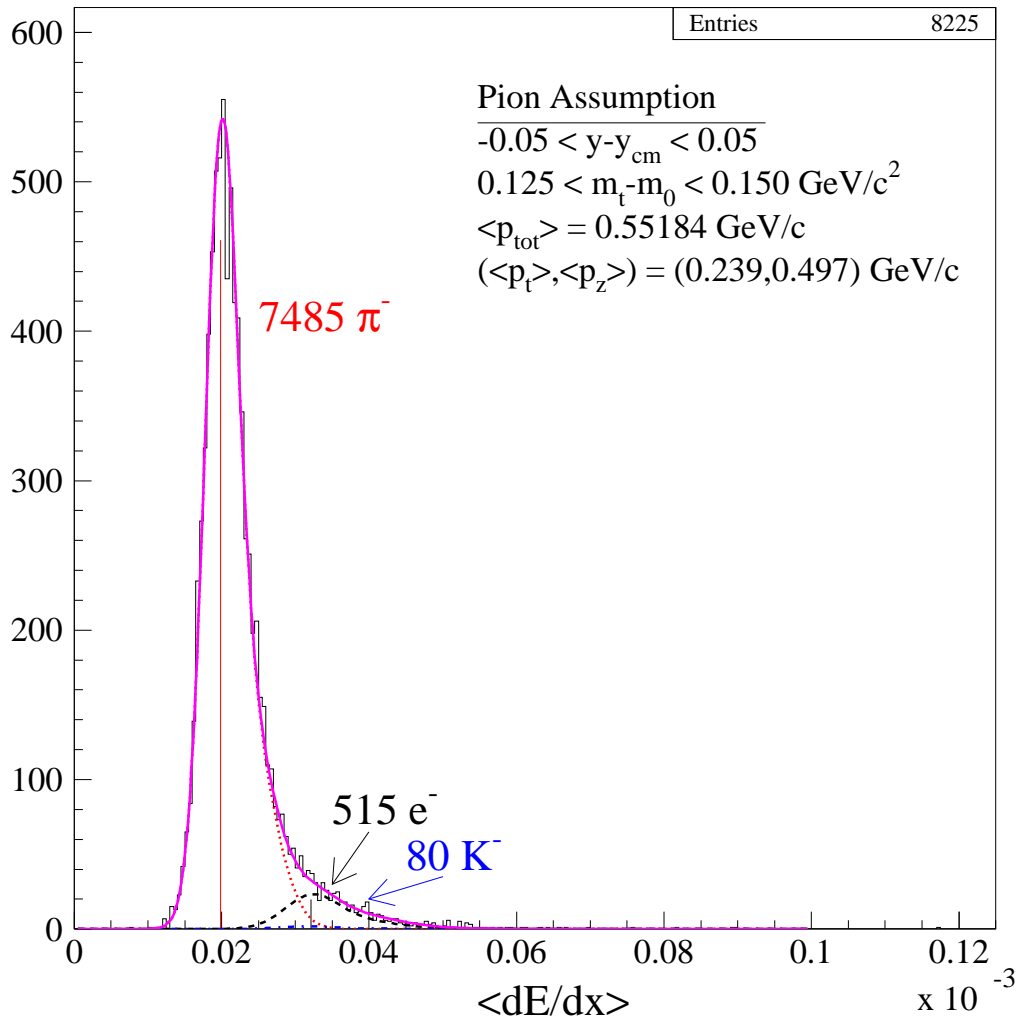
Figure 5.1: Negative particle $\langle dE/dx \rangle$ projection in the pion mass assumption at 6 AGeV mid-rapidity, $0.125 < m_t\text{-}m_0 < 0.150$ GeV/c^2

6 AGeV, Mtbin 6, ybin 0

Entries   8645

Pion Assumption
$\overline{-0.05 < y\text{-}y_{cm} < 0.05}$
$0.125 < m_t\text{-}m_0 < 0.150 \text{ GeV/c}^2$
$<p_{tot}> = 0.55184 \text{ GeV/c}$
$(<p_t>,<p_z>) = (0.239, 0.497) \text{ GeV/c}$

5654 π^+

448 e^+

283 K^+

1852 p

$<dE/dx>$ x 10^{-3}
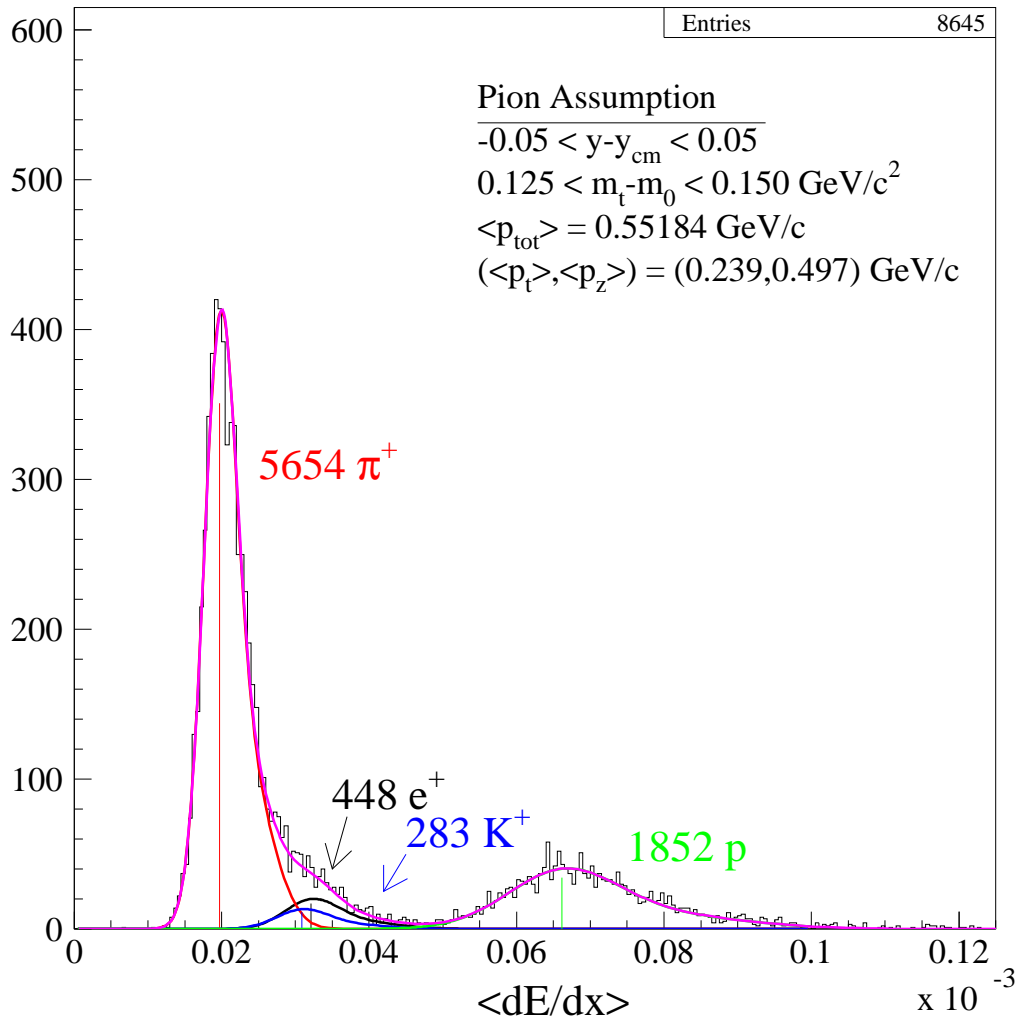
Figure 5.2: Positive particle $\langle dE/dx \rangle$ projection in the pion mass assumption at 6 AGeV mid-rapidity, $0.125 < m_t\text{-}m_0 < 0.150 \text{ GeV/c}^2$
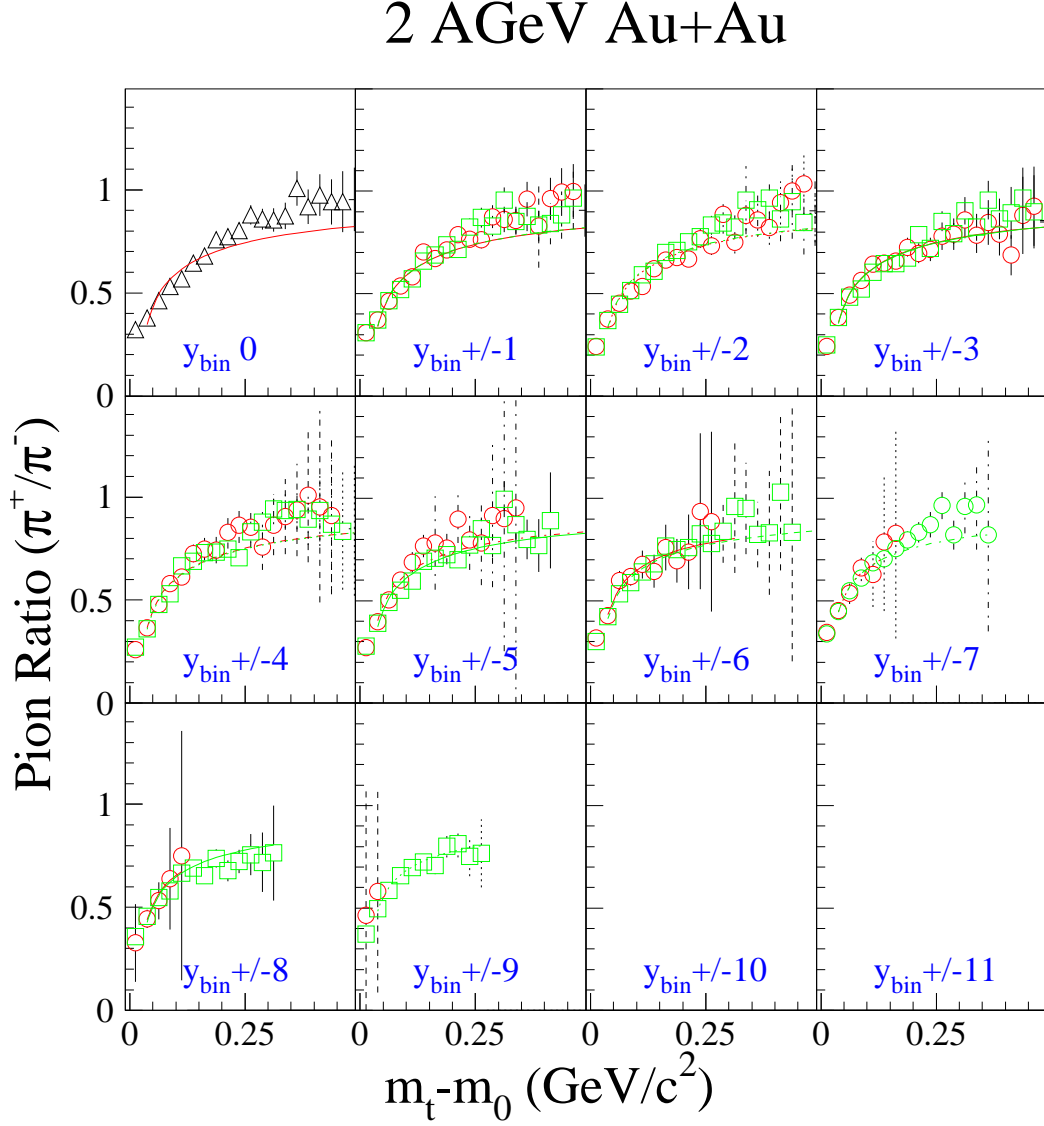
Figure 5.3: Pion ratios as a function of m_t-m_0 for mid-rapidity (first panel) and each successive rapidity bin (forward bins are shown as green squares while backward bins are shown as red circles, plotted on the same panel) at 2 AGeV. The red and green lines are fits to the ratio data using Equation 5.16.

4 AGeV Au+Au
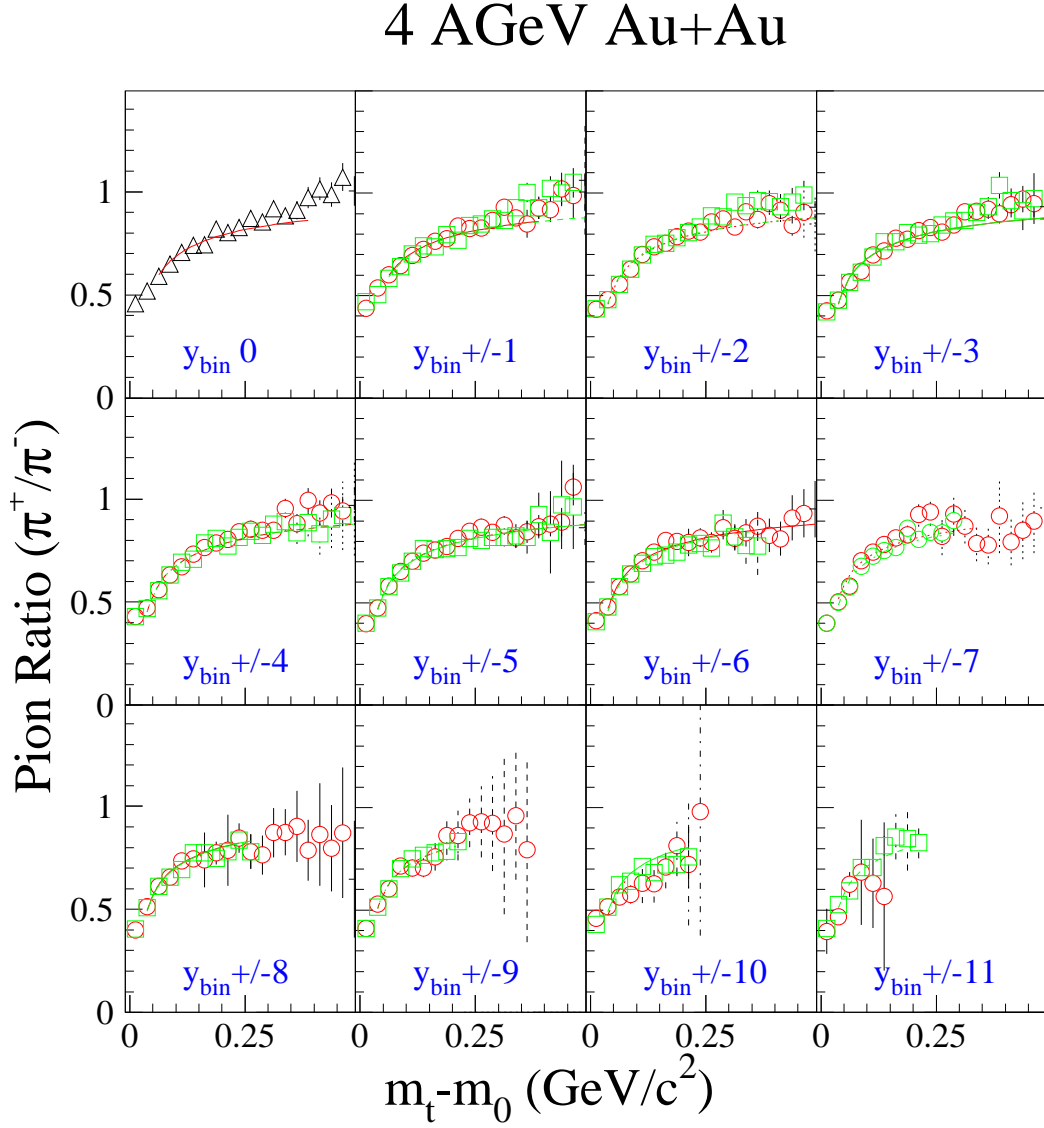
Figure 5.4: Pion ratios as a function of m_t-m_0 for mid-rapidity (first panel) and each successive rapidity bin (forward bins are shown as green squares while backward bins are shown as red circles, plotted on the same panel) at 4 AGeV. The red and green lines are fits to the ratio data using Equation 5.16.

6 AGeV Au+Au
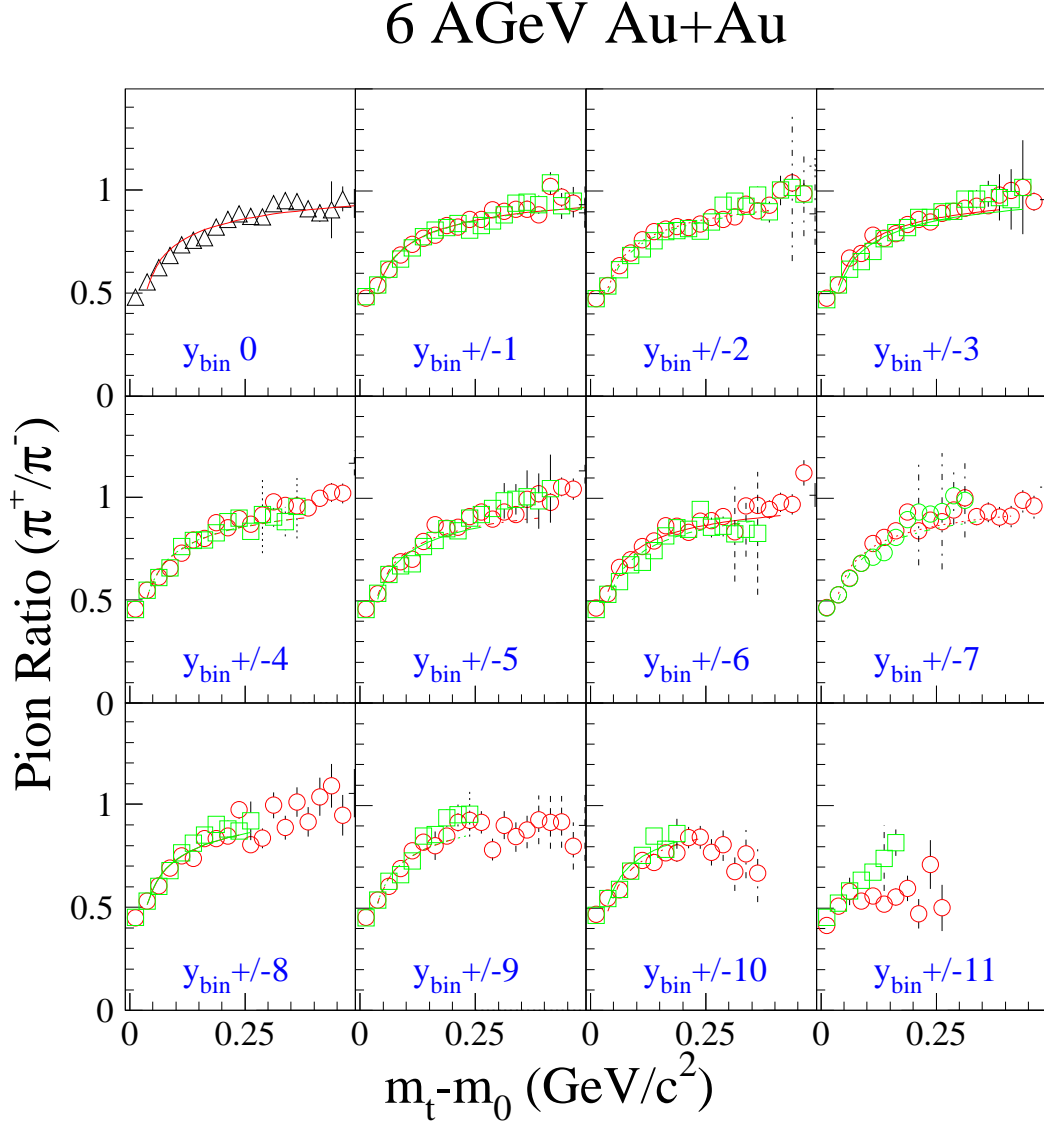
Figure 5.5: Pion ratios as a function of m_t-m_0 for mid-rapidity (first panel) and each successive rapidity bin (forward bins are shown as green squares while backward bins are shown as red circles, plotted on the same panel) at 6 AGeV. The red and green lines are fits to the ratio data using Equation 5.16.

8 AGeV Au+Au
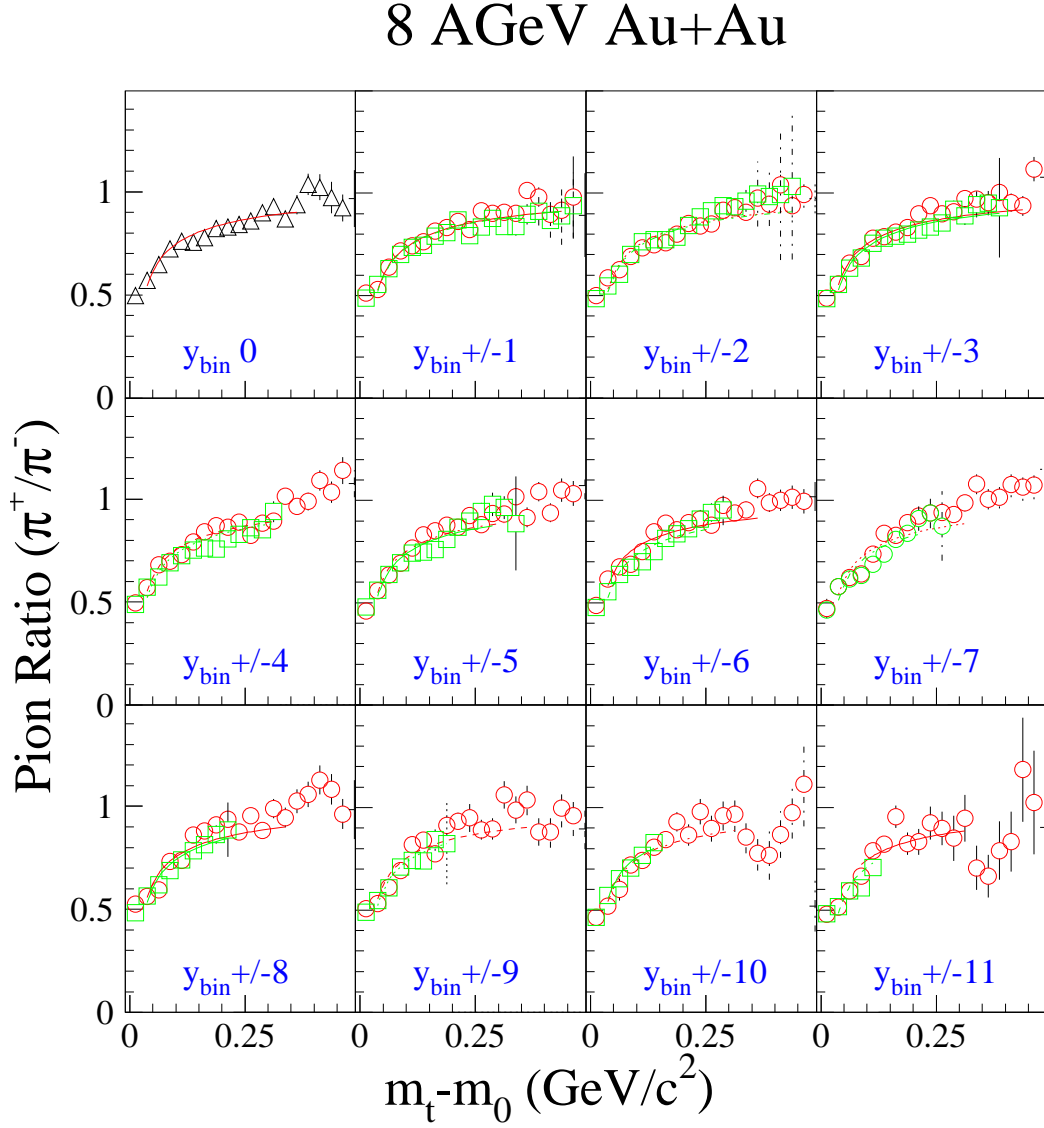
Figure 5.6: Pion ratios as a function of m_t-m_0 for mid-rapidity (first panel) and each successive rapidity bin (forward bins are shown as green squares while backward bins are shown as red circles, plotted on the same panel) at 8 AGeV. The red and green lines are fits to the ratio data using Equation 5.16.

mentum. The interaction can be interpreted as a static long-range Coulomb attraction for the π^- and a Coulomb repulsion for the π^+.[Gyul81],[Li95],[Osad96] Although the dynamics are much more complicated than this [Ayal99],[Barz98], for the sake of an analytical tool, the simple model is sufficient.[2]

Before freeze-out, the dynamics of the system are dominated by strong interactions. The Coulomb effect becomes important only after freeze-out, when the system has expanded to the point where strong interactions cease. At this point, the total yields are essentially fixed and only the final state energy and momenta are modified by the field. In the simplest treatment of a static uniformly charged sphere of total charge Z and radius R, located at mid-rapidity, the average Coulomb potential of the source is

$$V_C = \frac{6}{5} \frac{Ze^2}{R}. \tag{5.11}$$

The Coulomb field radially accelerates all free-streaming charged particles; negatively charged particles are attracted to the source while positively charged particles are repulsed. Slow pions, as the lightest hadronic collision products, experience the largest relative effect, a decrease in their total energy for pi-minus and an increase for pi-plus.

$$E = E_0 \pm V_C \tag{5.12}$$

---

[2]For this analysis, the goal of characterizing the pion ratios is simply to be able to remove π^+ contamination from the $\langle dE/dx \rangle$ distributions of the protons. A more extensive analysis including dynamical effects is currently under investigation by D. Cebra[Cebr01].

Only the momentum and energy are effected by the Coulomb field; the number of pions before and after the modification (Equation 5.12) is the same: $d^3N_0 = d^3N$. If the pions are assumed to have an underlying thermal distribution

$$E_0 \frac{d^3 N_0}{dp_0^3} \sim E_0 e^{-E_0/T} \tag{5.13}$$

the thermal spectrum is modified by this effect:

$$E \frac{d^3 N}{dp^3} = E_0 \frac{d^3 N_0}{dp_0^3} \frac{dp_0^3}{dp^3} = E_0 \frac{d^3 N_0}{dp_0^3} \frac{p_0}{p} \sim E_0 e^{-E_0/T} \frac{\sqrt{E_0^2 - m_0^2}}{\sqrt{(E_0 \pm V_C)^2 - m_0^2}} \tag{5.14}$$

Equation 5.14 must be rewritten in terms of the measured final state quantities using Equation 5.12.

$$E \frac{d^3 N}{dp^3} \sim (E \mp V_C) e^{-E \mp V_C/T} \frac{\sqrt{(E \mp V_C)^2 - m_0^2}}{\sqrt{E^2 - m_0^2}} \tag{5.15}$$

The energy shift transforms the measured momenta, manifest as a low-p_t enhancement for π^- and a low-p_t depletion for π^+. The ratio of the yields of positive and negative pions as a function of m_t-m_0 takes the form

$$\frac{\pi^+}{\pi^-} = R_\pi \frac{(E - V_C)}{(E + V_C)} \frac{\sqrt{(E - V_C)^2 - m_0^2}}{\sqrt{(E + V_C)^2 - m_0^2}} \tag{5.16}$$

The parameter R_π is the ratio of the yields of positive to negative pions at high m_t-m_0, and V_C is the effective Coulomb potential, which is related to the dip in the observed ratios at low m_t-m_0. The lines on Figures 5.3, 5.4, 5.5, and 5.6 are the result of fitting Equation 5.16 to the measured pion ratios at each rapidity slice. Using this parameterization, the pion ratios may be extrapolated over the full range in m_t-m_0.

For this analysis, Equation 5.16 is evaluated in the longitudinally co-moving frame of the pions traveling within a given rapidity slice. That is, the energy E, is taken to be m_t only; the explicit rapidity dependence in $E = m_t \cosh(y)$ is removed by the boost to the frame of the pions. This gives V_C and R_π values which are different from the V_C and R_π associated with the center of momentum frame of the collision. It is observed experimentally that the asymptotic ratio parameter, R_π, evaluated in this way is nearly flat as a function of rapidity, while V_C shows an approximately Gaussian behaviour as a function of rapidity. In order to improve the determination of V_C, R_π is fixed to the average value in a second fit to the pion ratios. Figure 5.7 shows the effective Coulomb potential as a function of rapidity extracted from these fits at all four beam energies. They are fit with Gaussian parameterizations to extrapolate to the tails of the rapidity range, where the ratios are less well-behaved. Both the most forward and backward regions are statistics-limited; the most forward bins suffer from the momentum cut-off imposed on the π^+ by the protons. The effective Coulomb potential is nevertheless observed to decrease from 2 AGeV to 8 AGeV. Table 5.3 lists the fit parameters from the Gaussian parameterization and the average values of R_π extracted for each beam energy.
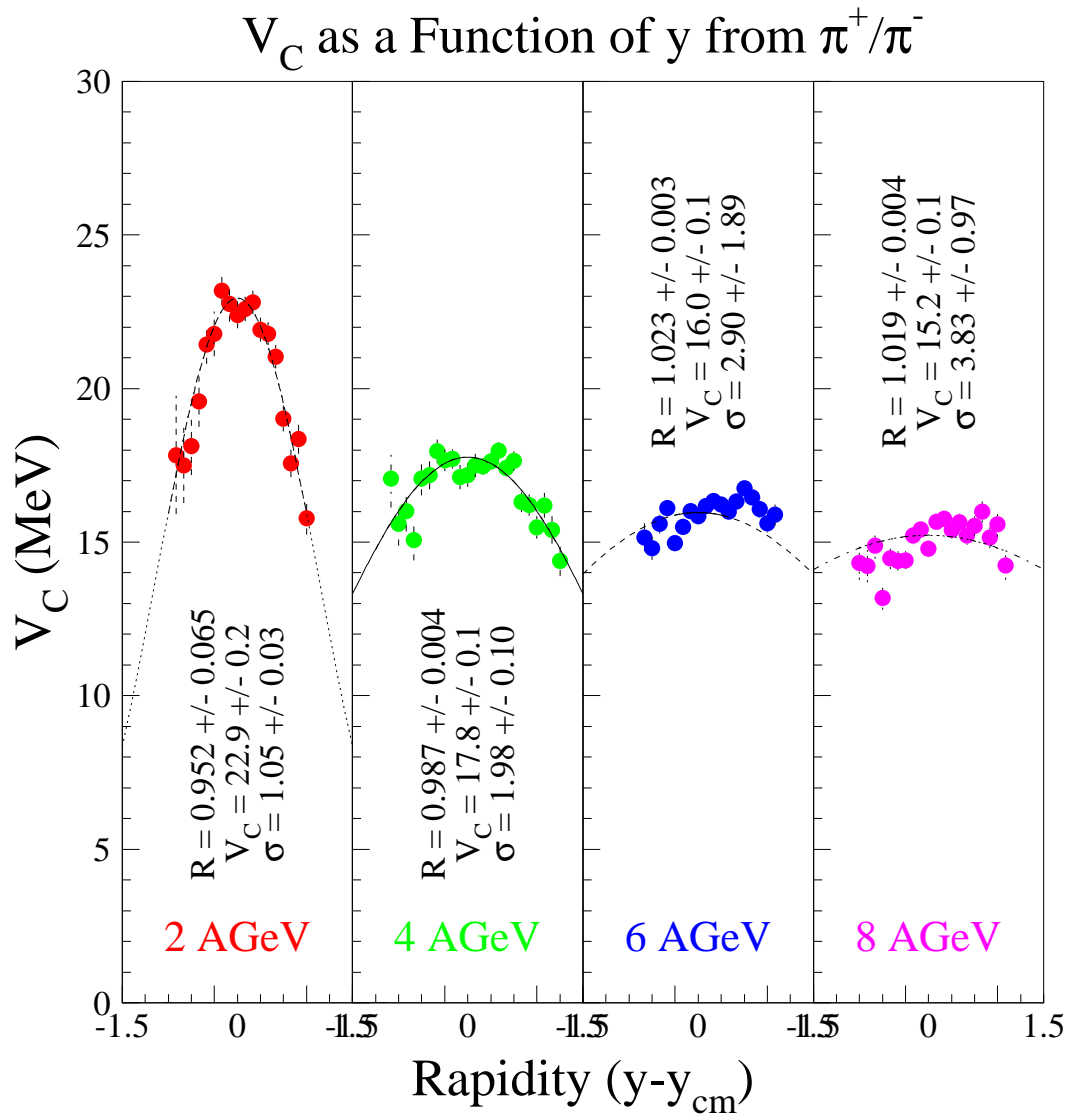
Figure 5.7: Effective Coulomb Potential as a function of rapidity for a fixed asymptotic ratio of pions in the longitudinally co-moving frame at 2,4,6, and 8 AGeV.

	2 AGeV	4 AGeV	6 AGeV	8 AGeV
V_C (MeV)	22.9 ± 0.2	17.8 ± 0.1	16.0 ± 0.1	15.2 ± 0.1
σ_{V_C}	1.05 ± 0.03	1.98 ± 0.10	2.90 ± 1.89	3.83 ± 0.97
$R_\pi(\pi^+:\pi^-)$	0.952 ± 0.065	0.987 ± 0.004	1.023 ± 0.003	1.019 ± 0.004

Table 5.3: Fit parameters extracted from Pion Ratios in the longitudinally co-moving frame of the pions at each beam energy.

5.5   Proton Fitting

Extracting the proton spectra is much the same as the positive pions, with the addition of a few crucial steps. First, as with the π^+'s, the two-Gaussian model $\langle dE/dx \rangle$ distribution shape parameters are characterized by studying the negative particles in the proton mass assumption. That is, the $(m_t\text{-}m_0,y)$ of the negative particles (mostly pions) are computed using the proton mass. The lab momenta (p_t, p_z), of the negative particles for these calculated $(m_t\text{-}m_0,y)$ are the same as for the actual positively charged proton candidates. Since the $\langle dE/dx \rangle$ resolution depends on N_{hits}, which in turn depends on momentum, binning the negative particles this way implies that they should have similar N_{hits} distributions and momentum resolution as the proton candidates. Therefore, the negative particle $\langle dE/dx \rangle$ distribution shapes should be identical to the positive particle $\langle dE/dx \rangle$ distribution shapes for the identical mass assumption. This is true over most of the phase space covered by the detector. The proton shape parameter optimization is detailed along with the pion optimization in Appendix A.

In the lab momentum range between 0 and 1 GeV/c, the proton band is well-

separated from other particle species, so the particle identification is trivial. Similar to the pion fits, kaon contamination is removed following the prescription in Appendix C. However, beyond $p_{lab} \sim 1.2$ GeV/c, the pions become a contaminant which must be removed from the proton fits in order to extract reliable proton yields. This is accomplished using the pion ratios introduced in the preceding section.

5.5.1 Pion Subtraction

The negative particle distributions in the proton mass assumption used to optimize the shapes of the proton distributions are also used to determine the negative pion yields in each $(m_t\text{-}m_0,y)_{pro}$ bin. Proton $m_t\text{-}m_0$ and rapidity can be transformed to the pion $m_t\text{-}m_0$ and rapidity since they come from the same lab p_x, p_y and p_z. For example, at 4 AGeV mid-rapidity ($y_{CM} = 1.166$), in the third proton $m_t\text{-}m_0$ bin (50 $< m_t\text{-}m_0 < 75$ MeV), $p_t = 0.348$ GeV/c, $p_z = 0.145$ GeV/c, and $p_{tot} = 1.491$ GeV/c in the lab frame. Transforming to the pion $m_t\text{-}m_0$ and rapidity

$$E_\pi = \sqrt{p_{tot}^2 + m_\pi^2} = 1.498 GeV$$

$$m_t - m_\pi = \sqrt{p_t^2 + m_\pi^2} - m_\pi = 0.235 GeV$$

$$y_\pi^{CM} = \frac{1}{2}\log(\frac{E_\pi + p_z}{E_\pi - p_z}) - y_{CM} = -1.069,$$

the pion ratio for these $(m_t\text{-}m_0,y)_\pi$ coordinates may be predicted from the parameterizations in Table 5.3 and folded with the observed yield of negative pions in this proton bin to fix the positive pion yield. Figure 5.8 shows the $\langle dE/dx \rangle$ histogram

for this bin and the corresponding positive pion yield which was subtracted from the fit; the total yields of other contaminating particles (*e.g.* d,t,^{3}He) are allowed to be free parameters. A test of the pion subtraction method is available in the regions of phase space where the pion and proton distributions are well-separated. The ratio method accurately predicts (within 10%) the observed values, suggesting that this method should also work where the pion and proton distributions completely overlap. The absence of seams in the proton spectra in the transition region where the pions become fixed to the predicted values is an additional indicator of the validity of the method. In the region of momentum where total overlap occurs, the pions contaminate predominantly the very lowest bins of the proton m_t-m_0. Beyond the very lowest bins, the contamination is small and decreasing exponentially.

5.5.2 Deuteron-Triton Confusion

Near the lab momentum of 5.8 GeV/c, the ability to resolve the declining proton signal from the deuteron and triton species becomes increasingly difficult. The centroids of these three particle bands cross in such a way that there is a range of momentum ($\sim$ 5.8 - 7.8 GeV/c) over which the contributions from these three species cannot be disentangled. Since there are virtually no anti-deuterons and anti-tritons, there is no way to remove the deuteron and triton contamination from the $\langle dE/dx \rangle$ distribution fits that is analogous to the pion subtraction. The Bethe-Bloch

4 AGeV, Mtbin 3, ybin 0
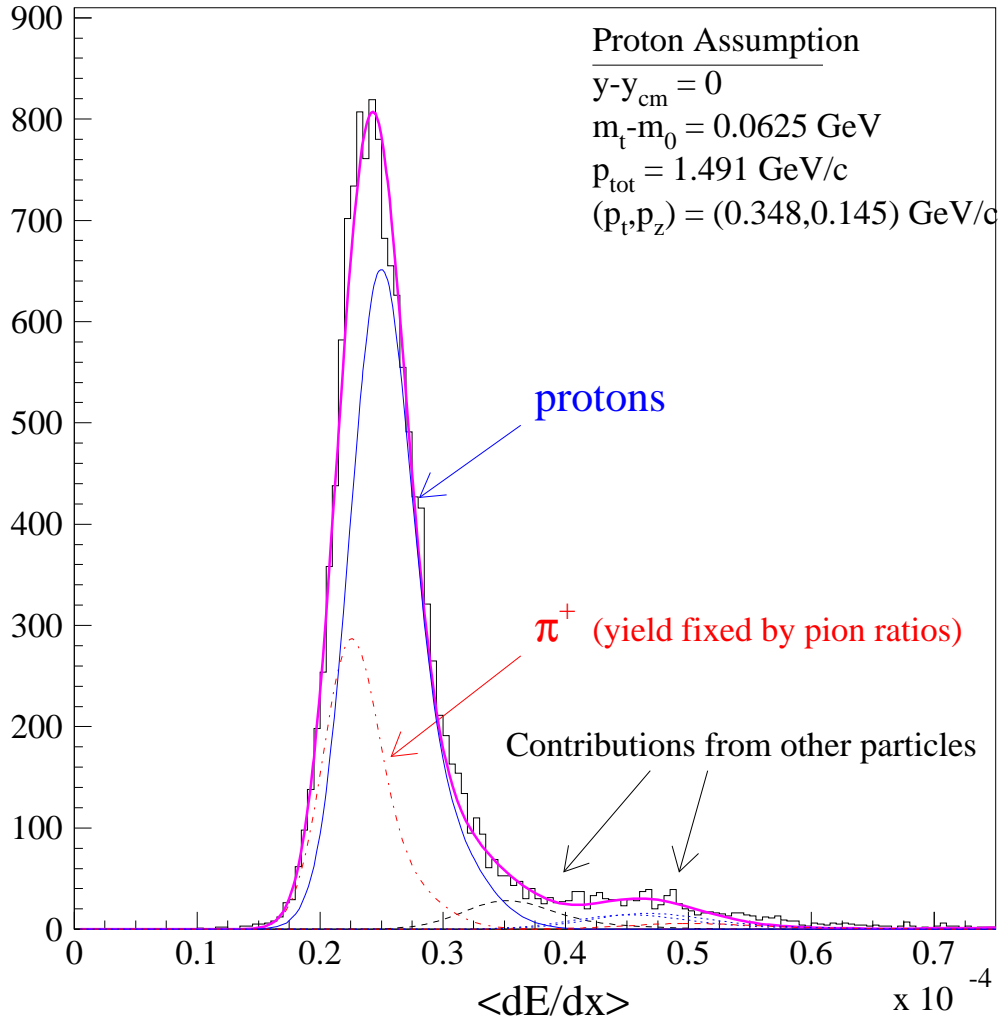
Figure 5.8: $\langle dE/dx \rangle$ distribution at 4 AGeV mid-rapidity in the proton mass assumption for Z=+1 particles. The π^+ yield is a fixed quantity predicted from the extrapolated pion ratios and the measured π^- yield for this (m_t-m_0,y) bin. Contamination due to other particle species, such as d,t and ^{3}He are free parameters in the fit.

predicted proton $\langle dE/dx \rangle$ is rising more quickly than the deuteron Bethe-Bloch prediction, whereas the triton prediction is just reaching its minimum, so that beyond a certain limit, the particle bands re-separate enough to recover the proton cross-section again. Unfortunately, the statistics are so reduced due to the exponential decline that the yield values exhibit appreciable statistical errors. Similar to the proton cut-off for the π^+, this effect manifests itself at lower and lower m_t-m_0 as we move forward in rapidity, due to the Lorentz boost from the fixed target lab frame. Nevertheless, the exponential trend in the proton spectra is still observable and can be used to characterize the overall proton yield as a function of m_t-m_0 and rapidity even in the very forward regions.

Chapter 6

Simulations and Corrections

6.1 Introduction

In order to understand how well the detector (both hardware and software) has captured the physical information coming from a collision, detailed studies of its acceptance, tracking efficiency and momentum resolution/skewing must be made. Each of these must be evaluated and the measured particle spectra corrected before interpretations of the physical significance of the measured data are made. To clarify the distinctions between the acceptance, efficiency and resolution/skewing, three questions may be asked and answered:

• Did a charged particle originating in the collision pass through the sensitive volume of the detector?

Geometric acceptance is constrained by the finite size and placement of the detector with respect to the collision vertex. Only those particles which actually pass through the detector's sensitive volume and leave a track with greater than 7 hits have a chance of being observed. This depends on the rapidity and p_t of the particle. It is essential to understand what fraction of the collision information is inaccessible to the detector in order to eliminate this bias. In addition to geometry, since time projection chambers rely on electromagnetic interactions to observe particles, they have zero acceptance for directly observing electrically neutral particles. [1]

---

[1] The exception of course occurs for those neutral particles which decay into charged daughters inside the detector volume. The daughters may then be tracked and reconstructed into the neutral parent.

• Did the detector assign a track to this particle?

Losses (or inefficiencies) arise from those particles which traverse the detector and leave a signal, but whose tracks of adequate length cannot be reconstructed at all due to the high density of hits. If tracks passing all quality cuts were assigned for every charged particle that passes through the detector, the efficiency would be 100%.

• Finally, if a track was assigned to the particle, how accurately was its momentum measured?

Due to uncertainties in the determination of the radius of curvature, disributions of reconstructed momenta are spread over a range of possible momenta, peaked (hopefully, but not always) at the true value. This momentum resolution varies as a function of momentum, since the radius of curvature can be more reliably determined for very curvy (low momentum) tracks than for straighter (high momentum) tracks.

Momentum skewing occurs when a track is found with a significantly different momentum than its true momentum. This is likely to occur when a track is assigned hits that don't belong to it or when some of its hits are lost or when the tracker creates a single track by switching between two independent track segments partway through the detector. Also, the uncertainty in determining the radius of curvature for high momentum tracks which are not significantly bent by the magnetic field introduces a significant momentum skewing. For the purposes of this analysis, the effects of acceptance, tracking efficiency and momentum resolution/skewing are combined into

a single measure of the detection efficiency, ϵ_{det}.

It is clear that ϵ_{det} is strongly dependent on the quality cuts applied to the data. For example, under what criteria is a track considered to be found and reliably measured? The more hits assigned to a track, the better determined is its momentum, because there are more samples from which to reconstruct this quantity. On the other hand, since the momentum is found from the radius of curvature of the track, for very stiff tracks with large radii of curvature, the detector's spatial resolution limits the accuracy of the momentum determination. Short, high-momentum tracks can suffer similarly. Stricter quality cuts assure that those particles found are better measured, but the data suffer from the loss of statistics. Attempts to apply corrections to these data can add additional and sometimes extreme statistical uncertainties. Looser quality cuts admit more tracks but many of these will suffer from the skewing of found momenta from the true momenta. This skewing effect is present in either case but is amplified in the second case.

Corrections must necessarily try to address all three issues: acceptance, losses and skewing. Reformulating the experimental conditions in mathematical terms, the TPC and Tracking (T) operate on the true physical spectrum of particles originating in a collision (p) to produce the observed spectrum (o).

$$T * p = o \tag{6.1}$$

If one could construct a TPC Response Matrix (TRM) which fully represents the

effects of the hardware (TPC) and software (Tracking), then finding the true physical spectrum would simply be a matter of inverting T and applying the result to the observed spectrum.

$$T^{-1} * o = p \qquad (6.2)$$

Fortunately, T can be found rather trivially from evaluating the results of embedding particles of known momenta into real data events. (This will be discussed in the next section.) Unfortunately, the inversion necessarily introduces large variations between adjacent elements of the inverted matrix. In fact adjacent elements in the columns or rows have opposite sign. Since the measured spectrum itself is subject to statistical uncertainties, the matrix multiplication of these two quantities amplifies the statistical fluctuations such that the "corrected" spectrum is unreasonably oscillatory. Therefore, an alternative approach was devised.

6.2 Monte Carlo Embedding

Corrections for the TPC response (hardware and software) can be obtained by simulating the detector's effects on the physics to be measured. The standard method of doing this is to embed particles of known mass and momentum into real data events at the pixel level. A spectrum of these "fake" particles is passed to GEANT, a software package which simulates the passage of these particles through the detector volume and acquisition electronics, taking into account all manner of interactions of these

particles with the detector material and noise sources.[GEAN94] The GEANT pixels are tagged as such and then embedded into real data events in small quantities (a maximum of four tracks per event) so as not to distort the real events too much. These events are processed through hit-finding and tracking software. The tag on GEANT hits assigned to tracks by the tracking software is retained for the purpose of later recovering the "found" embedded tracks.

The reason for embedding into real data events is to reliably reproduce the TPC and tracker's performance under battle conditions. Simply simulating and tracking the fake particles alone cannot account for the high-density conditions under which the software must try to resolve individual hits and tracks. Since tracking conditions vary according to bombarding energy and centrality in general, separate embedding runs must be undertaken for each beam energy and centrality class to be corrected. Because this experiment was conducted with fixed targets, the tracking conditions are asymmetric with respect to the center of momentum of the system. Therefore, for this analysis, embedding was performed using the 5% most central Au+Au collisions at the four beam energies: 2, 4, 6, 8 AGeV in narrow slices (0.1 units) of rapidity for two particle types: protons and π^-. In the interest of minimizing computing time, only every other rapidity bin (even-numbered bins) was separately embedded. The odd-numbered bin corrections were obtained from interpolating between neighboring bins. (96 correction vectors, covering most of phase space).

The embedded particles were randomized in azimuthal angle and over the given rapidity window. The magnitude of p_t for each particle was selected by randomly sampling from thermal m_t-m_0 spectra whose approximate parameters were obtained directly from the measured data. The embedded m_t-m_0 spectra were extended by a factor of two beyond the measured data to be corrected in order to reduce edge effects. To account for the two-track resolution of the tracker, tracks embedded in the same event were required to be well-separated compared to the measured momentum resolution. A single cut for all embedding was used: $\Delta p/p > 20\%$.

The thermal spectrum was chosen over the standard flat distribution in p_t for two important reasons. First, by statistically weighting the embedded data in a similar manner as the measured data, fewer events need be processed. Second, although a flat distribution is a reasonable input for evaluating pure losses, if the embedded spectrum were weighted equally in all bins of m_t-m_0, momentum skewing between bins would be more difficult to determine. The simulated data must experience the same kind of distortions as the real data in order to be able to accurately estimate the corrections. The goal is to be able to take simply the ratio of known embedded input to measured embedded output as a function of m_t-m_0 at each rapidity bin, including the effects of geometric acceptance, tracking losses and momentum skew, for the correction, ϵ_{det}.

Suppose a thermal spectrum t is embedded and the correction factor is taken to

be the ratio of the known input (t) over measured output (T * t), Equation 6.1.

$$D^{-1} = \frac{t}{(T * t)},$$
(6.3)

D thus being a diagonal matrix. If t $\sim$ p, then

$$(T * t) \sim o$$
(6.4)

and the operation of D^{-1} on the observed data should reproduce the true physical spectrum.

$$
\begin{aligned}
D^{-1} * o &= \frac{t}{(T * t)} * o \\
&= \frac{t}{o} * o \\
&= t \\
&= p.
\end{aligned}
$$
(6.5)

Figure 6.1 shows an example of D^{-1} (Equation 6.3) for pions and protons at mid-rapidity, 4 AGeV.

6.3   Pion and Proton Corrections

An example of the pion and proton detection efficiencies, ϵ_{det}, at mid-rapidity for 4 AGeV are shown in Figure 6.1. The complete detection efficiency plots are compiled in Appendix D. The data are corrected by dividing the measured spectra by the efficiency, ϵ_{det}. (Alternatively, one could define a correction factor, C$_{det}$ =
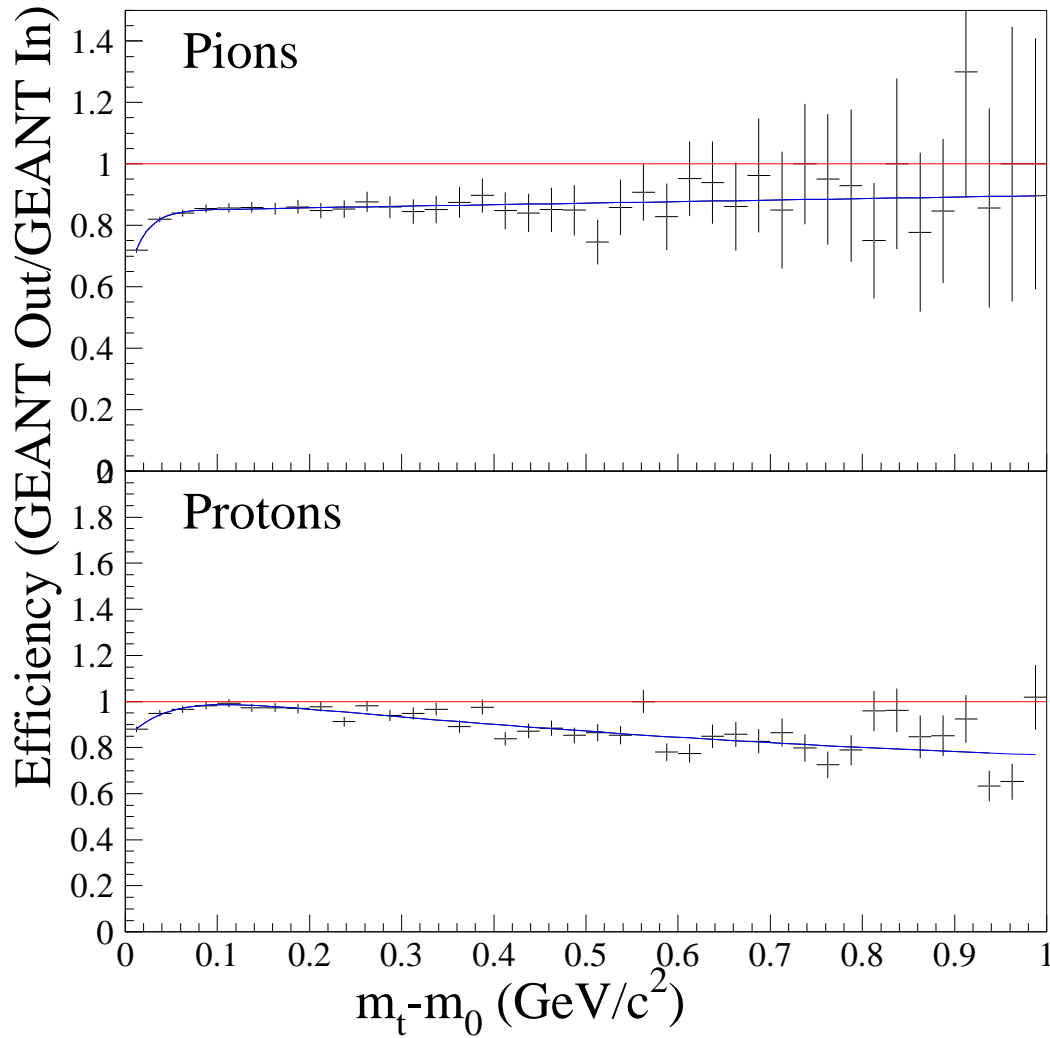
Figure 6.1: Example of E895 detection efficiency, D^{-1} from Equation 6.3, at 4 AGeV mid-rapidity for pions and protons.

ϵ_{det}^{-1}.) Due to the limited statistics available from the embedding, the fluctuations in the efficiencies increase at high m_t-m_0. Instead of applying these values directly to the data, a functional form is fit to the efficiency vector to obtain a smoothly varying function. The functional form chosen contains an overall offset parameter, α, an exponential term with an amplitude, A, and a decay parameter, τ, plus a linear term with slope, b.

$$\epsilon_{det} = \alpha + A e^{\frac{-m_t - m_0}{\tau}} + b(m_t - m_0) \tag{6.6}$$

This form is fit to all of the efficiency vectors obtained at each even-numbered rapidity slice for pions and protons at all four beam energies. Interpolating the odd-numbered bins between neighboring embedding bins, the assembled efficiencies as a function of m_t-m_0 and rapidity for pions and protons at each beam energy are shown in Figures 6.2 and 6.3. These efficiencies are applied bin-by-bin to the measured data to obtain the final observed spectra for pions and protons presented in Chapter 7.

The severe forward rapidity, low-m_t-m_0 proton inefficiency stems from the fact that this region has an extremely high track density, due to forward focusing from the Lorentz boost. The 8 AGeV data have the highest multiplicities and the largest boost, resulting in the trend of decreasing efficiency as a function of the beam energy from 2 AGeV to 8 AGeV. Backward rapidity inefficiencies are caused primarily by the geometric acceptance of the detector. A particle must traverse a length of the TPC such that it leaves a minimum of 7 hits in order to be counted as a track. High-

p_t particles with very backward rapidities have only a slim chance of meeting this requirement, causing the abrupt cut-offs observed in the efficiencies in this region.

Pion Efficiency
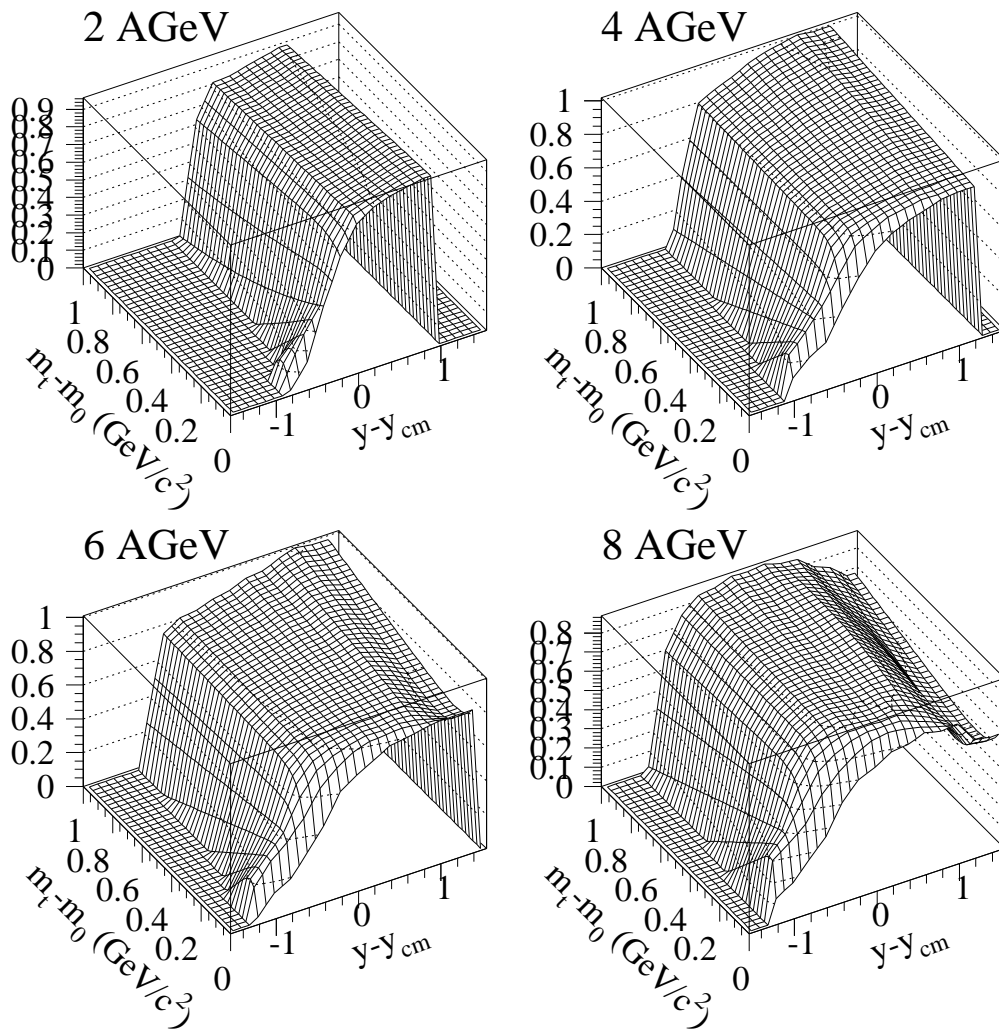
Figure 6.2: Surface plot showing E895 pion detection efficiency as a function of m_t-m_0 and rapidity at 2, 4, 6, and 8 AGeV

Proton Efficiency
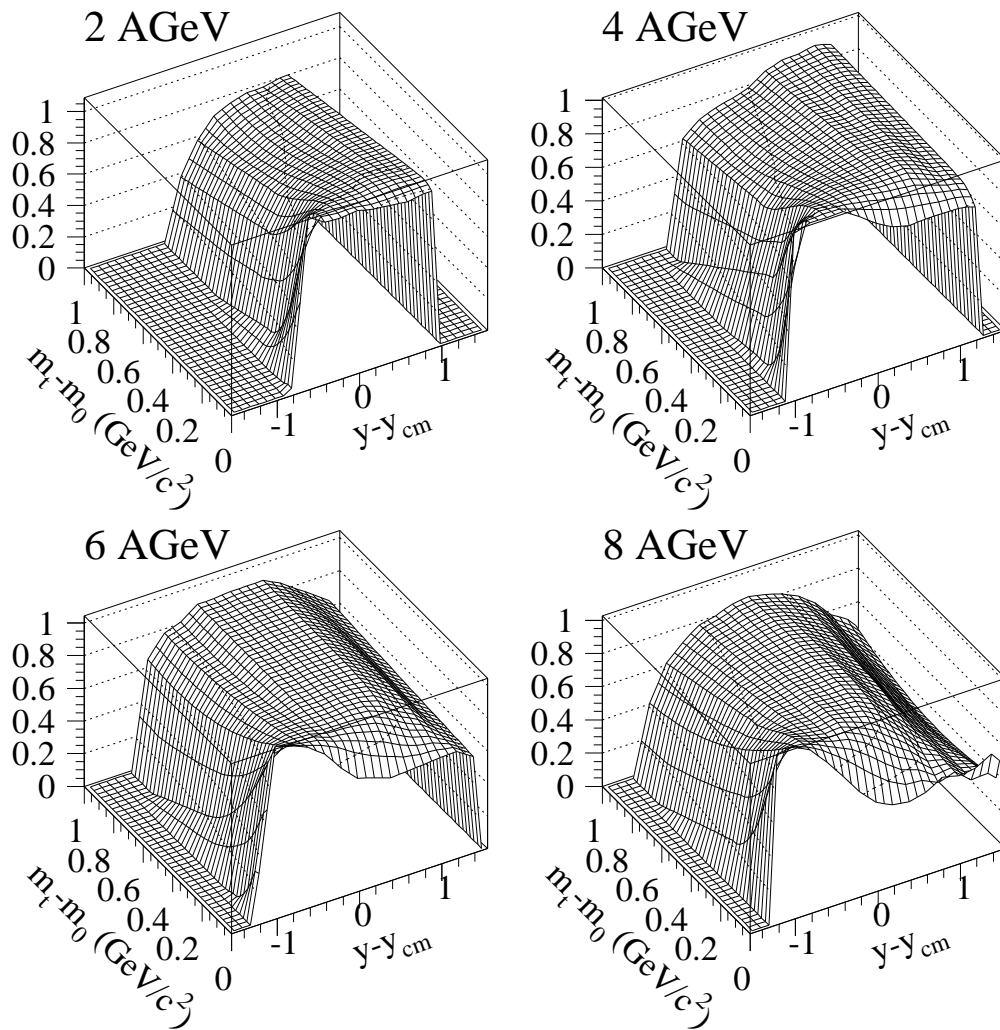
Figure 6.3: Surface plot showing E895 proton detection efficiency as a function of m_t-m_0 and rapidity at 2, 4, 6, and 8 AGeV

Chapter 7

Results

7.1   Transverse mass spectra

The Lorentz invariant yields per event of pions and protons obtained from the $\langle dE/dx \rangle$ fits described in Chapters 4 and 5, over all rapidity bins at all four beam energies, corrected for detector efficiency as described in Chapter 6, are plotted as a function of m_t-m_0 in Figures 7.1, 7.2 and 7.3. The mid-rapidity spectra are indicated by open squares in black at the center of each plot. Forward rapidity bins, scaled up by successive powers of ten, are plotted as green triangles, while the backward rapidity bins, scaled down by successive powers of ten, are displayed as inverted red triangles. The functional forms, shown superposed in blue, will be explained below.

The approximately exponential decay of the particle yields as a function of m_t-m_0 has been observed in heavy ion experiments over a wide range of conditions[Barr94], [Herr96], [Jone96], [Ahle00]. In 1974, for a hydrodynamic plus thermal model, Cooper and Frye developed a formalism from a hydrodynamic analysis to describe the relativistically invariant momentum spectrum of particles integrated over a freeze-out hypersurface, σ, [Coop74]

$$E\frac{d^3N}{dp^3} = \int_\sigma f(x,p)p^\mu d\sigma_\mu \tag{7.1}$$

where f(x,p) is the invariant distribution function (Maxwell-Boltzmann, Fermi-Dirac or Bose-Einstein, depending on the quantum statistics) describing the complete par-
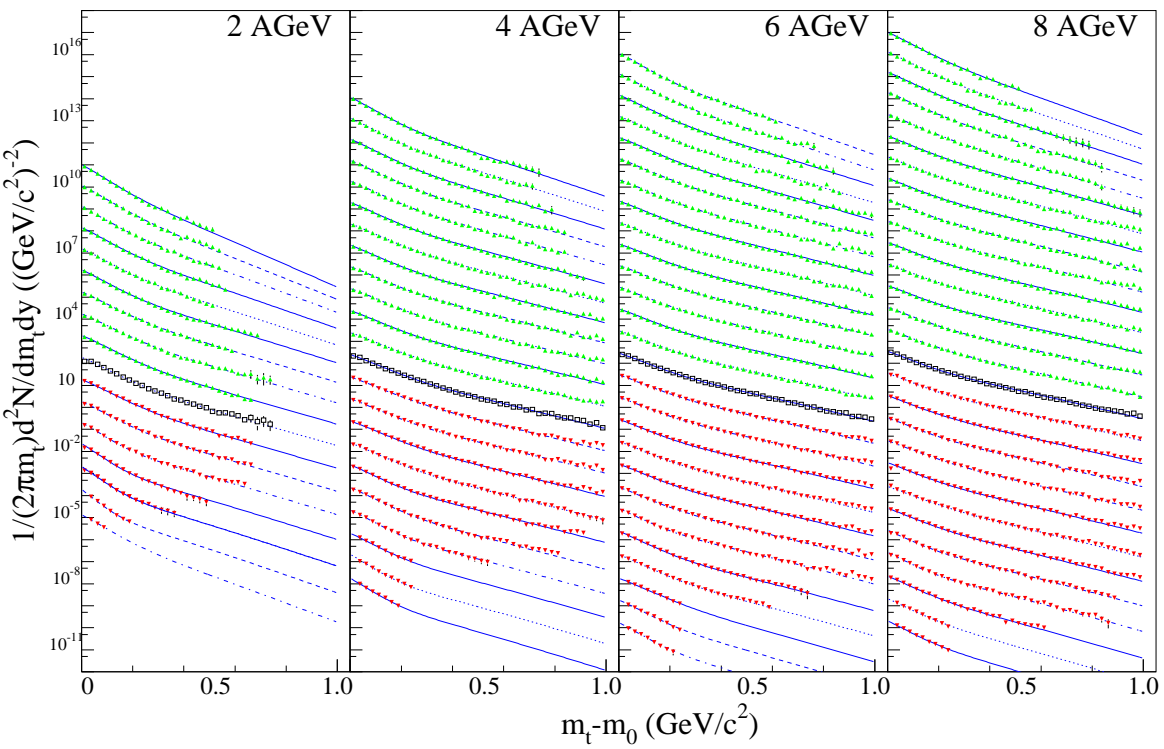
Figure 7.1: Invariant Yield of Negative Pions as a function of $m_t\text{-}m_0$ over all rapidity bins and beam energies. Mid-rapidity is shown unscaled as open black squares. Forward rapidities are shown scaled up by successive factors of ten as green triangles while backward rapidities are shown scaled down by successive factors of ten as inverted red triangles. The underlying fits represent a two-temperature thermal function fit.

Pi-Plus M$_t$ Spectra
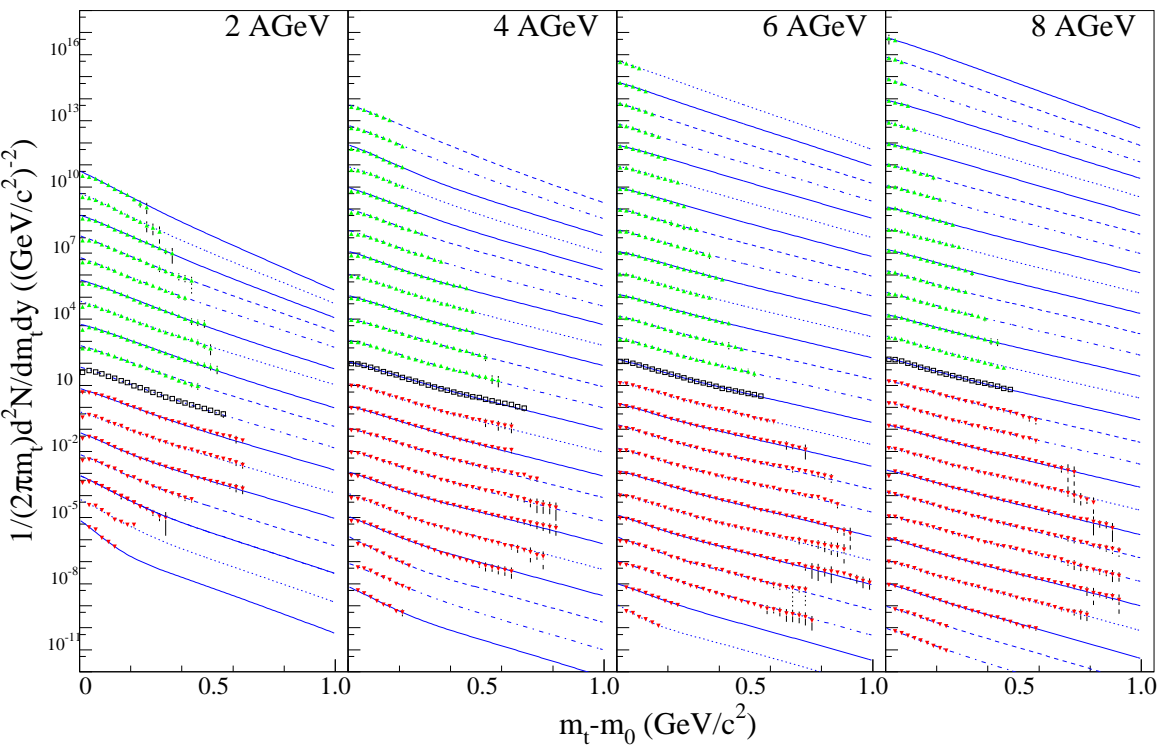
Figure 7.2: Invariant Yield of Positive Pions as a function of m$_t$-m$_0$ over all rapidity bins and beam energies. Mid-rapidity is shown unscaled as open black squares. Forward rapidities are shown scaled up by successive factors of ten as green triangles while backward rapidities are shown scaled down by successive factors of ten as inverted red triangles. The underlying fits represent a two-temperature thermal function fit.
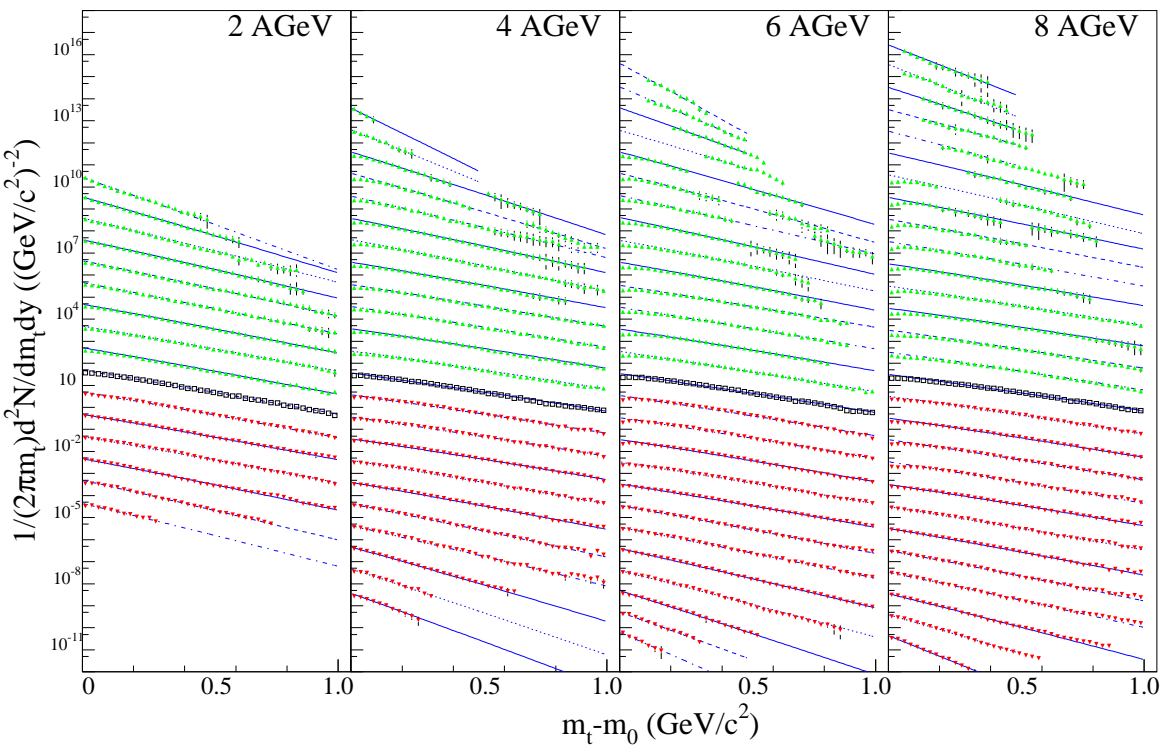
Figure 7.3: Invariant Yield of Protons as a function of $m_t - m_0$ over all rapidity bins and beam energies. Mid-rapidity is shown unscaled as open black squares. Forward rapidities are shown scaled up by successive factors of ten as green triangles while backward rapidities are shown scaled down by successive factors of ten as inverted red triangles. The underlying fits represent a single-temperature thermal function fit.

ticle phase-space density.

$$f(x,p) = \frac{g}{(2\pi)^3} \frac{1}{e^{[p^\nu u_\nu - \mu]/T} \pm 1},$$ (7.2)

where u is the fluid flow velocity and μ is the chemical potential. If the 3-velocity $\vec{u}$ is zero, the spectrum is purely thermal. Siemens and Rasmussen[Siem79] use a model of spherical symmetry with $\vec{u}$ radially outward and the $\pm$ 1 is omitted (Maxwell-Boltzmann assumption). At large m_t, the density in phase space is small enough that omitting the $\pm$ 1 in Equation 7.1 is reasonable. Transforming to the measured co-ordinates, (m_t-m_0,y), and integrating over azimuthal angle, the distribution (7.1,7.2) can be approximated for large p_t as

$$\frac{1}{2\pi m_t} \frac{d^2N}{dm_t dy} = A(y) m_t e^{-(m_t - m_0)/T_{eff}(y)}$$ (7.3)

where the amplitude A and temperature T_{eff} are parameters which can be extracted from fits to the data at each rapidity slice. Note that $T_{eff} \neq T$ of (7.2) unless $\vec{u}=0$. Integration of this distribution over m_t produces the total number of particles per unit of rapidity in the given rapidity slice. [Schn93]

$$\frac{dN}{dy}(y) = 2\pi A(y)(m_0^2 T_{eff}(y) + 2m_0 T_{eff}^2(y) + 2T_{eff}^3(y))$$ (7.4)

For convenience, Equation 7.3, can be re-expressed in terms of the integrated yield:

$$\frac{1}{2\pi m_t} \frac{d^2N}{dm_t dy} = \frac{dN/dy}{2\pi T_{eff}\left(m_0^2 + 2m_0 T_{eff} + 2T_{eff}^2\right)} m_t e^{-(m_t - m_0)/T_{eff}}$$ (7.5)

and the fit parameters extracted from the data become dN/dy(y) and the effective temperature, $T_{eff}(y)$, both functions of the rapidity.

Approximation 7.3 does not account for additional dynamical effects which can distort the spectra further. These are contributions due to resonance decays [Soll90], [Hofm95], [Wein98], and the Coulomb interaction [Gyul81], [Barz98], [Ayal99] described in Chapter 5. With these effects in mind, the temperature parameters extracted from the data for this analysis should be interpreted only as "inverse slope parameters" which describe approximately the observed data. For a detailed description of the deconvolution of radial flow and thermal effects using the Siemens and Rasmussen model in the mid-rapidity negative pion, proton and helion spectra observed in E895, please refer to the PhD dissertation of M. Heffner [Heff00].

7.2   Pion Spectral Shapes

The effective thermal model alone cannot describe the full range of the m_t-m_0 spectra for pions, due to an enhancement of the number of pions at low p_t from the feed-down of late-stage resonance decays [Soll90], [Hofm95], [Wein98]. Pion production near 2 AGeV is dominated by the production of the lowest mass nucleonic resonance, the $\Delta(1232)$.[Stoc86] This resonance is a short-lived isospin resonance state of the nucleon which decays into a pion and a nucleon. Elastic and inelastic collisions between beam and target nucleons during the earliest compression stage of the colli-

sions produce new particles and a lot of these excitations which then decay during the cooling expansion phase of the collision. In addition, π-N interactions in the fireball are very important. $\sigma(\pi N \rightarrow \Delta)$ is very large, particularly $\pi^+ p \rightarrow \Delta^{++}$ and $\pi^- n \rightarrow \Delta^-$. The final state distributions of the pions depend on the point of decay of their parent. Since the Δs are very short-lived ($\Gamma \simeq 100$ MeV), they decay quickly. The daughters emerging from these decays may have sufficient time to thermalize with their neighbors, and/or develop collective fluid motion, increasing their average energy. However, decays that occur near the surface of the expanding fireball or at later stages of the expansion, close to freeze-out, will not have this chance. Their final-state momenta are fixed by the decay kinematics.

Due to conservation of momentum, in the rest frame of the Δ, the pion and nucleon daughters each receive 227 MeV/c. Since the azimuthal angle of emission of this back-to-back pair is randomly distributed, for a large number of decays, on average, the pion and nucleon each have zero momentum ($\langle p \rangle \approx 0$). The average energy of the pion or the nucleon, $\langle E \rangle = \langle \sqrt{p^2 + m^2} \rangle$ ($\neq \sqrt{\langle p \rangle^2 + m^2}$), depends on the relationship between the daughter mass and the daughter momentum, p = 227 MeV/c. Since the nucleon mass is approximately four times larger than 227 MeV/c, compared to a factor of ≈ 0.6 for the pion, the average nucleon energy is over twice the pion energy in the Δ frame. The Lorentz boost from the Δ frame to the center of momentum of the collision is the same for both daughter particles, so the ratio
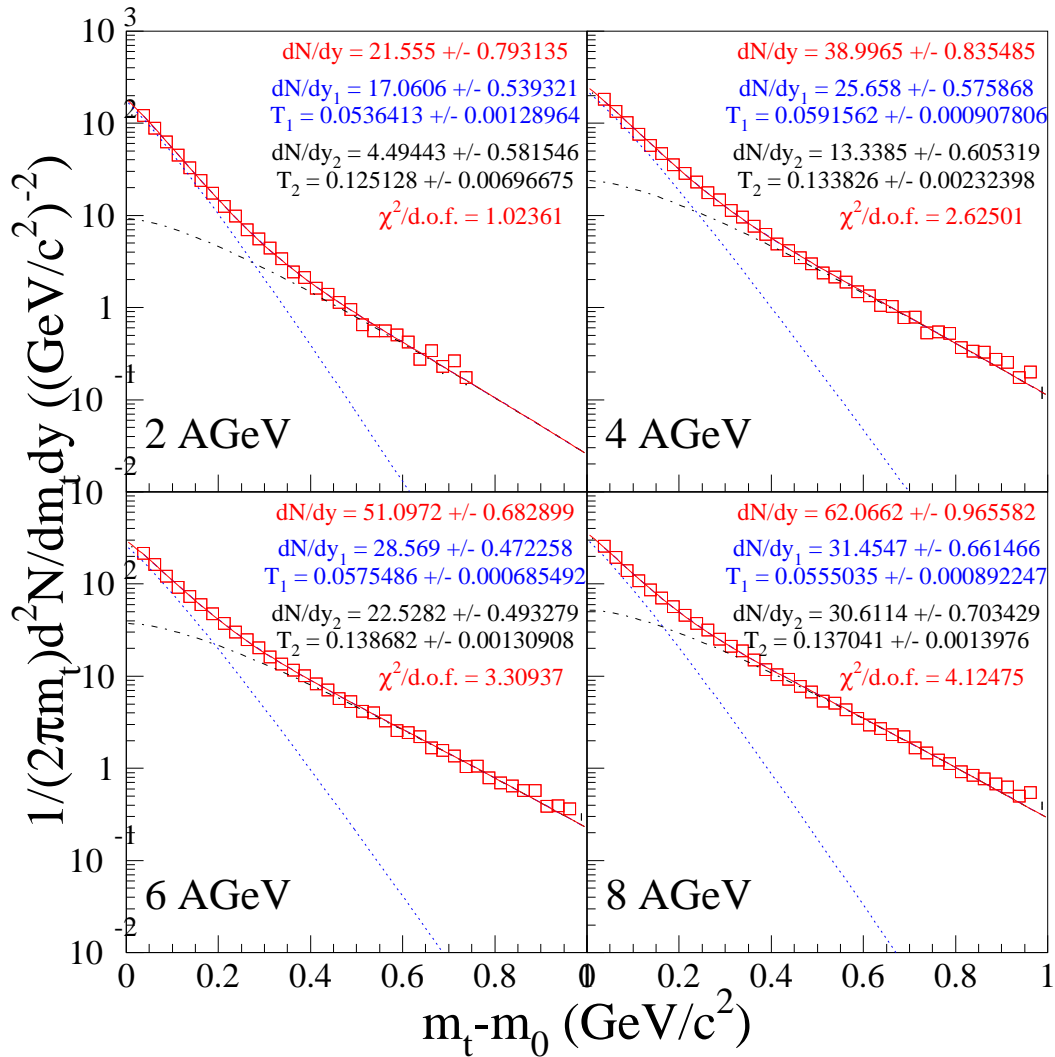
π^- at Mid-rapidity

Figure 7.4: Negative pion transverse mass spectra at mid-rapidity for 2, 4, 6, and 8 AGeV. Two-temperature thermal fits are shown superposed on the data along with the contributions to the total from the two separate temperature functions.

of their average energies in the Δ frame is the same as in the frame of the center of momentum of the nuclear collision:

$$\langle p \rangle^{CM} = \gamma(\langle p \rangle + \beta\langle E \rangle) \simeq \gamma\beta\langle E \rangle. \tag{7.6}$$

An approximately thermal distribution of Δs in the center of momentum frame of the collision means that there are significantly more low m_t-m_0 than high m_t-m_0 Δs. Combined with the decay kinematics discussed above, this implies that on average, the Δ decays soften the pion spectra more than the nucleon spectra. That is, the effective temperature of the late-stage resonance feed-down pions is lower than the thermal rescattered pion temperature.

This qualitative treatment has been made quantitative along with the addition of contributions from other resonance decays by numerous authors [Stoc86], [Soll90], [Schn93], [Hofm95], [Wein98]. For the purpose of this analysis, the characterization of the observed enhancement is the main goal. Therefore, a two-temperature model of the pion spectra has been applied to reproduce the shapes of the spectra over all m_t-m_0. The "double thermal" fit has two slope parameters and two yield parameters which are extracted from the data. The steeper shape of the spectra at low m_t-m_0 is characterized by an effective Δ-dominated temperature, while the higher temperature parameter characterizing the flatter, high m_t-m_0 region is attributed to thermally rescattered pions. Collective flow effects are assumed to contribute to all regions of the spectra. An example of this four parameter fit is shown in Figure 7.4. The

mid-rapidity π^- transverse mass spectra are plotted at each beam energy with the two-temperature model fits and the separate contributions from the Δ and thermal rescattering regions also overlaid. This parameterization of the observed pion data allows us to characterize the pion spectral shapes over all measured m_t-m_0 and to analytically extrapolate the distributions to arbitrarily large m_t-m_0. By integrating the distributions over m_t-m_0 and rapidity we can estimate the complete 4π yields of pions emerging from our collisions.

7.2.1 Negative Pions

The top four panels of Figures 7.5, 7.6, 7.7, and 7.8 show the parameters obtained from the two-temperature fits as a function of rapidity for negative pions when all four parameters are allowed to be freely fit. The scatter in the individual temperature and dN/dy parameters is largely the result of some covariance between them. The overall rapidity density plotted in the first panel indicates that this scatter does not significantly affect the overall yield of pions extracted in each rapidity bin. The number of pions and the effective temperature parameters are observed to peak at mid-rapidity (y-y_{CM} = 0), decreasing away from mid-rapidity. This suggests that the energy available for particle production and the average transverse energy are highest at mid-rapidity. Gaussian parameterizations of the rapidity densities and the temperature parameters are indicated on the figures. In a thermalized system,

there is a single average total energy which is the same for all particles ($\langle p_x \rangle^2 = \langle p_y \rangle^2 = \langle p_z \rangle^2$). From the relationship between energy and rapidity, E=$m_t$cosh(y), the higher the rapidity, the lower the average m_t for thermalized particles. Therefore, one expects the temperature parameters to decrease away from mid-rapidity, which is the observed trend. The broader temperature parameter widths as compared to the rapidity density widths probably reflect the fact that there is an energy threshold associated with particle production. A large transfer of energy between interacting particles is required for new particle production compared to a thermal exchange. The pair-production interaction probability is higher at mid-rapidity than at the tails of the rapidity distributions.

In a second pass on the data, the thermal rescattering temperature parameter is held fixed to the Gaussian fit values. This constrains the covariance among the other three parameters such that they may be more reliably extracted. In the backward regions where the data are scarce at high m_t-m_0, the thermal rescattering yield is also fixed to the corresponding forward rapidity value. Yields that were fixed in this way are indicated by an "x" overlaid on the plotted points. The results of these fits are shown in the bottom four panels of Figures 7.5, 7.6, 7.7 and 7.8. The differences in the 4π yields extracted from these two methods define the degree of error in measurement. The fit functions plotted on the π^- data in Figure 7.1 use the parameters from this second pass fit.

Figure 7.5: Fit parameters from 2 AGeV negative pion transverse mass spectra fits with a two-temperature model. The top four panels are from fits allowing all parameters to float. The bottom four panels are from fits in which the thermal rescattering temperature parameters were held fixed to the Gaussian parameterized values. A Gaussian parameterization was chosen because it works well at the higher beam energies. The sum of the red and blue points in the fourth and eighth panels are the total yields shown in the first and fifth panels, respectively. Data points indicated with an "x" represent rapidity-reflected fixed yields. The extracted parameters indicated on the figures are only significant to the first three digits.

Figure 7.6: Fit parameters from 4 AGeV negative pion transverse mass spectra fits with a two-temperature model. The top four panels are from fits allowing all parameters to float. The bottom four panels are from fits in which the thermal rescattering temperature parameters were held fixed to the Gaussian parameterized values. The sum of the red and blue points in the fourth and eighth panels are the total yields shown in the first and fifth panels, respectively. Data points indicated with an "x" represent rapidity-reflected fixed yields. The extracted parameters indicated on the figures are only significant to the first three digits.

Figure 7.7: Fit parameters from 6 AGeV negative pion transverse mass spectra fits with a two-temperature model. The top four panels are from fits allowing all parameters to float. The bottom four panels are from fits in which the thermal rescattering temperature parameters were held fixed to the Gaussian parameterized values. The sum of the red and blue points in the fourth and eighth panels are the total yields shown in the first and fifth panels, respectively. Data points indicated with an "x" represent rapidity-reflected fixed yields. The extracted parameters indicated on the figures are only significant to the first three digits.
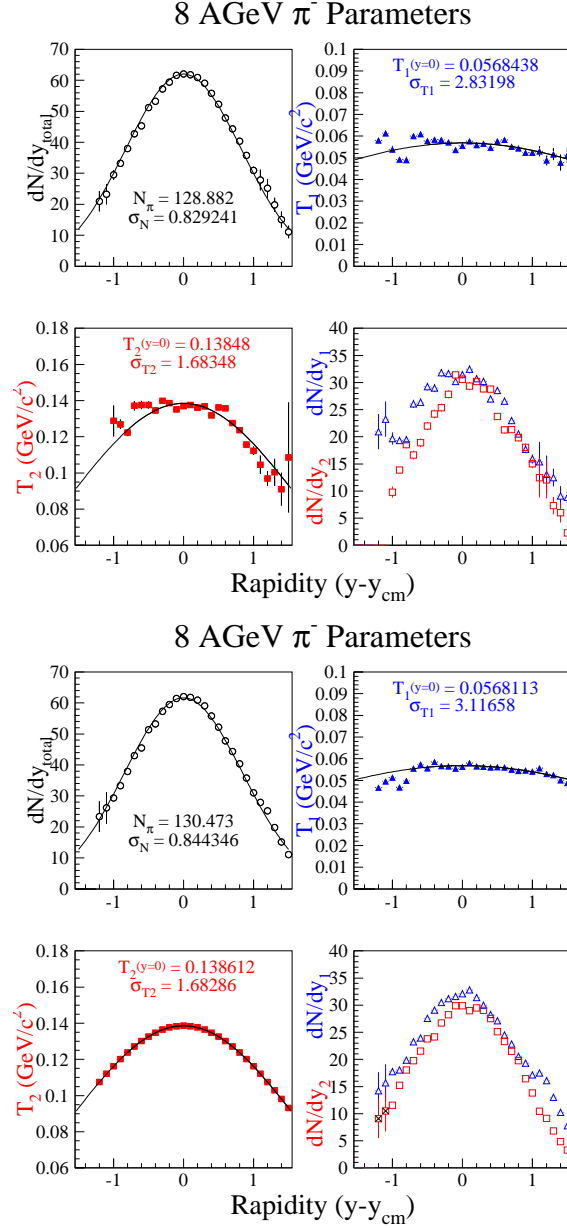
Figure 7.8: Fit parameters from 8 AGeV negative pion transverse mass spectra fits with a two-temperature model. The top four panels are from fits allowing all parameters to float. The bottom four panels are from fits in which the thermal rescattering temperature parameters were held fixed to the Gaussian parameterized values. The sum of the red and blue points in the fourth and eighth panels are the total yields shown in the first and fifth panels, respectively. Data points indicated with an "x" represent rapidity-reflected fixed yields. The extracted parameters indicated on the figures are only significant to the first three digits.

7.2.2 Positive Pions

The positive pion spectra can be similarly fit with a two-temperature model for the dN/dy and temperature parameters describing their shapes. However, as should be apparent from Figure 7.2, the limited range of m_t-m_0 that can be measured for the π^+ means that there are much larger uncertainties in the extraction of the thermal rescattering yield and temperature parameter. In order to extract reliable 4π yields, the Gaussian-parameterized thermal rescattering temperature parameters extracted from the negative pions were used as fixed values in the positive pion fits, while the Δ-dominated temperature and yield were allowed to be freely fit. This prescription is justified if the pions at high m_t-m_0 are truly dominated by thermal rescattering and the Coulomb effect is only important at low m_t-m_0. Thermal rescattering, on average, is assumed to be charge independent. The validity of this approximation is affected by the neutron excess and therefore the difference between π^+N and π^-N interactions. However, $\pi\pi$ strong interactions, which should be charge sign independent, also play an important role in the thermalization process, especially at higher beam energies, where the number of pions is significantly larger than the number of nucleons. The fact that the pions are light compared to the nucleons means that the average number of $\pi\pi$ collisions needed to thermalize them is smaller than the average number of πN collisions needed for thermalization. Despite the caveats, experimentally, the high m_t-m_0 negative pion temperature parameters reasonably reproduce the observed high m_t-

m_0 positive pion slopes in Figure 7.2. In certain cases, the thermal rescattered yield parameters were also fixed, using estimates based on information from the rapidity bins where the values can be extracted from the data. The results are shown in Figures 7.9, 7.10, 7.11 and 7.12. Where fixed values for the thermal rescattered yields were used, the data points are marked with an "x". The larger uncertainties in the yields from the forward rapidity bins reflect the fact that there is more extrapolation than measured data in those regions.

The Δ-dominated temperature parameters for the π^+ are higher than those obtained from the negative pions. Recall from Chapter 5, a Coulomb interaction of the pions with the nuclear fireball is expected to give an extra energy kick to the π^+ while the π^- experience a drag. This effect produces an additional enhancement at the lowest m_t-m_0 of the π^-, while correspondingly depleting the lowest m_t-m_0 region of the π^+. The observed temperature parameters bear this out. The Δ-dominated π^- "temperature" is colder than the π^+ temperature by about 25% at 2 AGeV, 15% at 4 AGeV, 17% at 6 AGeV and 19% at 8 AGeV.
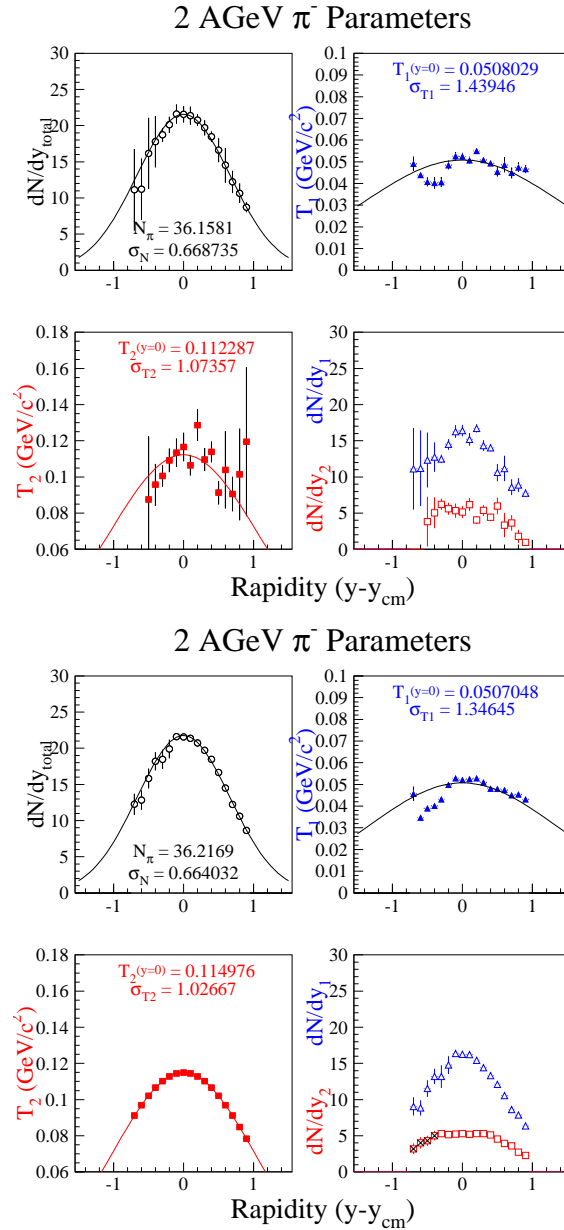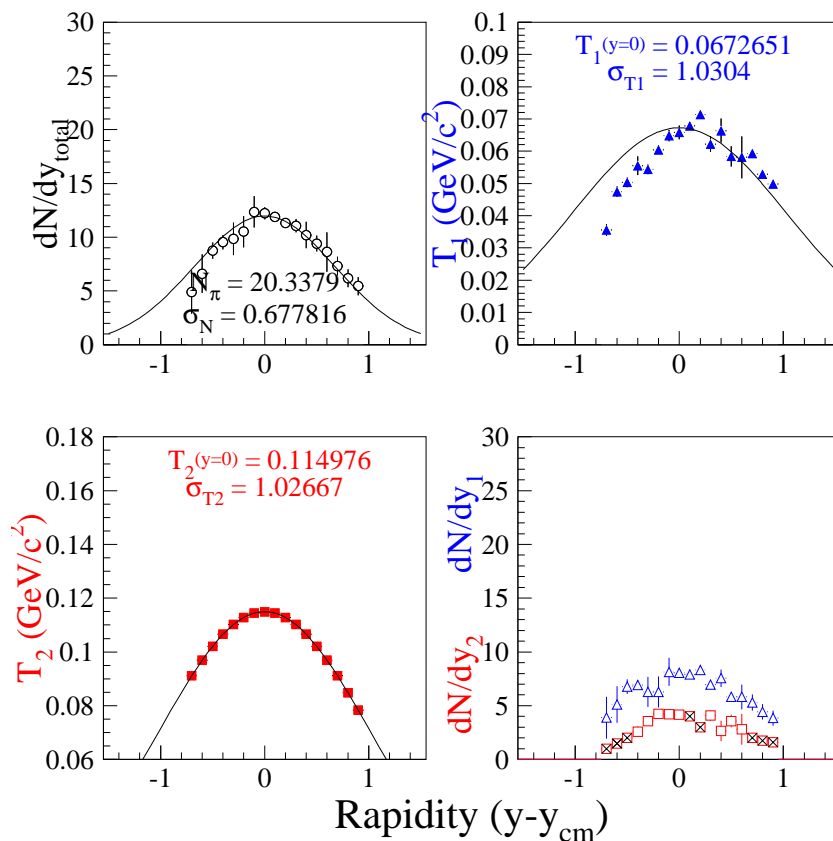
Figure 7.9: Fit parameters from 2 AGeV positive pion transverse mass spectra fits with a two-temperature model. The thermal rescattering temperature parameters were held fixed to the Gaussian parameterized values obtained from the negative pions. The sum of the red and blue points in the fourth panel is the total yield shown in the first panel. Data points indicated with an "x" represent fixed yields. The extracted parameters indicated on the figures are only significant to the first three digits.
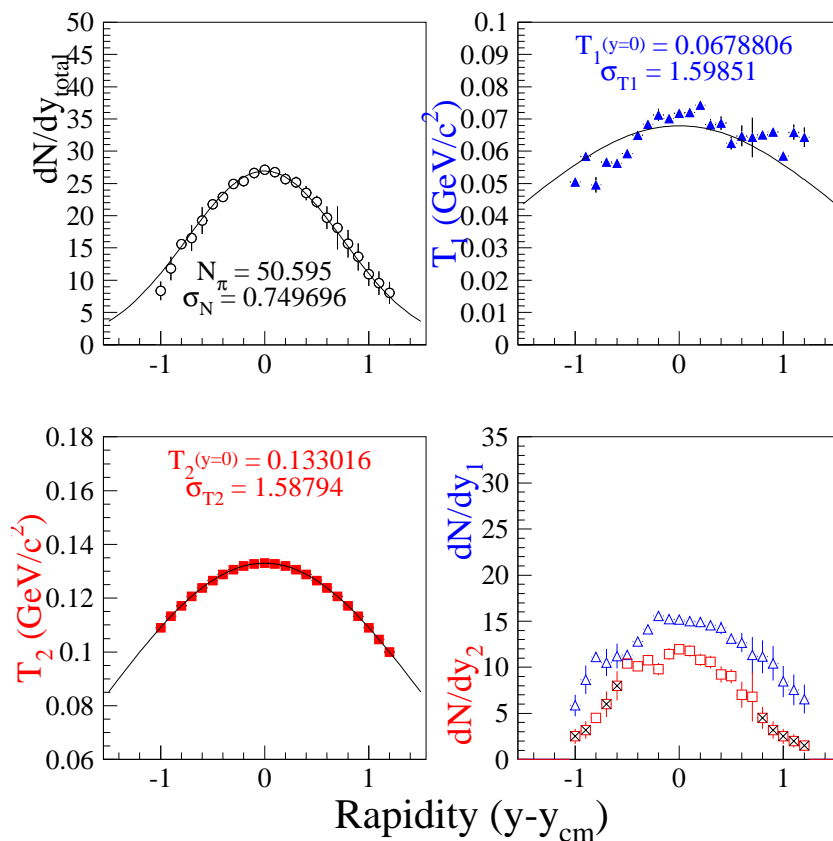
Figure 7.10: Fit parameters from 4 AGeV positive pion transverse mass spectra fits with a two-temperature model. The thermal rescattering temperature parameters were held fixed to the Gaussian parameterized values obtained from the negative pions. The sum of the red and blue points in the fourth panel is the total yield shown in the first panel. Data points indicated with an "x" represent fixed yields. The extracted parameters indicated on the figures are only significant to the first three digits.
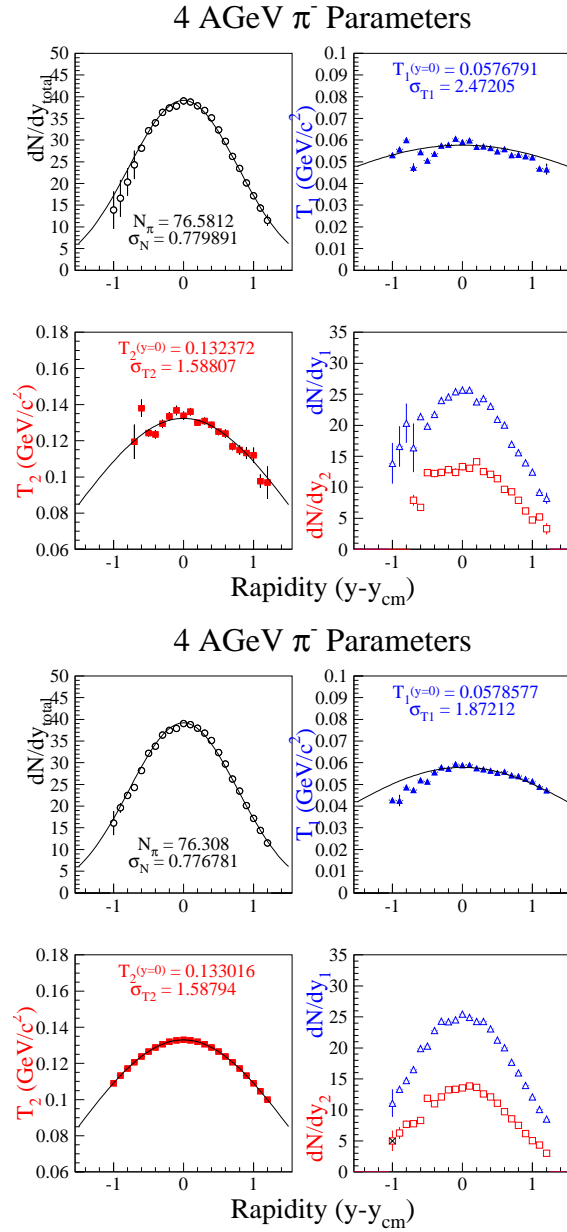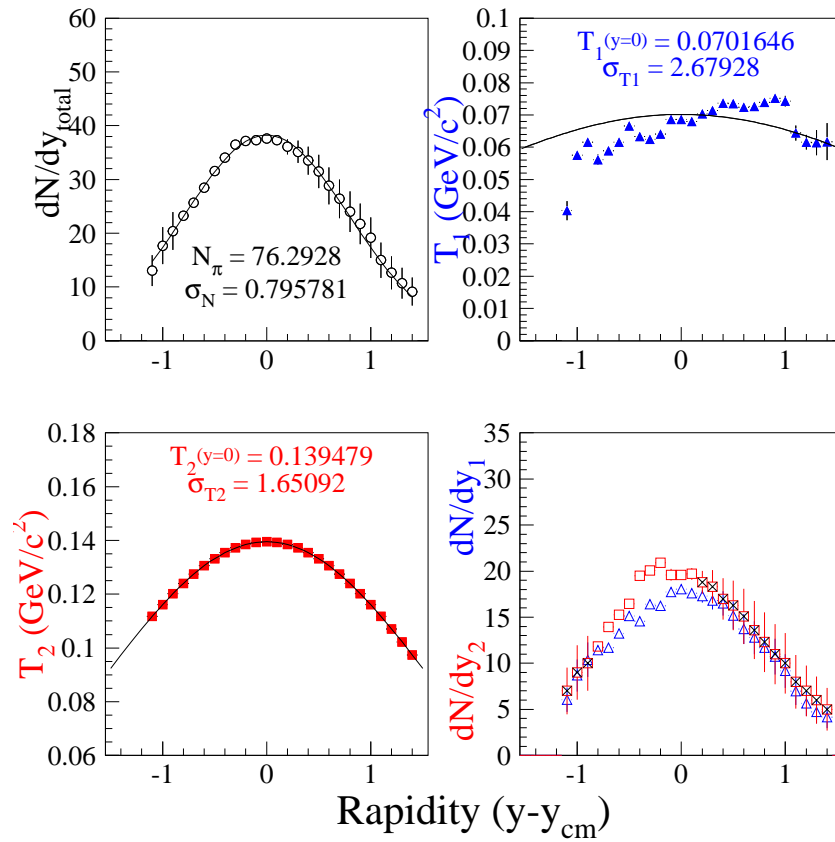
Figure 7.11: Fit parameters from 6 AGeV positive pion transverse mass spectra fits with a two-temperature model. The thermal rescattering temperature parameters were held fixed to the Gaussian parameterized values obtained from the negative pions. The sum of the red and blue points in the fourth panel is the total yield shown in the first panel. Data points indicated with an "x" represent fixed yields. The extracted parameters indicated on the figures are only significant to the first three digits.
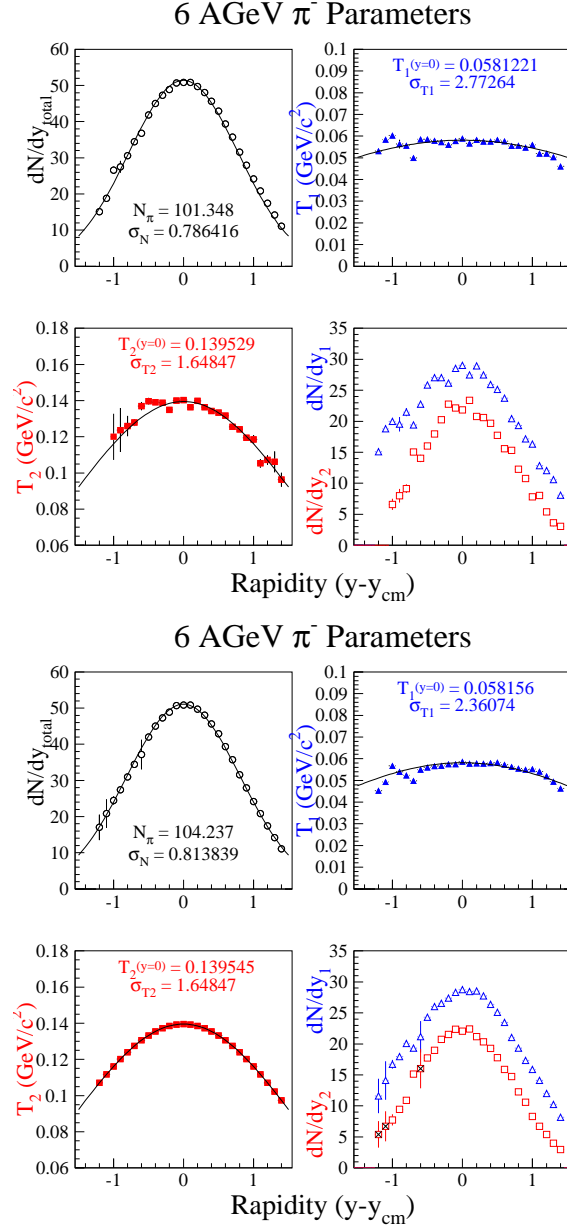
8 AGeV π^+ Parameters

$N_\pi = 96.1908$
$\sigma_N = 0.832376$

$T_1^{(y=0)} = 0.0695717$
$\sigma_{T1} = 2.41565$

$T_2^{(y=0)} = 0.138612$
$\sigma_{T2} = 1.68286$
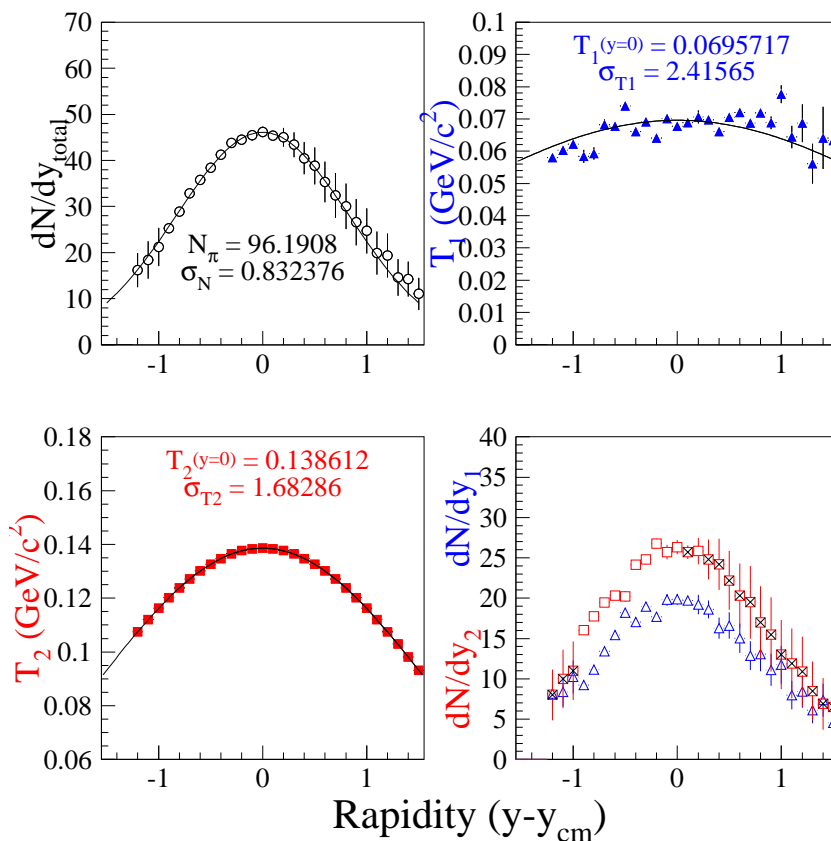
Figure 7.12: Fit parameters from 8 AGeV positive pion transverse mass spectra fits with a two-temperature model. The thermal rescattering temperature parameters were held fixed to the Gaussian parameterized values obtained from the negative pions. The sum of the red and blue points in the fourth panel is the total yield shown in the first panel. Data points indicated with an "x" represent fixed yields. The extracted parameters indicated on the figures are only significant to the first three digits.

7.3 Proton Spectral Shapes

Although the proton spectra are also affected by feed-down from resonance decays, the effect is not easily discernible from the data. However, the dip in the spectra at low m_t-m_0 is a significant feature. The shapes of the proton spectra over all m_t-m_0 are better characterized by the superposition of a relativistic blast wave and an underlying thermal distribution, a so-called "boosted thermal" model. [Siem79], [Dobl99], [Lisa95], [Heff00] The boost effectively moves the peak of the distribution away from the zero-momentum peak of the Maxwell-Boltzmann distribution to a momentum related to the blast wave velocity. For a given fluid velocity, the different mass particles are shifted by different amounts. The proton shift is more evident than the pion shift due to the factor of ~ 7 difference in their masses ($E_{kin} \propto m$). For m_t-m_0 above about two hundred MeV/c^2, the proton spectra can be reasonably well-described by a thermal function of their transverse momentum distributions. For this analysis, therefore, a single thermal function is applied over the limited range in m_t-m_0, from above the peak to 1 GeV/c^2, to extract the effective temperature parameter. The yields are obtained by analytically extrapolating this fit from zero to arbitrarily large m_t-m_0. Examples of this type of fit at mid-rapidity for each beam energy are shown in Figure 7.13. The yields and temperature parameters obtained as a function of rapidity at each beam energy are shown in Figure 7.14. A Gaussian parameterization of the rapidity density distribution as a function of rapidity is used

to extract the 4π yield of protons.

Protons at Midrapidity
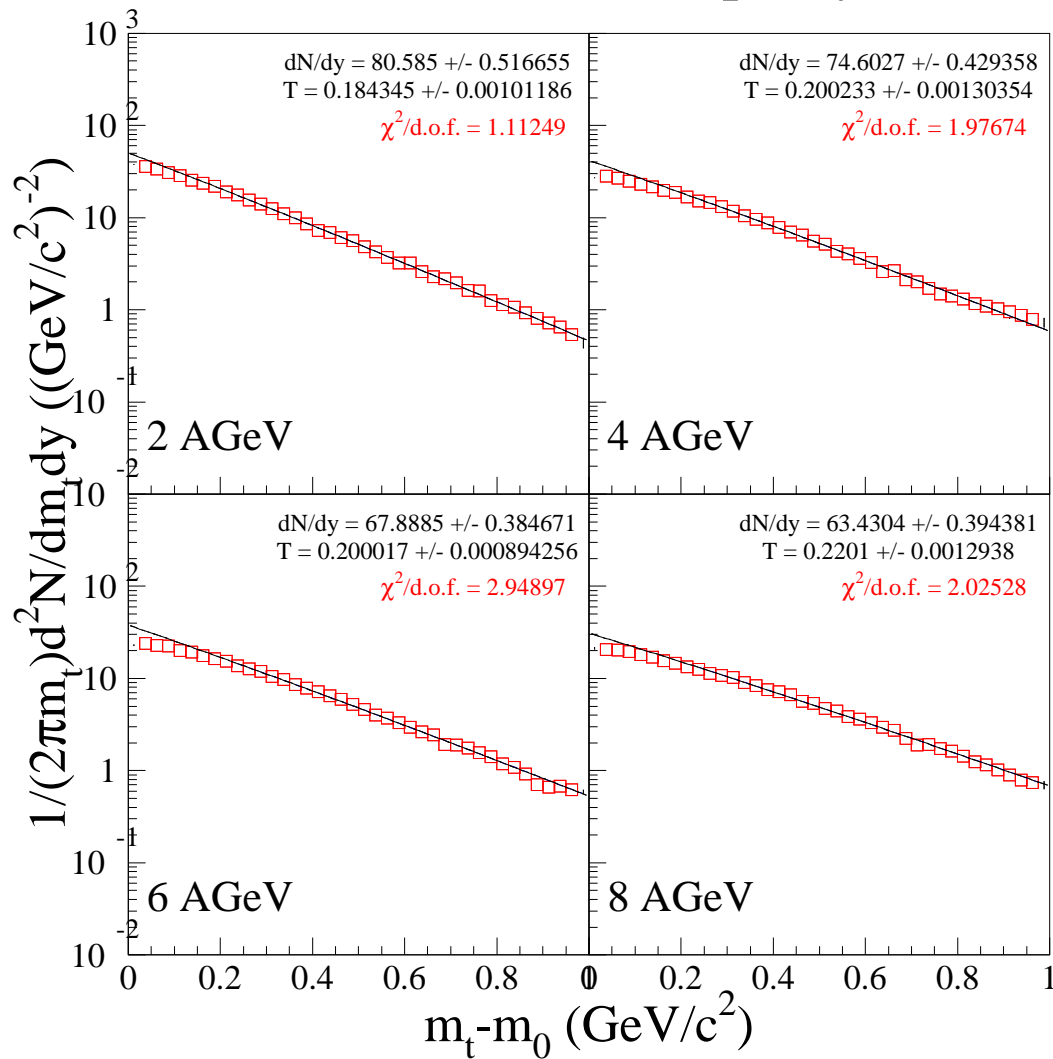
Figure 7.13: Proton transverse mass spectra at mid-rapidity for 2, 4, 6, and 8 AGeV. Single slope thermal function fits are shown superposed on the data.

Proton Parameters
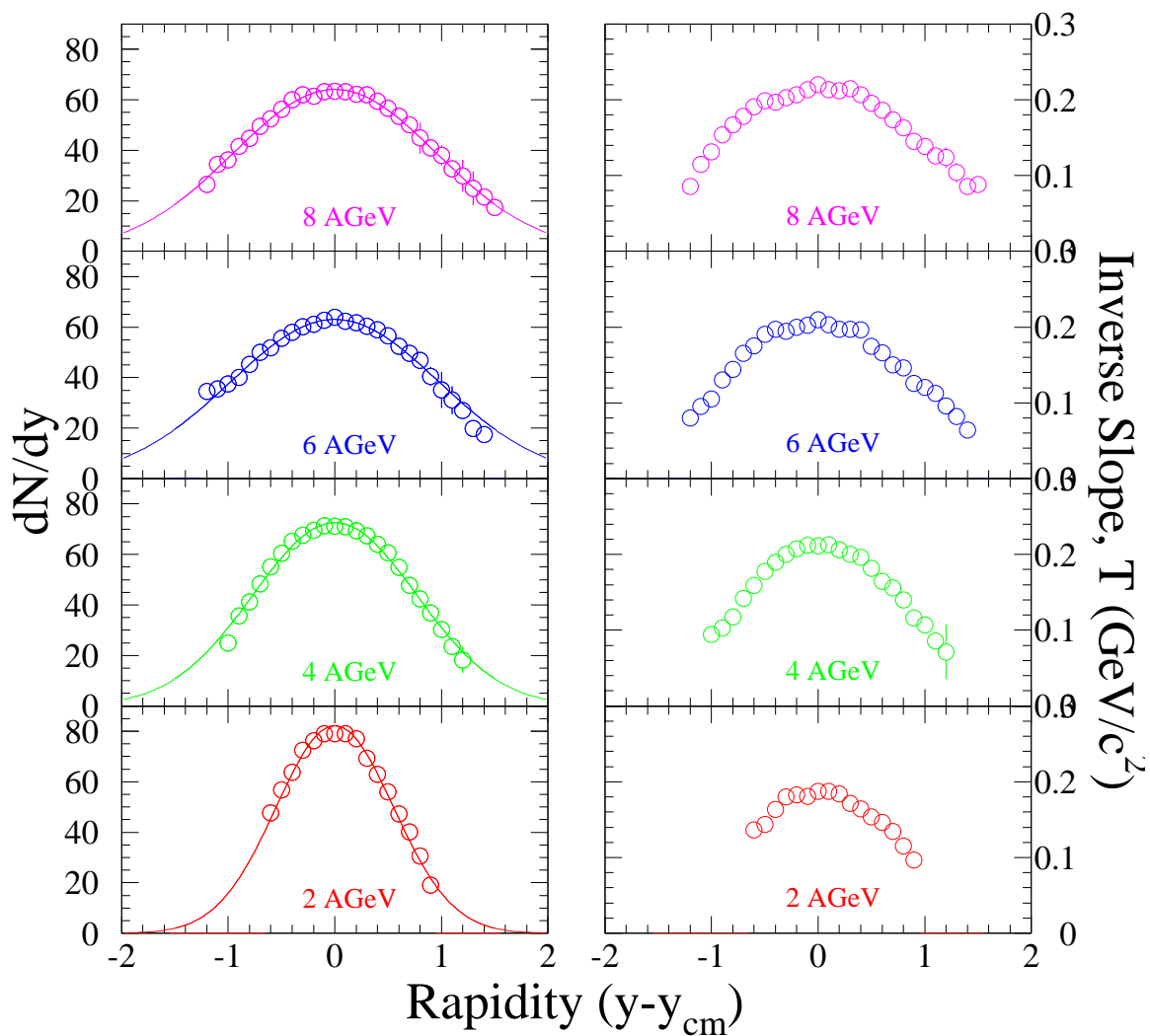
Figure 7.14: Yield and Temperature parameters from proton transverse mass spectra fits with a single slope thermal function.

7.4   Rapidity Densities and 4π Yields

The two-slope thermal function, represented by the sum of two single-slope thermal functions, was integrated over m_t-m_0 to generate the dN/dy distributions of pions shown in Figures 7.15 and 7.16. The proton dN/dy distributions shown in Figure 7.17 were obtained by integrating their single slope thermal functions over all m_t-m_0. The analytic extrapolations to arbitrarily large m_t-m_0 contribute only a small amount to the total yield of π^- and protons at a given rapidity, due to the exponential decay of the number of particles as a function of m_t-m_0. The large error bars on the π^+ yields at forward rapidities reflect the fact that a more significant fraction of the yield comes from extrapolation rather than measurement.

The dN/dy distributions are well-described by a Gaussian parameterization, which is used to obtain the total 4π yields by integrating the fitted distributions from -∞ to +∞.

$$N = \int_{-\infty}^{+\infty} \frac{dN}{dy} dy = \sqrt{2\pi}\sigma A \qquad (7.7)$$

where A is the value of dN/dy at y-y_{CM} = 0 and σ is the width. The fit parameters and their uncertainties are listed in Tables 7.1, 7.2, and 7.3. Both the widths and the overall yields of pions increase as a function of beam energy. However, there is a more significant jump in the observed pion yields between 2 AGeV and 4 AGeV than between 4 and 6 AGeV or 6 and 8 AGeV. (2 AGeV is only slightly above lowest mass Δ resonance threshold - 1232 MeV/c^2.) The proton widths and yields increase

as a function of beam energy. At 2 AGeV, a significant number of deuterons and tritons are created[Witt99], which may account for the lower number of observed free protons, as more of them are confined in bound states. As the beam energy increases, the number of protons is observed to increase, in line with the decreasing number of bound protons.
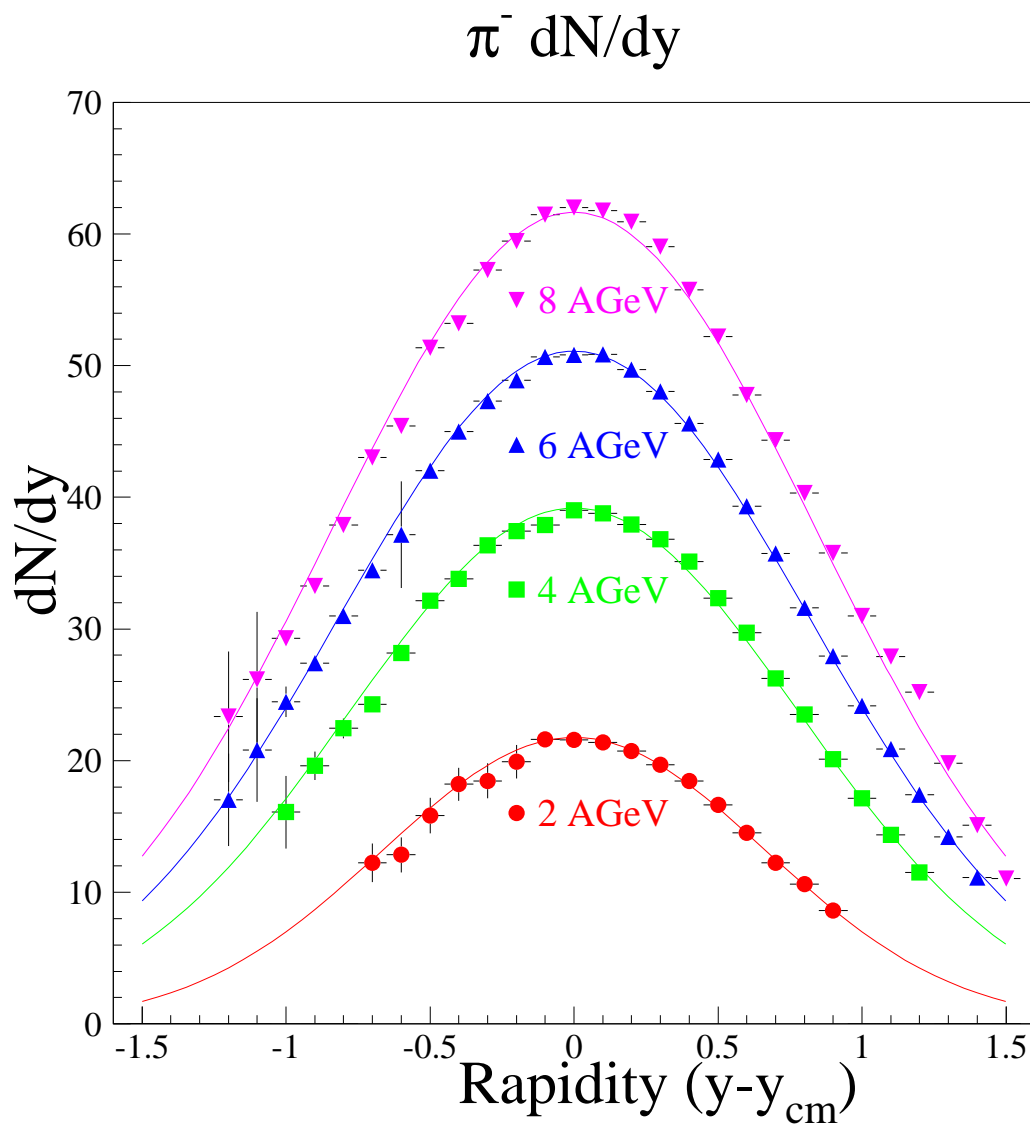
Figure 7.15: Yield per event of Negative Pions integrated over m_t-m_0 as a function of rapidity. A Gaussian model is applied to extract the 4π yields.
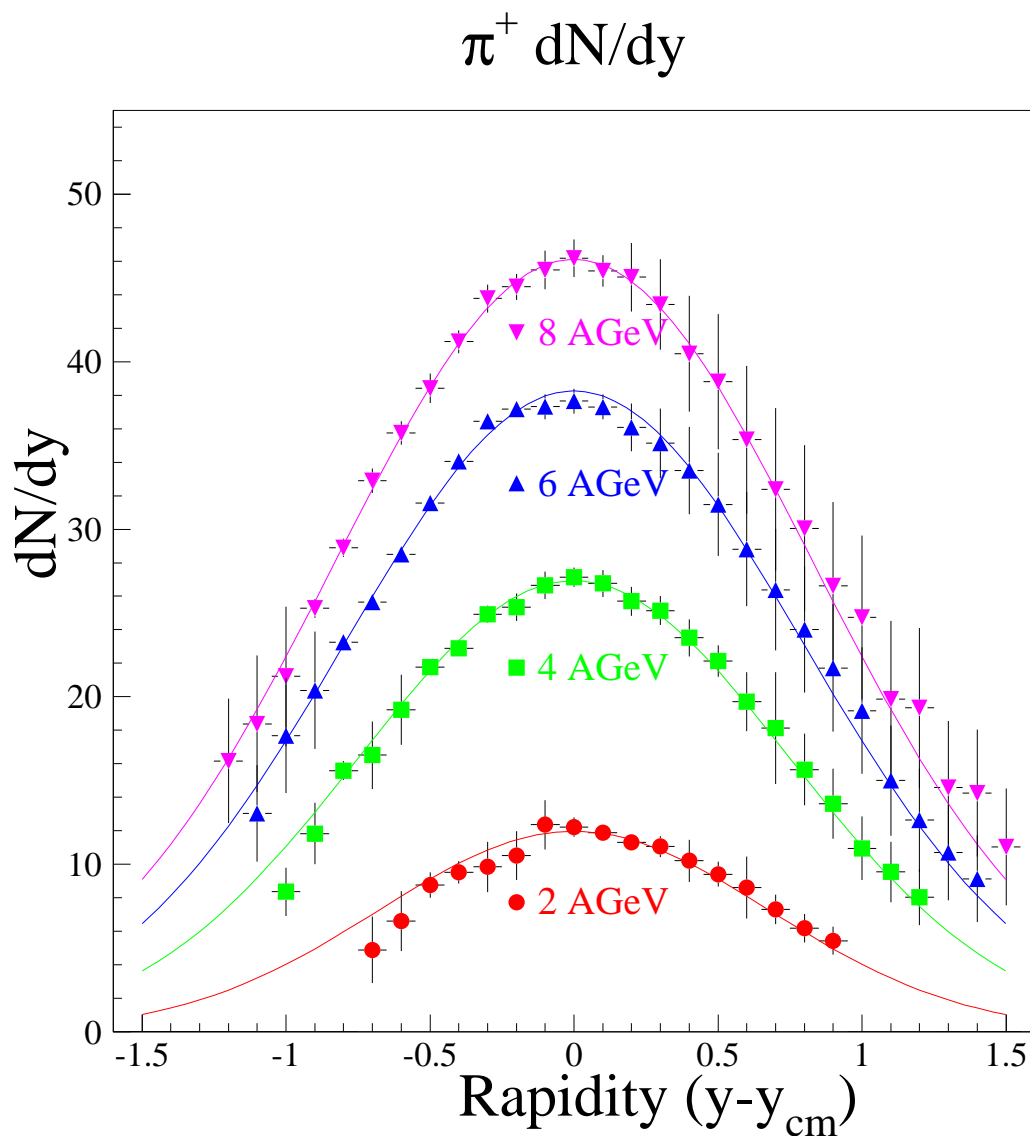
Figure 7.16: Yield per event of Positive Pions integrated over m_t-m_0 as a function of rapidity. A Gaussian model is applied to extract the 4π yields.

Proton dN/dy
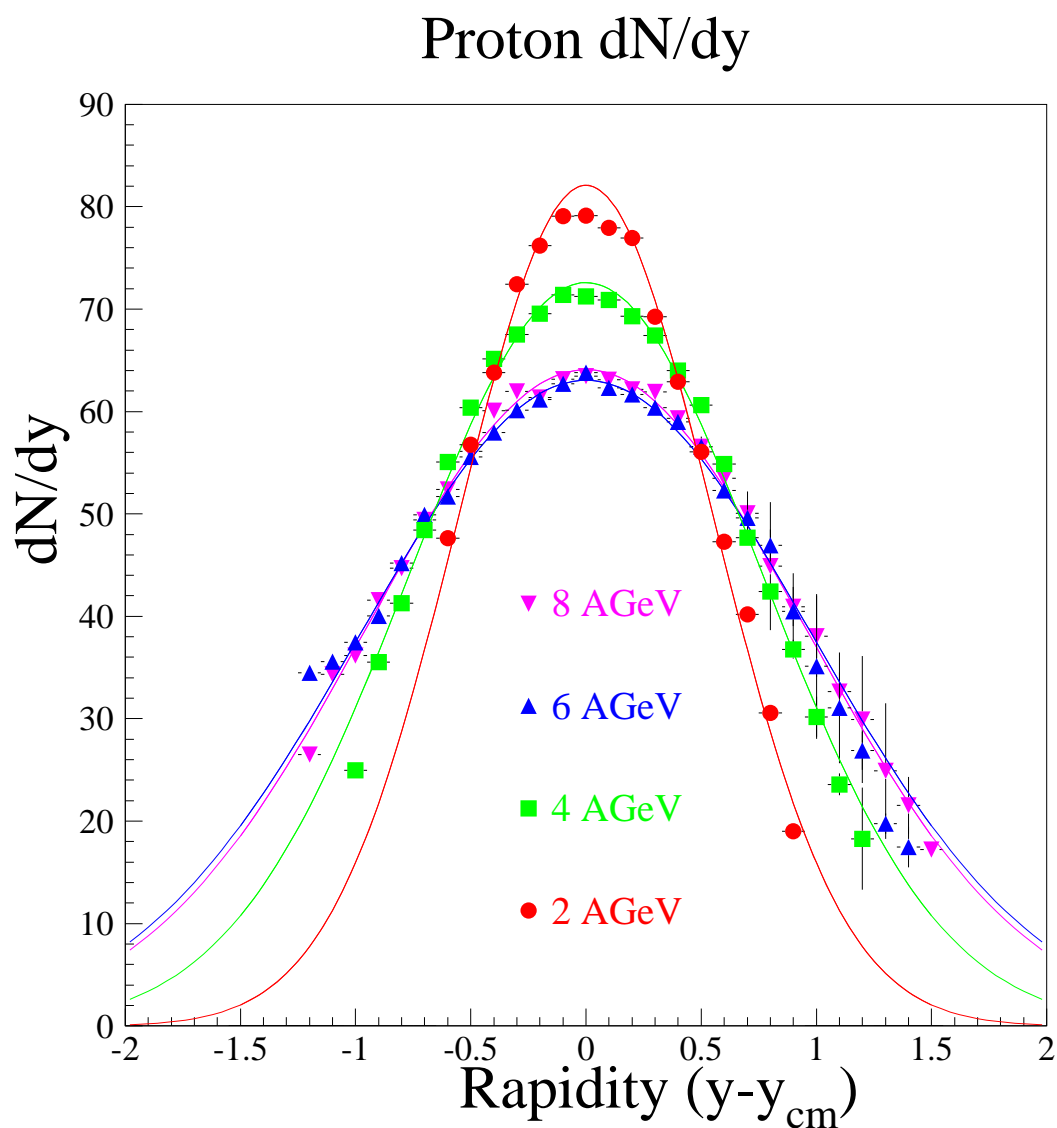
Figure 7.17: Yield per event of Protons integrated over m_t-m_0 as a function of rapidity. A Gaussian model is applied to extract the 4π yields.

E_{beam}	π^- dN/dy$_{(y=0)}$	$N_{\pi^-}(4\pi)$	σ_{π^-}
2 AGeV	21.6 ± 0.3	36.2 ± 0.5	0.664 ± 0.002
4 AGeV	39.0 ± 0.3	76.3 ± 0.5	0.777 ± 0.004
6 AGeV	50.8 ± 0.3	104.2 ± 0.5	0.814 ± 0.002
8 AGeV	62.0 ± 0.4	130.5 ± 2.0	0.844 ± 0.020

Table 7.1: dN/dy fit parameters for negative pions at each beam energy.

E_{beam}	π^+ dN/dy$_{(y=0)}$	$N_{\pi^+}(4\pi)$	σ_{π^+}
2 AGeV	12.2 ± 0.6	20.2 ± 0.9	0.673 ± 0.034
4 AGeV	27.1 ± 0.6	50.6 ± 1.0	0.750 ± 0.018
6 AGeV	37.6 ± 0.7	76.3 ± 0.8	0.796 ± 0.012
8 AGeV	46.2 ± 1.1	96.2 ± 3.0	0.832 ± 0.013

Table 7.2: dN/dy fit parameters for positive pions at each beam energy.

E_{beam}	p dN/dy$_{(y=0)}$	$T^{eff}_{(y=0)}$ (MeV/c^2)	$N_p(4\pi)$	σ_p
2 AGeV	82.2 ± 0.2	187 ± 1	113.7 ± 0.2	0.552 ± 0.001
4 AGeV	72.6 ± 0.3	216 ± 1	139.7 ± 0.3	0.768 ± 0.002
6 AGeV	63.0 ± 0.4	209 ± 1	154.9 ± 0.4	0.980 ± 0.003
8 AGeV	64.1 ± 0.3	221 ± 1	153.1 ± 0.3	0.953 ± 0.003

Table 7.3: dN/dy fit parameters for protons at each beam energy.

Chapter 8

Discussion

8.1 Overview

In this chapter, the results presented in Chapter 7 are discussed in the context of certain models which attempt to explain the collision dynamics based on the observed data. A comparison of the observed pion rapidity density distributions and 4π yields to the predictions from the transport model, RQMD v.2.3, are presented. The differences in the positive and negative pion yields are discussed and the 4π yields are used to estimate entropy production in the collision. The proton rapidity densities are considered under two scenarios - a hydrodynamical picture in which significant longitudinal flow develops and as a possible measure of incomplete nuclear stopping during the collision process.

8.2 Pions

As the most copiously produced particles, the analysis of the pion distributions is of particular interest in evaluating the dynamics occurring in relativistic heavy ion collisions. A large amount of the initial energy is converted into pions. It is interesting to note the asymmetry between the positive and negative pion yields at each beam energy. Although the ratio of negative to positive pions decreases over the studied beam energy range, from 1.79 at 2 AGeV to 1.39 at 8 AGeV, it does not reach the asymptotic value of ~ 1.0 observed at the CERN SPS.[Dunn97]

Qualitatively, the negative pion excess can be explained by considering the isospin dependence in the branching ratios of single particle pion production in nucleon-nucleon interactions:[Stoc86]

$$
\begin{array}{cccccccc}
 & \pi^- & & \pi^0 & & \pi^+ \\
nn & 5 & : & 1 & : & 0 \\
pp & 0 & : & 1 & : & 5 \\
np = pn & 1 & : & 4 & : & 1
\end{array}
$$

The branching ratios go like the absolute square of the scattering amplitudes, which are determined by the Clebsch-Gordan coefficients for the corresponding isospin combinations. (Pions are isospin I=$|1>$ particles, nucleons are I=$|1/2>$.) The ratios are inclusive, so they include all direct processes, such as direct pion production, (NN → NNπ) and production through nucleonic resonances such as the Δ (I=$|3/2>$) or N* (I=$|1/2>$), (NN → NΔ → NNπ). Since there are 118+118 neutrons compared to 79+79 protons in the Au+Au collisions under investigation, for the most central events, there are a maximum of $(118)^2$ possible nn collisions, $(79)^2$ possible pp collisions and $2(118)(79)$ possible np or pn collisions which could lead to pions.[Stoc86] By summing these production ratios weighted according to the pion branching ratios, the charged pions are expected to be produced in the ratio

$$
\frac{\langle N_{\pi^-}\rangle}{\langle N_{\pi^+}\rangle} \approx \frac{5N^2 + NZ}{5Z^2 + NZ} = 1.95 \tag{8.1}
$$

Roughly two negative pions to every one positive pion. The number of neutral pions falls in between. This is somewhat higher than is actually observed, even at 2 AGeV (see Table 8.1). The relative fractions need to be folded with the observed cross-sections for NN → NNπ from experimental measurements. These have been compiled by VerWest and Arndt [VerW82]. Combining their energy-dependent parameterization of the production cross-sections with the isospin fractions, the expected ratio of $\langle\pi^-\rangle$:$\langle\pi^+\rangle$ at 1 AGeV is $\sim$ 1.91:1. The 2 AGeV data, just above the Δ production threshold, are quite near, though a little lower than this predicted ratio. As the energy increases, the number of directly produced pion pairs $(\pi^-\pi^+,\pi^0\pi^0)$ is expected to lower the ratio, asymptotically approaching 1.0, which is the trend we observe. At 8 AGeV the negative pion excess is approximately 26%, compared to 44% at 2 AGeV.

8.2.1   RQMD Comparison

RQMD (Relativistic Quantum Molecular Dynamics) is a transport model which attempts to simulate, via Monte Carlo techniques, the nucleon interactions which occur in a heavy ion collision. This model has been reasonably successful in describing many final state observables experimentally measured in the beam energy range studied for this analysis.[Bass98]

In general, transport models operate by propagating individually the colliding

nucleons through the six dimensions of phase space (position and momentum).[1] In-teraction probabilities are approximated by using published interaction cross-sections of free nucleons and the relative phase space proximity of pairs of particles at each time step of the reaction. Inelastic collisions may produce new particles, such as pions, which are also propagated through phase space along with the nucleons. The reaction ends when the phase space density reaches a low enough threshold such that the probability of further interactions is small - the freeze-out point. No post freeze-out effects, such as the Coulomb interaction discussed in Chapter 5, are included in this model. All final-state particle distributions are frozen at the end of the reaction.

In-medium effects for nucleon-nucleon interactions can be included by using the 'mean field' setting, which scales the free nucleon cross-sections to mock up the in-medium dependence of the interaction probabilities.

RQMD version 2.3, with the nucleon mean field setting turned on, was used to predict 4π yields of charged pions to be compared to the measured values from this analysis. The beam energy, system (Au+Au) and impact parameter ranges (0-3.3 fm) were set to match the experimental conditions. Resonance particles produced in the reaction which may decay to pions were 'manually' decayed using published lifetimes correctly folded with their proper phase space positions following the prescription of Mike Lisa to account for all possible sources of final state pions.[Lisa98] All other

---

[1]This is in contrast to hydrodynamic models which model the system as a fluid, propagating the material using hydrodynamical transport equations.

E_{beam}	Measured π^-/π^+	RQMD v2.3 π^-/π^+
2 AGeV	1.792 ± 0.084	1.584
4 AGeV	1.508 ± 0.031	1.363
6 AGeV	1.366 ± 0.016	1.283
8 AGeV	1.357 ± 0.047	1.236

Table 8.1: Comparison of Charged Pion 4π yield ratios with RQMD model predictions.

tunable model settings were left at their default values.

The rapidity density distributions of charged pions predicted by RQMD are compared to the measured distributions at each beam energy in Figure 8.1. Qualitatively, the agreement is fairly good. The charged pion 4π yield ratios are compared in Table 8.1. Again, the agreement is qualitatively good. One possible explanation of the differences in the distributions and ratios may be due to the fact that the model does not include in-medium effects for pion interactions with the nucleons; pion-nucleon interactions are treated as free particle interactions.

8.2.2   Entropy production

It was suggested many years ago by Fermi[Ferm50] and later Landau[Land53] that pion production may be used to estimate the amount of entropy produced in a high energy collision. More recently, Van Hove[VanH82] extended this idea to heavy ion collisions and proposed that this may be a way to distinguish events in which a Quark Gluon Plasma (QGP) is formed. In a QGP the color degrees of freedom of the liberated partons introduce a significant number of new energy states unavailable in

RQMD Pion Comparison
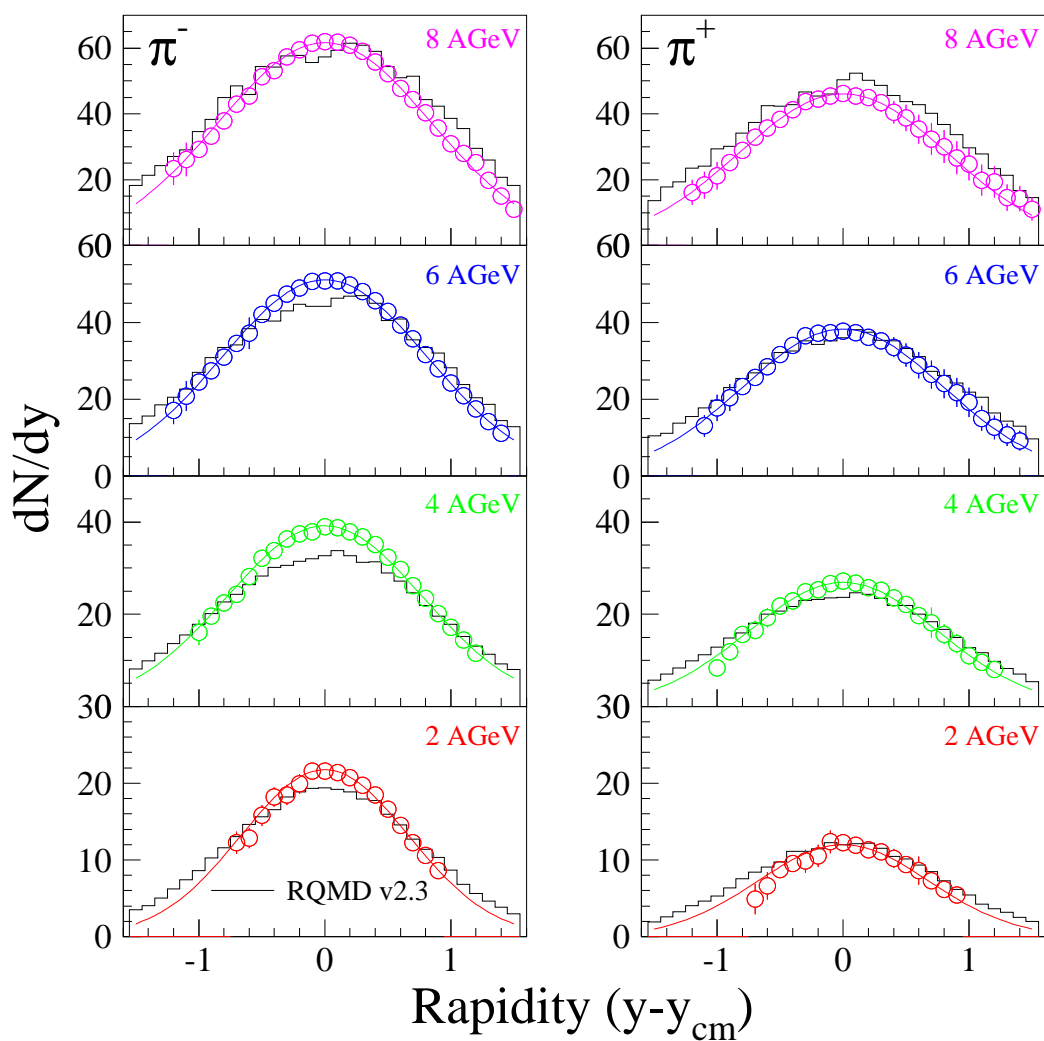
Figure 8.1: Comparison of measured charged pion rapidity density distributions to the predictions of RQMD v.2.3, with the mean field setting ON. The colored curves are Gaussian fits to the measured data.

a hadron gas. By studying pion production over a broad range of collision systems and energies, discontinuities in the observed multiplicities might indicate the onset of QGP formation.

In 1995, Gaździcki [Gaźd95a] took the available data from heavy ion collisions and showed that there is an increase in the observed entropy produced at AGS energies compared to the SPS (NA35 Experiment with S+S collisions at 200 AGeV[Bäch94]). The low energy heavy ion data follow the trend for p+p collisions, while at the SPS there is an apparent factor of 3 increase in the effective number of degrees of freedom. [Gaźd95b] The entropy production analysis of Pb+Pb collisions at 158 AGeV (NA49) by Brady and Dunn[Brad98] confirmed Gaździcki's observation. Figure 8.2 from [Seyb01] shows the heavy ion data, including new data from NA49 at 40 AGeV and the early RHIC results from the PHOBOS Experiment[Back00] compared with data from p+p and p+$\overline{p}$ data. The pions presented in this dissertation fill in the systematics at lower energy.

The model of entropy production in central nucleus-nucleus collisions introduced by Landau[Land53] assumes that the entropy is produced at the early stage of the collision when all of the incident matter is in a highly excited state, produced by complete stopping of the incident nuclei. The thermalized strongly interacting matter is assumed to expand adiabatically to the freeze-out point, preserving the early stage entropy. The collision energy density, ϵ, available for particle production can be
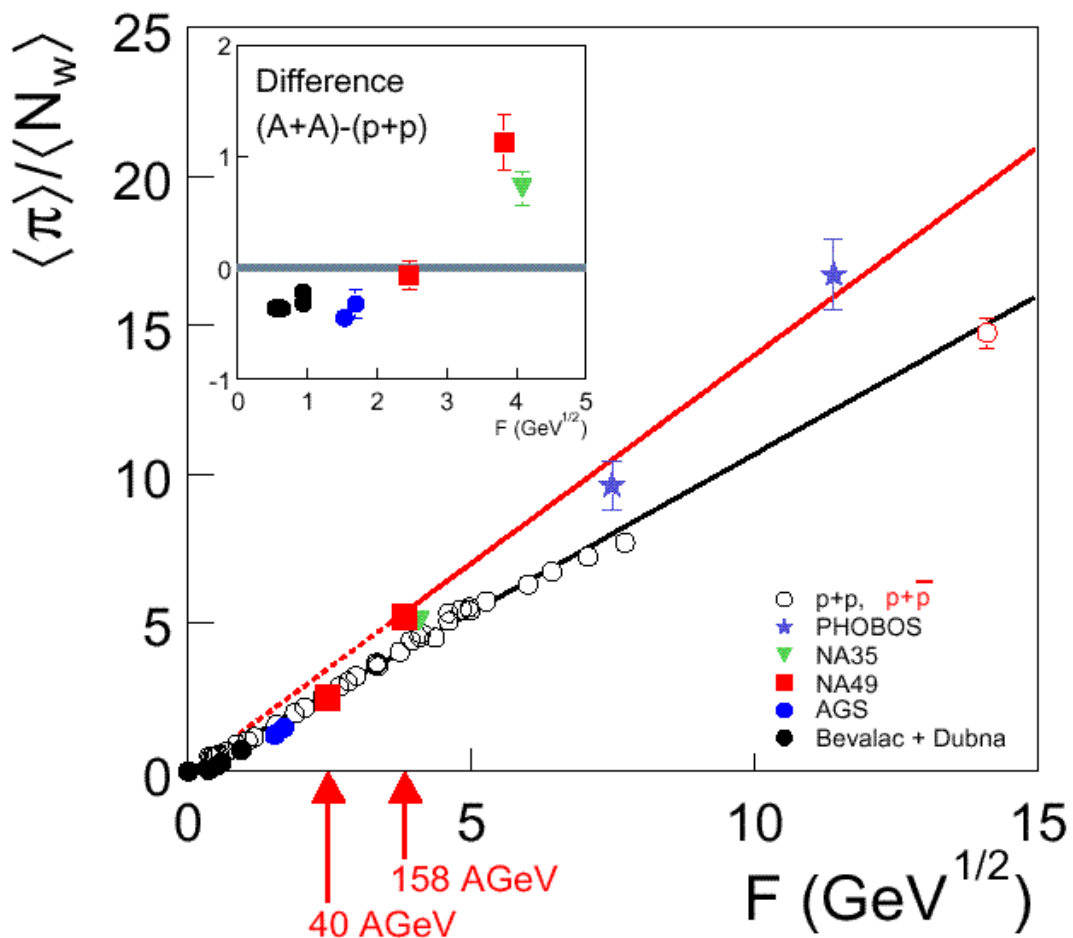
Figure 8.2: Entropy per participant vs. F (Fermi energy variable).[Seyb01] (Only the pion multiplicities were used.) A change in behaviour between the AGS and the top energy SPS is evident. The recent RHIC data[Back00] continue the observed enhancement trend.

estimated from the Lorentz-contracted volume of the overlapping nuclei and the center of mass energy

$$V \sim \frac{V_0}{\gamma} = \frac{2m_N V_0}{\sqrt{s_{NN}}} \tag{8.2}$$

$$\epsilon = \frac{E}{V} \sim \frac{(\sqrt{s_{NN}} - 2m_N)\sqrt{s_{NN}}}{2m_N V_0}. \tag{8.3}$$

Since the majority of produced particles are pions, to first order, the mean pion (boson) multiplicity should be nearly proportional to the entropy. In order to relate the entropy density, σ to the energy density, an equation of state (EOS) must be assumed. For a simple approximation, Landau assumed the EOS of a massless relativistic gas of pions[Land53]

$$p = \frac{1}{3}\epsilon, \tag{8.4}$$

where p is the pressure and ϵ is the energy density. For a relativistic blackbody with $\epsilon \sim T^4$, the entropy density is related to the energy density as

$$T\sigma = \epsilon + p - \mu n = \frac{4}{3}\epsilon. \tag{8.5}$$

The chemical potential, μ, being zero for massless pions implies

$$\sigma \sim \epsilon^{3/4}. \tag{8.6}$$

By substituting the energy density, Equation 8.3, into Equation 8.6, and multiplying by the initial state volume, Equation 8.2, the early stage entropy can be expressed

$$S_E \sim V((\sqrt{s_{NN}} - 2m_N)\sqrt{s_{NN}})^{3/4}. \tag{8.7}$$

Unfortunately, even in the most central collisions of identical nuclei, the participation of all nucleons is not assured. The volume must be scaled according to the average number of participant nucleons, based on the centrality selection of the total reaction cross-section. The average number of participants for a nucleus-nucleus collision can be estimated using the inelastic cross-section for nucleon-nucleon interactions ($\sigma_{NN} \approx 32$ mb) and a geometric Glauber model calculation of the mean free path of the nucleons through the nuclei as they collide at a given impact parameter.[Wong94]

$$\langle N_P \rangle = \frac{\sigma_{pA}}{\sigma_{AA}}(A + A) \tag{8.8}$$

where σ_{pA} and σ_{AA} are production cross-sections in nucleon-nucleus and nucleus-nucleus collisions, respectively. For 5% most central events, the average number of participants is approximately[Salm93]

$$\langle N_P \rangle \simeq 0.87(A + A) \approx 343 \tag{8.9}$$

Expressing the volume in terms of $\langle N_P \rangle$, the early stage entropy, Equation 8.7, can be re-written

$$S_E \sim \langle N_P \rangle \frac{(\sqrt{s_{NN}} - 2m_N)^{3/4}}{\sqrt{s_{NN}}^{1/4}} \tag{8.10}$$

This $\sqrt{s_{NN}}$ dependence is the same as that obtained by Fermi[Ferm50] for high energy collisions. He defined a new variable F:

$$F \equiv \frac{(\sqrt{s_{NN}} - 2m_N)^{3/4}}{\sqrt{s_{NN}}^{1/4}}. \tag{8.11}$$

The average pion multiplicity is therefore linearly related to the Fermi energy variable, F through the number of participants.

$$\langle \pi \rangle \sim \langle N_P \rangle F. \tag{8.12}$$

The entropy must also include contributions from other produced particles, notably kaons, and the energy which is required to heat the incident nucleons up to the thermalized system temperature. A modified version of the expression used by Gaździcki to generalize the total entropy is

$$S \quad \simeq \quad (\langle \pi^- \rangle + \langle \pi^0 \rangle + \langle \pi^+ \rangle) + \kappa \langle K + \overline{K} \rangle + \delta \langle N_P \rangle \tag{8.13}$$

$$S \quad \sim \quad \langle N_P \rangle F. \tag{8.14}$$

The first term separates the isospin triplet of pions to account for the differences in the production ratios of pions in our energy range. The next term takes into account the entropy used to produce kaons, which can be estimated from the measurements of E917[Dunl99]. The factor $\kappa \approx 1.45$ introduced by Gaździcki is the ratio of the entropy per kaon to the entropy per pion at a freeze-out temperature of 150 MeV, but he notes that this value very weakly depends on the assumed freeze-out temperature. The last term accounts for the entropy required to raise the temperature of the participating nucleons during the collision. The factor $\delta \approx 0.35$, is an empirical value obtained by Gaździcki from an observed offset in the pion multiplicities as a function of F.[Gaźd95b]

Figure 8.3 shows the entropy per participant using Equation 8.14 from [Brad98],

$\sqrt{s_{NN}}$ (GeV)	F (GeV$^{1/2}$)	$\langle\pi^+\rangle$	$\langle\pi^0\rangle$	$\langle\pi^-\rangle$	$\langle K+\overline{K}\rangle$	S/$\langle N_p\rangle$	Ref.
2.630	0.644	20.2	*28.2*	36.2	0.78	0.600	*This work*
3.279	0.965	50.6	*63.5*	76.3	6.01	0.931	*This work*
3.838	1.190	76.3	*90.3*	104.2	13.26	1.196	*This work*
4.289	1.351	96.2	*113.3*	130.5	21.87	1.434	*This work*
8.830	2.488	*313*	*313*	313	74	3.348	[Seyb01]
17.260	3.813	*610*	*610*	610	145	6.146	[Seyb01]

Table 8.2: Tabulated Entropy variables. The $\langle\pi^0\rangle$ values, shown in italics, are averages of the measured charged pion values. The values calculated from [Seyb01] are for central Pb+Pb collisions at 40 AGeV ($\langle N_{part}\rangle$=349) and 158 AGeV ($\langle N_{part}\rangle$=352) from NA49 (where the total pion multiplicities are assumed to be $\langle\pi\rangle \approx 3*\langle\pi^-\rangle$).

with the E895 data shown in red. Table 8.2 contains the tabulated information used to calculate the entropy per participant nucleon. The E895 neutral pion values were obtained by taking the average of the charged pion values, since the isospin dependence of the production cross-sections for the neutron excess implies $\langle\pi^-\rangle > \langle\pi^0\rangle > \langle\pi^+\rangle$. NA49 results for 40 AGeV and 158 AGeV Pb+Pb collisions from the CERN SPS were calculated from values presented in [Seyb01]. The number of participant nucleons quoted in [Seyb01] are $\langle N_{part}\rangle = 349$ for 40 AGeV and $\langle N_{part}\rangle$=352 for 158 AGeV. At these energies, the charged and neutral pions are assumed to be produced in approximately equal numbers.

8.3 Protons

The characterization and interpretation of the proton distributions produced in heavy ion collisions are also important to our understanding of the dynamics of "hot,

Entropy Production
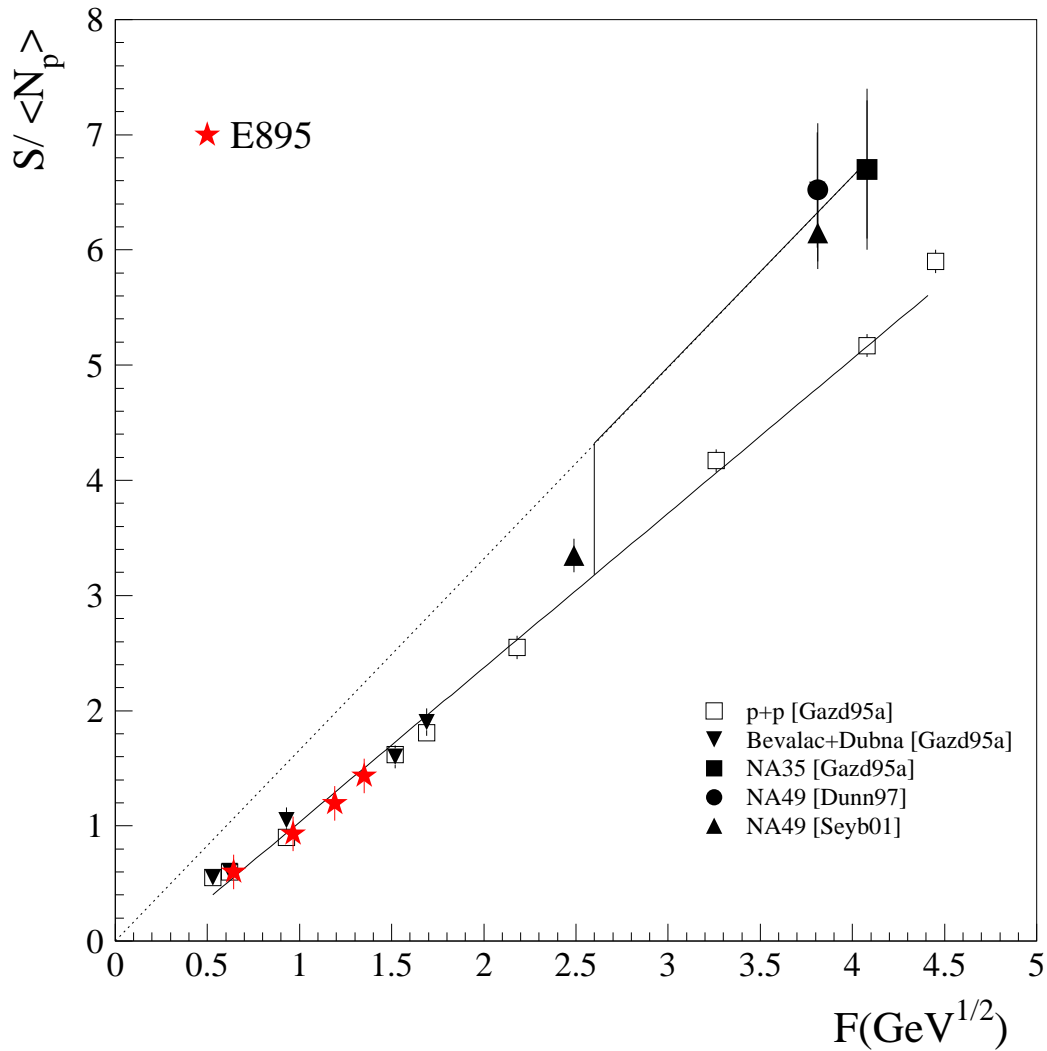
Figure 8.3: Entropy per participant vs. F, the Fermi energy variable. The solid symbols represent data from heavy ion collisions, whereas the open symbols come from p+p interactions. The E895 data points are indicated by red stars. The vertical line is included to indicate the possibility of a discontinuity in the entropy as a function of F, though its location in F is arbitrary.

dense" nuclear matter. As is evident from the nuclear matter phase diagram, Figure 1.1, there exists a continuum of critical temperatures and baryon densities at which a phase transition from a hadron gas to a Quark Gluon Plasma (QGP) might occur. By studying stopping in heavy ion collisions as a function of beam energy, we hope to be able to determine whether the energy densities attained in the collisions are high enough to allow a phase transition to a QGP state. Although a phase transition is not likely in the beam energy range of study for this dissertation, it is important to establish the baseline from which anomalous behaviour may be compared.

We know the initial (pre-collision) and final states of the proton distributions as a function of rapidity. Our goal is to be able to say something about the collision dynamics at the point of impact from our observations of the final state. This is somewhat difficult, given that very different scenarios for the early time of the collision can lead to similar patterns in the final state. In particular, there are two distinct signatures which may be inferred from the observed proton rapidity densities: incomplete stopping/nuclear transparency and longitudinal hydrodynamic flow. While the true situation is likely a combination of these two effects, they cannot be easily disentangled. In the next two sections, both of these interpretations of the observed proton rapidity densities at 2, 4, 6 and 8 AGeV will be discussed.

8.3.1 Baryon Stopping

The efficiency in converting the incoming longitudinal energy in a pA or AA collision to transverse or other degrees of freedom is known as stopping. [Busz84] The degree of stopping depends on the nature of the interactions of the nucleons in the collision. In an extremely relativistic collision, the nuclei become almost transparent to one another. In analogy to the deep-inelastic scattering experiments which confirmed the existence of quarks, large momentum transfer collisions between the nucleons are approaching asymptotic freedom. The dissociating nuclei pass through each other losing only a fraction of their initial longitudinal momenta. In the Bjorken scenario, what is left at mid-rapidity is a highly excited baryon-free vacuum, approaching nuclear size, from which gluons and quark-antiquark pairs emerge, forming a QGP.[Bjor83]

Stopping is typically estimated by studying the average rapidity loss of baryons. $\langle \delta \mathrm{y} \rangle$

$$\langle \delta y \rangle = y_p - \langle y_b \rangle, \tag{8.15}$$

where y_p is the projectile rapidity and $\langle \mathrm{y}_b \rangle$ is the average net baryon rapidity after the collision.[Vide95] The average rapidity loss can be evaluated by using

$$\langle \delta y \rangle = \frac{\Sigma |y - y_b|(dN_p/dy)}{\Sigma (dN_p/dy)}, \tag{8.16}$$

where y_b is the beam projectile rapidity, and $\mathrm{dN}_p/\mathrm{dy}$ is the proton rapidity density.

At high energies, where the rapidity gap between target and projectile is large (≥ 6 units of rapidity), an average rapidity loss of $\langle \Delta y \rangle \approx 2$ units implies a net loss of $\approx 90\%$ of the nucleons' incident longitudinal energy and would leave the central rapidity region practically baryon-free.[Barr94]

Experimentally, net proton rapidity densities from Pb+Pb collisions at 158 AGeV [Appe99] show a distinct double-humped character which is suggestive of a large degree of nuclear transparency. However, if indeed a QGP is formed at those beam energies it is not yet a baryon-free plasma; the central rapidity region is not completely evacuated of net baryon number. The two humps are elongated and are peaked at rapidities approximately 1.3 units away from mid-rapidity (see Figure 8.4). At the lower incident beam energies ($\sim$ 250 AMeV - 1.0 AGeV) of the Bevalac and SIS facilities, a higher degree of stopping is inferred from the pile-up of protons at mid-rapidity.[Herr96] Figure 8.4 reproduces the measured proton rapidity densities at SIS[Herr96] and the top energy of the AGS[Back01], and the net proton (p-$\overline{p}$) rapidity density at the CERN SPS [Appe99]. From the Figure, there appears to be a transition in behaviour as a function of beam energy, but the relative rapidity loss, $\langle \delta y \rangle / \delta y_{max}$ is constant, within the experimental uncertainties, over this energy range.

Table 8.3 shows the absolute $\langle \delta y \rangle$ and relative $\langle \delta y \rangle / \delta y_{max}$ rapidity losses at each beam energy. As the beam energy increases, so does the size of the rapidity gap from target to projectile. Therefore, the range of rapidities used to calculate the
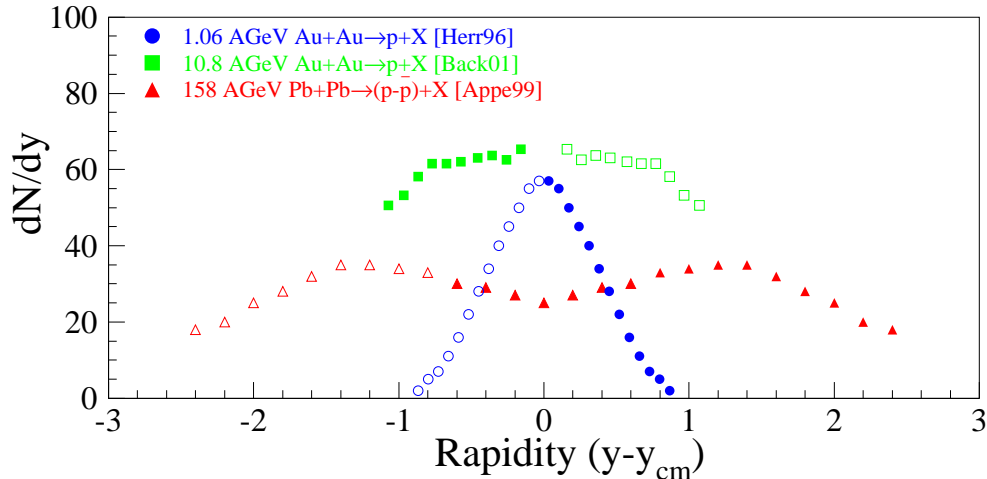
Figure 8.4: dN/dy distributions of protons from the top energy at SIS (1.0 AGeV Au+Au) [Herr96], the top energy of the AGS (10.8 AGeV Au+Au) [Back01], and net protons at the top energy of the CERN SPS (158 AGeV Pb+Pb). [Appe99]

loss, Equation 8.16, was -0.5 to 0.5 for 2 AGeV (due to the smaller available gap) and -1.0 to 1.0 for 4, 6, and 8 AGeV. The increase in the absolute rapidity loss as a function of beam energy might be interpreted as an indication of an increase in the amount of stopping, but the relative loss remains fairly constant. Indeed, this is in agreement with the observation reported in [Vide95] of a flat dependence of the relative rapidity loss, $\langle \delta y \rangle / \delta y_{max}$, from the AGS to the SPS, and extended to lower energies (using Ni+Ni collisions) by the FOPI Collaboration.[Hong98] For comparison, the recently reported values at 6, 8 and 10.8 AGeV from E917[Back01], and the values from [Vide95] are also included. Yet, the proton rapidity distributions show a broadening which is not consistent with a complete stopping scenario. Is the

E_{beam} (AGeV)	System	$\langle \delta y \rangle$	$\langle \delta y \rangle / y_{beam}$	Ref.
1.06	Au+Au	0.49 ± 0.02	0.70 ± 0.02	[Herr96] *analysed here*
2	Au+Au	0.61 ± 0.02	0.70 ± 0.02	*This work*
4	Au+Au	0.84 ± 0.04	0.72 ± 0.04	*This work*
6	Au+Au	0.95 ± 0.02	0.70 ± 0.02	*This work*
8	Au+Au	1.01 ± 0.04	0.69 ± 0.04	*This work*
6	Au+Au	0.96 ± 0.04	0.71 ± 0.03	[Back01]
8	Au+Au	1.01 ± 0.04	0.69 ± 0.04	[Back01]
10.8	Au+Au	1.07 ± 0.05	0.66 ± 0.05	[Back01]
11.6	Au+Au	1.02	0.64	[Vide95]
158	Pb+Pb	1.76 ± 0.05	0.61 ± 0.02	[Back01],[Appe99]

Table 8.3: Absolute and relative rapidity loss of protons as a function of beam energy, evaluated using Equation 8.16. The absolute loss increases with beam energy, while the relative loss remains fairly constant.

origin of this broadening due to an increase in transparency or a hydrodynamical evolution of a completely stopped system? This remains an open question. In the next section, the hydrodynamical picture will be addressed.

8.3.2 Longitudinal Flow

The rapidity density for purely thermal emission from a stationary source isotropically radiating particles of a given mass can be obtained by integrating the Maxwell-Boltzmann distribution, Equation 7.3, with the implicit rapidity dependence of the parameters $A(y) \propto m cosh(y-y_{cm}) exp[\mu/T_{chem}-m/T(y)]$ and $T(y) = T/cosh(y-y_{cm})$ revealed[Schn93]

$$\frac{dN_{th}}{dy} = AT^3(\frac{m^2}{T^2} + \frac{m}{T}\frac{2}{\cosh y} + \frac{2}{\cosh^2 y})e^{(-\frac{m}{T}\cosh y)}. \qquad (8.17)$$

The width of the distribution, Equation 8.17, for a given emitted particle is determined by the particle mass and temperature. One would expect that in a thermalized system, in which all particles have a common temperature, the widths of the rapidity densities for different particles would vary with the particle masses. The data do not support this view. The experimentally observed rapidity densities of the protons and pions have comparable Gaussian widths, broader than suggested by Equation 8.17 (see Tables 7.1, 7.2,7.3), which do not vary like their mass ratio (≈ 7).

Hydrodynamical considerations can be used to interpret the elongation of the particle rapidity densities as a collective fluid flow driven by the pressure gradients which develop in a highly excited thermal fireball. Figure 8.6 shows the proton rapidity densities at 2, 4, 6, and 8 AGeV with the stationary thermal source assumption shown in black. Since the rapidity densities are fairly insensitive to the temperature gradients, [Schn93] the mid-rapidity temperatures from the transverse mass spectra fits, listed in Table 7.3, were used to compute the curve representing Equation 8.17. The data are much broader than this model can explain. Schnedermann, Sollfrank and Heinz[Schn93] proposed a method of evaluating the increase in the widths as the result of collective longitudinal flow. This is achieved by assuming that the observed distributions arise from the superposition of multiple boosted individual isotropic, locally thermalized sources in a given rapidity interval. This is reminiscent of the Hagedorn definition of the fireball in which each local region is a fireball in its own

right.[Hage73] For this analysis, the "temperatures" are fixed by the measured slope parameters of the transverse mass spectra at mid-rapidity and the distributions are integrated over rapidity to extract the maximum longitudinal flow from the free parameter, η_{max}

$$\frac{dN}{dy} = \int_{\eta_{min}}^{\eta_{max}} d\eta \frac{dN_{th}}{dy}(y - \eta) \qquad (8.18)$$

$$\beta_L = \tanh(\eta_{max}). \qquad (8.19)$$

where $\eta_{max} = - \eta_{min}$, from symmetry about the center of mass; $\frac{dN_{th}}{dy}$ is Equation 8.17 with N_{th}, the number of particles from a thermal source of temperature T; T is the temperature of the system; m is the mass of the emitted particle; N is the total number of particles observed; and β_L is the maximum longitudinal velocity in units of c.

The variable η was introduced in [Schn93] to describe the range of rapidity over which the thermal dN/dy given by Equation 8.17 is boost-invariant. (The reader should not confuse this with the pseudo-rapidity, $\eta = -ln[tan(\theta/2)]$, which is a geometric variable relating to the polar angle between a particle's momentum vector and the beam axis.) Fits of this form have been applied to a wide array of experimental data at the AGS and the SPS.[Schn93], [Brau95], [Stac96], and [Herr99] Figure 8.5, from [Stac96] shows the average longitudinal flow velocities,

$$\langle \beta_L \rangle = tanh(\eta_{max}/2) \qquad (8.20)$$
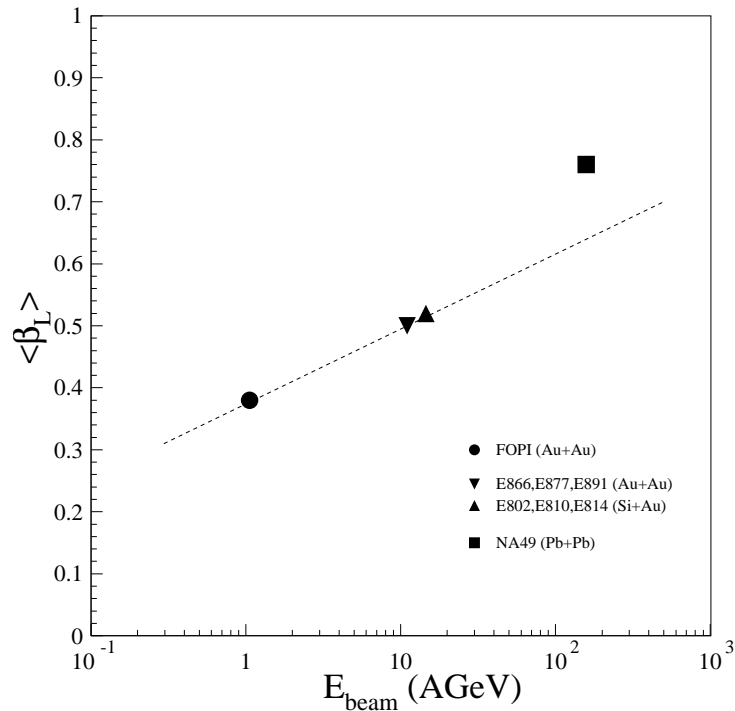
Figure 8.5: Energy excitation function of longitudinal flow velocities, $\langle\beta_L\rangle$, compiled by [Stac96]. The line is drawn to guide the eye and suggests there is an enhancement over the expectation for the SPS.

introduced by averaging over the forward(backward) portion of the distribution given by Equation 8.18, as a function of beam energy. The line is drawn to guide the eye and to suggest that there is an enhancement over the expectation for the SPS compared to SIS and the AGS.

Fits of Equation 8.18 to the proton rapidity densities at 2, 4, 6, and 8 AGeV are shown as the colored curves on Figure 8.6. The inverse slope parameters obtained from the transverse mass fits are used for the temperature. The fit parameters, η_{max} and

E_{beam} (AGeV)	System	η_{max}	β_L	$\langle\beta_L\rangle$	$\langle(\beta\gamma)_L\rangle$	Ref.
1.06	Au+Au	0.37	0.35	0.19	0.194	*(This work)*
1.15	Au+Au	0.41	0.39	0.20	0.204	*[Liu98]*
2 (1.85)	Au+Au	0.569 ± 0.002	0.65	0.28	0.314	*This work*
4 (3.91)	Au+Au	0.864 ± 0.002	0.70	0.41	0.450	*This work*
6	Au+Au	0.991 ± 0.010	0.76	0.46	0.518	*This work*
8	Au+Au	1.057 ± 0.025	0.78	0.48	0.547	*This work*
6	Au+Au	0.990	0.76	0.46	0.518	*[Back01]*
8	Au+Au	1.086	0.80	0.50	0.577	*[Back01]*
10.8	Au+Au	1.166	0.82	0.52	0.609	*[Back01]*
11	Au+Au	1.10	0.80	0.50	0.577	*[Stac96]*
14.6	Si+Al	1.15	0.82	0.52	0.609	*[Brau95]*
158	Pb+Pb	1.99	0.96	0.76	1.169	*[Stac96]*
200	S+S	1.70	0.94	0.69	0.953	*[Schn93]*

Table 8.4: Longitudinal Flow parameters extracted from fits of Equation 8.18 to the proton rapidity densities at 2, 4, 6, and 8 AGeV. Compiled data at other beam energies from the listed references are also included for comparison.

the corresponding velocities, β_L and $\langle\beta_L\rangle$ are listed in Table 8.4. $\langle(\beta\gamma)_L\rangle$ is evaluated by computing $\gamma = 1/\sqrt{1 - \langle\beta_L\rangle^2}$. It is interesting to note that often $\beta_{max} > 1/\sqrt{3}$, the speed of sound in an ideal fluid.

Multiple particle species can be simultaneously fit for an average longitudinal flow of the system. The pion rapidity densities are shown along with the protons in Figure 8.7. Stationary thermal source emission functions, the sum of two thermal distributions, Equation 8.17, using the two yield and slope parameters from the pion transverse mass spectra fits (see Chapter 7), are shown in black. Also indicated by the colored curves are the emission functions including longitudinal flow, with the velocities fixed to the values extracted from the protons. At 2 AGeV, the difference
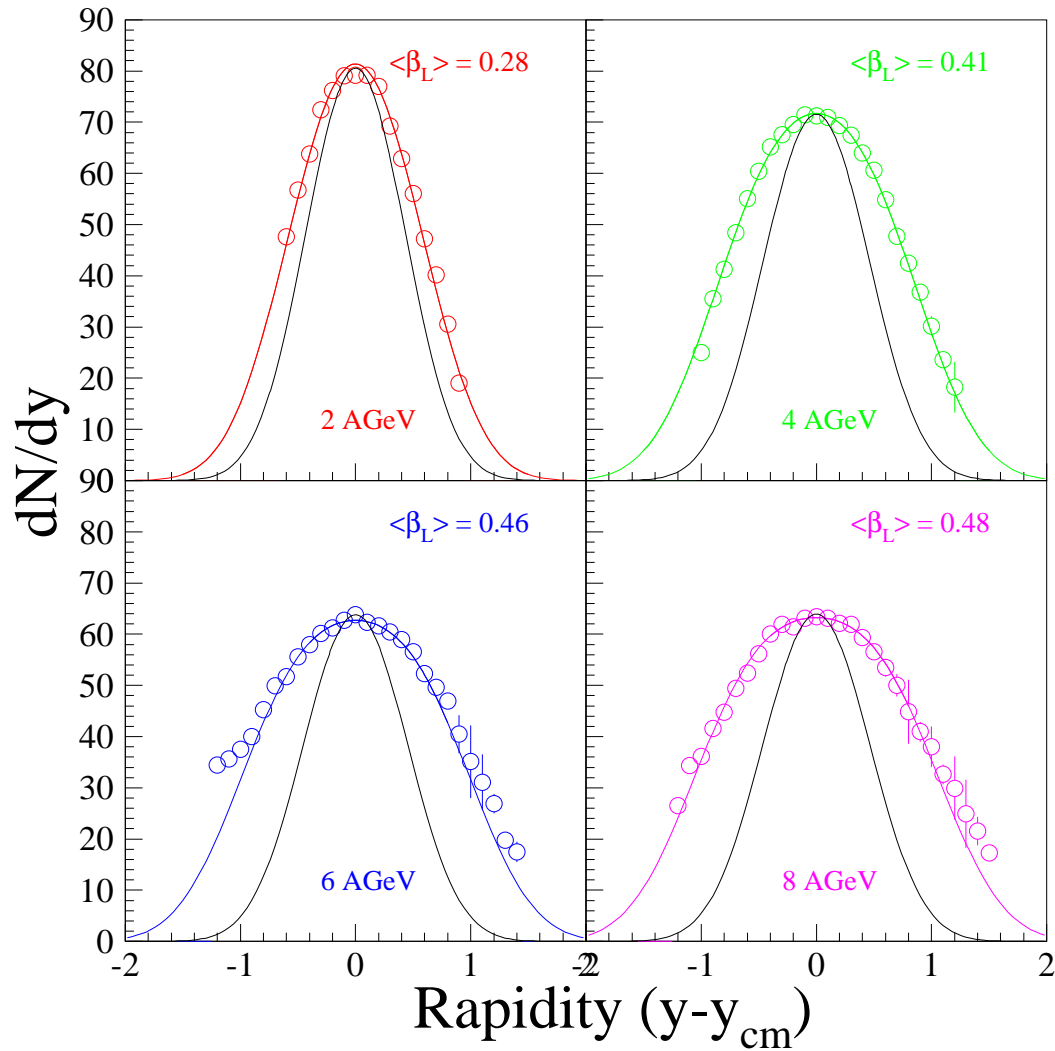
Figure 8.6: Proton rapidity density distributions at 2,4,6, and 8 AGeV. The black curves indicate the expectation for isotropic emission from a stationary thermal source with temperatures given by the inverse slope parameters from the transverse mass fits, whereas the colored curves indicate fits with longitudinal flow.

between the stationary and flowing sources is difficult to discern for the pions. However, the longitudinally expanding source clearly better reproduces the measured pion distributions at 4, 6 and 8 AGeV. Consistency among particles of different masses supports the hydrodynamical interpretation; the system is expanding like a fluid with a common longitudinal flow velocity. This suggests that a comparison of the produced particle distributions (*e.g.* the pions) with the proton distributions can be used to distinguish stopping from collective flow effects.

The extracted velocities exhibit a roughly linear increase as a function of beam energy in this range. A comparison of these results with the compiled data from [Schn93], [Brau95], [Stac96], [Herr99], [Liu98] and [Back01] is shown in Figure 8.8, where $\langle (\beta\gamma)_L \rangle$ is plotted versus the beam energy.

Based on the trend observed in our data, which extends to the higher beam energies, a modification to a previous interpretation of the lowest energy FOPI data point has been adjusted here. The longitudinal flow reported for 1.06 AGeV Au+Au in [Stac96], [Herr99], and [Wess97] was from an interpretation of the measured data from [Herr96] which assumed isotropic emission from a Siemens and Rasmussen[Siem79] radially boosted thermal source. [Herr96] reported good agreement between their Au+Au data and a model of the rapidity density distributions including radial flow. The flow velocity and temperatures used to make this comparison were extracted from boosted thermal fits to the mid-rapidity kinetic energy spectra. A temperature

of 80 MeV and an average (isotropic) flow velocity of $\langle \beta_r \rangle = 0.41c$ were reported.

While theirs may be a valid interpretation, the longitudinal flow velocity of $\langle \beta \rangle$ = 0.38c attributed to the 1.06 AGeV Au+Au data by [Stac96] is a factor of two larger than the value one extracts using the prescription of Schnedermann, Sollfrank and Heinz. In order to make a direct comparison of the longitudinal flow values from different experiments, it is important to apply the same model in each case. Therefore, I have performed a re-analysis of the FOPI 1.06 AGeV Au+Au proton rapidity density distributions for this dissertation using their reported temperature of 80 MeV with Equation 8.18. This model produces an average longitudinal flow of $\langle \beta_l \rangle = 0.19c$, which is consistent with a value purported to be calculated from Au+Au collision data measured by the EOS collaboration at the Bevalac for E_{beam}=1.15 AGeV and reported in [Liu98].

The linear systematic trend previously reported [Stac96], [Herr99], [Wess97] is still evident in the excitation function, but the slope has increased by a factor of ≈ 2.5 to include the data in this dissertation. The CERN SPS values show a much less significant excess above the new systematic. Within the context of this single model, all of the heaviest beam (Au+Au and Pb+Pb) data appear to obey a linear excitation over three orders of magnitude in beam energy.
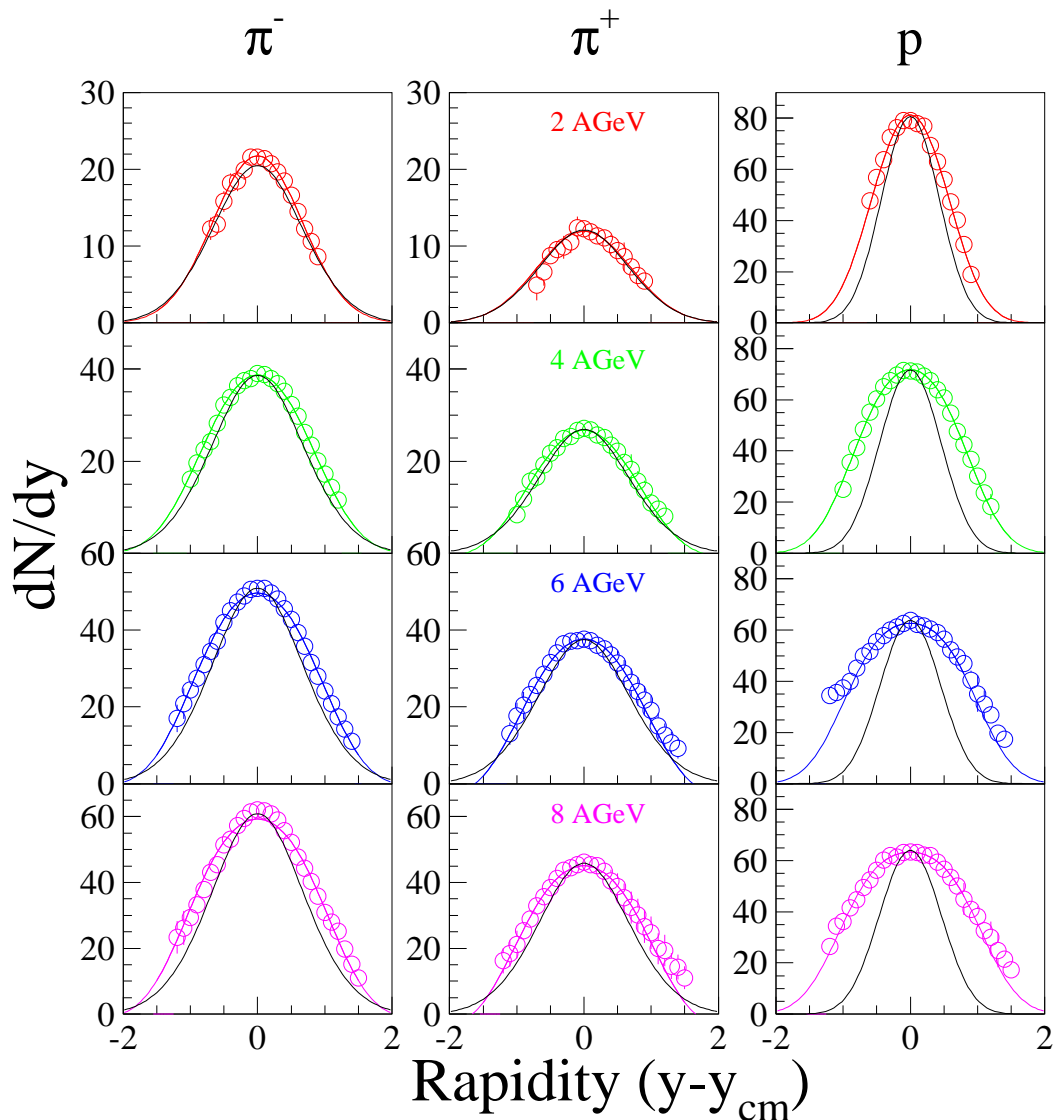
Figure 8.7: π^-, π^+ and proton rapidity density distributions at 2,4,6, and 8 AGeV. The expectation for isotropic emission from a stationary thermal source is indicated in black, whereas the colored curves represent the form including longitudinal flow from the proton η_{max} values listed in Table 8.4. In the case of the 2 AGeV pions, the isotropic source is barely distinguishable from the flowing source.
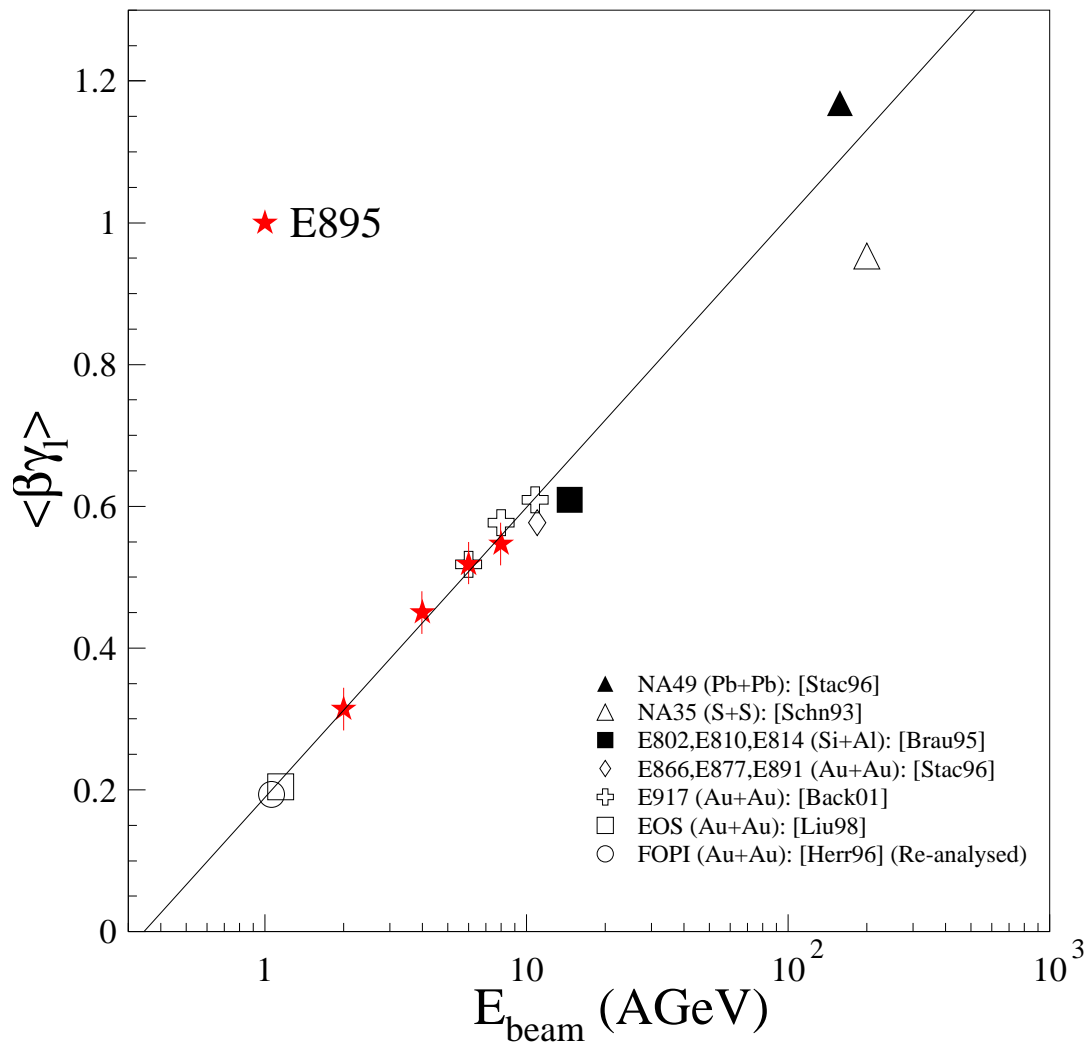
Figure 8.8: Energy excitation function of longitudinal flow velocities ($\langle\beta\gamma\rangle_l$), from heavy ion collisions. A roughly linear dependence over three orders of magnitude of beam energy is observed.

8.4   Conclusions

The full phase space momentum spectra of pions and protons have been measured for Au+Au collisions at 2, 4, 6, and 8 AGeV beam energies. Pion production increases as a function of the beam energy and the ratio of positive to negative pions is observed to approach but not attain the asymptotic limit. A study of the pion multiplicities as a measure of the entropy produced in heavy ion collisions confirms the baseline established by [Gaźd95a] and [Brad98] and supports the interpretation that there is a significant increase in entropy production between the AGS and the SPS. Whether this increase appears as a discontinuity or a smooth transition remains to be established.

Proton rapidity density distributions have been analysed in two contexts. The absolute rapidity loss of protons increases in this energy range, while the relative value remains constant, as is seen over three orders of magnitude in energy. This suggests that there is a significant amount of energy deposited in the collision zone and high baryon densities are achieved. However, the proton rapidity distributions exhibit an elongation which suggests that they retain some fraction of their initial longitudinal momenta, and/or that a substantial explosive collective behaviour emerges along the collision axis. The fact that the pion distributions can also be described with a source including the same magnitude of longitudinal flow as the protons supports the conclusion that the nuclear fireball produced in these heavy ion collisions explodes along the beam axis with a substantial hydrodynamical velocity.

Appendix A

$\langle dE/dx \rangle$ Shape Parameterization

The asymmetry in the shape of the $\langle dE/dx \rangle$ distribution for a single particle type is the result of the truncation method used to determine the mean value for a given track (see Chapter 3) and averaging over N_{hits} in filling the distributions. The truncation method introduced two effects in the $\langle dE/dx \rangle$. A fixed percentage truncation applied to distributions with different numbers of samples produces the asymmetric high-dE shoulder and causes the mean value to fluctuate. For future TPC experiments, it should be noted that in order to minimize distortions, the truncation percentage must be chosen such that the variation in the mean *and* the shoulder are minimized. Recently, the STAR experiment has adopted this type of $\langle dE/dx \rangle$ approach.[STAR00]

Since the $\langle dE/dx \rangle$ resolution depends on N_{hits}, averaging over this quantity also distorts the final distribution. The number of particles of a given N_{hits} in a given

momentum window varies, so even if the underlying distributions were themselves Gaussian, peaked at the same mean value, the superposition of multiple Gaussians of varying heights and widths produces a non-Gaussian final distribution. The trade-off between minimizing the distortion by cutting the distributions into N_{hits} bins and the loss of statistics in certain regions of the phase-space necessitated a parameterization of the N_{hits}-integrated, distorted distributions.

As described in Chapter 4, a two-Gaussian model was selected to approximate the observed distributions.

$$N_{\pi^-} = A \left[e^{-0.5 \left(\frac{x - <x>}{\sigma} \right)^2} + \alpha e^{-0.5 \left(\frac{x - \epsilon <x>}{\rho \sigma} \right)^2} \right] \tag{A-1}$$

The four parameters, σ, the main Gaussian width, ϵ, the ratio of the means of the two Gaussians, α, the ratio of their amplitudes, and ρ, the ratio of their widths were determined for each (m_t-m_0,y) bin through an extensive and iterative study of the negative particle distributions. The pion parameters were obtained from a study of the negative particles under the pion mass assumption, while the proton parameters were obtained from a study of the negative particles under the proton mass assumption. Two-Gaussian fits of the $\langle dE/dx \rangle$ distributions for the first twenty m_t-m_0 bins ($0 < m_t$-$m_0 < 500$ MeV/c^2) at each rapidity bin were used to characterize the variation of the four parameters as a function of momentum. This limited range of m_t-m_0 was chosen to ensure the statistics were high enough to obtain reliable fits. The results were used in the final analysis, extrapolating to the full range of m_t-m_0,

to fix the shapes of the distributions, allowing only the yields, A, and the overall gain to vary.

Through each of the four passes of the study, the total yields of the kaons were fixed using the method described in Appendix C. During the first pass, all four shape parameters and the yields of π^-, e^- and correlated π^- were allowed to vary while the mean value of $\langle dE/dx \rangle$ was fixed by the Bethe-Bloch parameterization. An additional overall gain parameter (single multiplicative factor on the centroids) was also included. This accounts for the fact that the Bethe-Bloch parameters were optimized using tight cuts on N_{hits} and the fraction of observed hits, so the predicted means do not exactly match those for the data used in this final analysis.

In the first pass, ϵ and α were observed to covary with each other but did not depend on m_t-m_0 or rapidity. Therefore, in the second pass, at each rapidity slice, ϵ was held fixed to a weighted average of the fit values extracted from the m_t-m_0 bins with greater than 150 entries obtained in the first pass. The second pass was run to obtain the values of α for fixed ϵ. A similar weighted average for α was computed after the second pass. Final fixed values of ϵ and α for each beam energy and particle of interest were then obtained by averaging their variation with rapidity. These were fixed inputs for the third pass of the shape study. Table A.1 lists the values of ϵ and α obtained for both pions and protons at each beam energy.

From the results of the third pass, it was concluded that the width parameters,

E_{beam}	$\pi\ \alpha$	$\pi\ \epsilon$	$p\ \alpha$	$p\ \epsilon$
2 AGeV	0.2622	1.2115	0.3394	1.1904
4 AGeV	0.2391	1.2120	0.2047	1.2133
6 AGeV	0.2725	1.1883	0.3108	1.1755
8 AGeV	0.2781	1.2127	0.3112	1.1833

Table A.1: Nominal shape parameters, ϵ and α for pion and proton candidates at each beam energy, used to fix the $\langle dE/dx \rangle$ distribution fits. The m_t-m_0 dependent parameters, σ and ρ, are shown in Figures A.1 and A.2.

σ and ρ, exhibit weak dependence on m_t-m_0 over most of momentum space, but a strong dependence on the rapidity slice in question. A simultaneous study of the N_{hits} distributions as a function of m_t-m_0 and rapidity supports this observation. The mean number of hits, $\langle N_{hits} \rangle$, increases significantly as a function of rapidity from backward to forward bins, but changes more slowly as a function of m_t-m_0. The asymmetry as a function of center of momentum rapidity is due to the Lorentz boost from the lab frame to the center of momentum frame. Only particles with high momentum in the z-direction are capable of traversing the entire volume of the TPC and acquiring the maximum number of hits. Since the $\langle dE/dx \rangle$ resolution depends on N_{hits}, (Equation 3.4), the $\langle dE/dx \rangle$ distributions should be narrower at forward rapidities, as is observed. However, at the most backward rapidities, as the m_t-m_0 increases, the proton $\langle dE/dx \rangle$ distributions become broader than the pion $\langle dE/dx \rangle$ distributions. This occurs where the pion and proton $\langle dE/dx \rangle$ are still well-separated. The N_{hits} distributions for these (m_t-m_0,y) bins exhibit two distinct bumps at different mean values, therefore, the widths of their $\langle dE/dx \rangle$ distributions should be

different. In order to account for the broadening of the proton $\langle dE/dx \rangle$ distributions, an additional multiplicative parameter was applied to the proton widths in the final yield fits to better characterize the measured proton distributions. The need for the additional parameter occurs at different rapidities for the different particle types and beam energies, due to the variation in their Lorentz boosts to the center of momentum. For example, at 2 AGeV, for the proton fits, all rapidity bins backward of mid-rapidity require the additional parameter. For the 4 AGeV protons, the parameter is included starting from the fourth bin backward of mid-rapidity, at 6 AGeV, from approximately the seventh bin backward and at 8 AGeV from the tenth bin and backward. In the worst cases, the proton distributions are 50% wider than the pion distributions for a given (m_t-m_0,y) bin.

Since there is also some covariance between ρ and σ, for the fourth and final pass, ρ was fixed to the m_t-m_0-averaged quantities plotted as a function of rapidity in the bottom panels of Figures A.1 and A.2. Due to the limited statistics at very forward and backward rapidities, reliable estimates of the shape parameters here are difficult. These regions must be extrapolated using some knowledge of the detector's boundaries. The minimum at forward rapidities in the protons is constrained by the predicted 7% resolution of Equation 3.4 for the ideal case of 128 samples on every track. Saturation at backward rapidities worked well to describe the pion distribution widths under both the pion and proton mass assumptions, but as was indicated in

the preceding paragraph, an additional free-floating multiplicative factor was needed in certain cases to accurately describe the proton widths.

The top panels of Figures A.1 and A.2 show the results for the m_t-m_0-averaged σ as a function of rapidity obtained from the fourth pass at each beam energy. These parameters, combined with those in Table A.1 define the baseline $\langle dE/dx \rangle$ distribution shapes of pion and proton candidates at each beam energy over all of momentum space studied for this dissertation.

Pion Shape Parameters
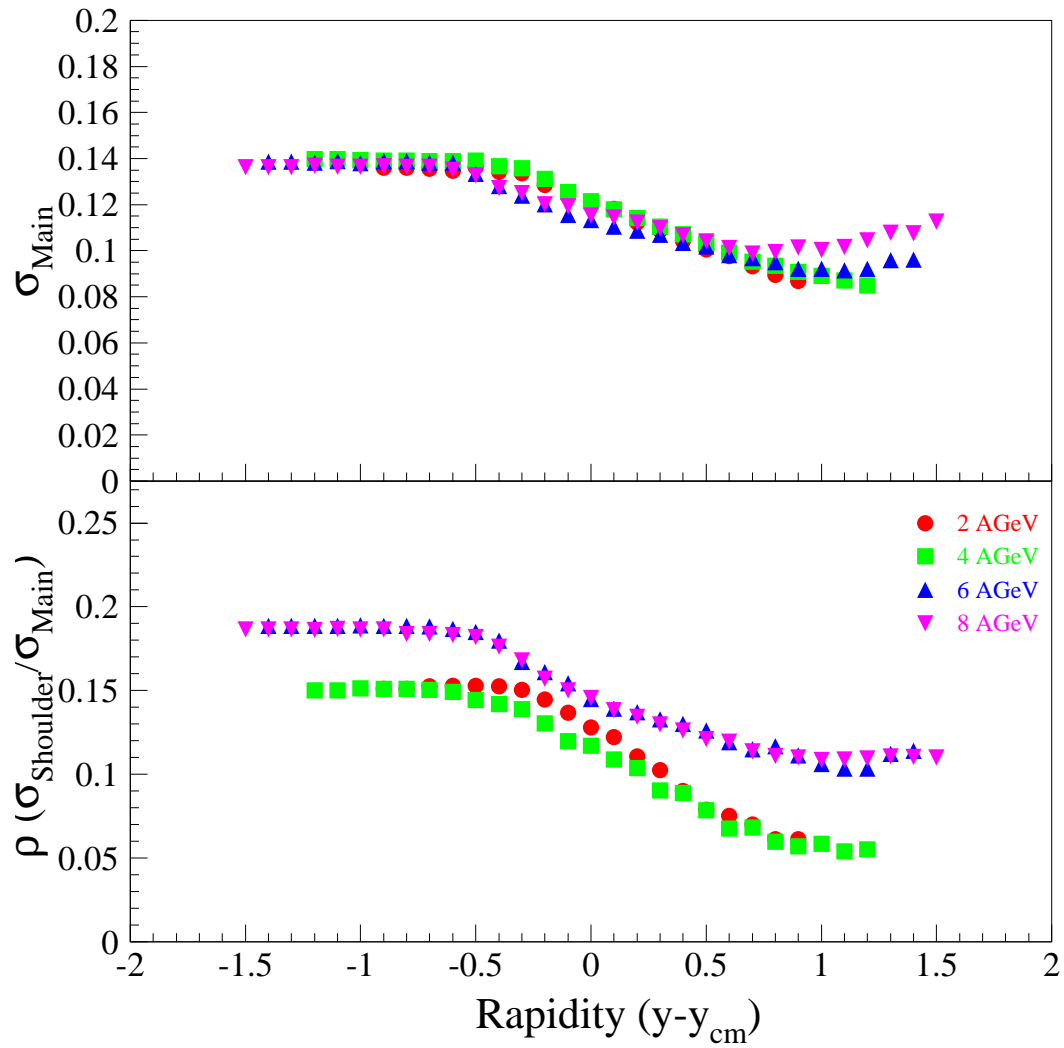
Figure A.1: σ and ρ from Equation A-1 as a function of rapidity for pion candidates at 2,4,6 and 8 AGeV.
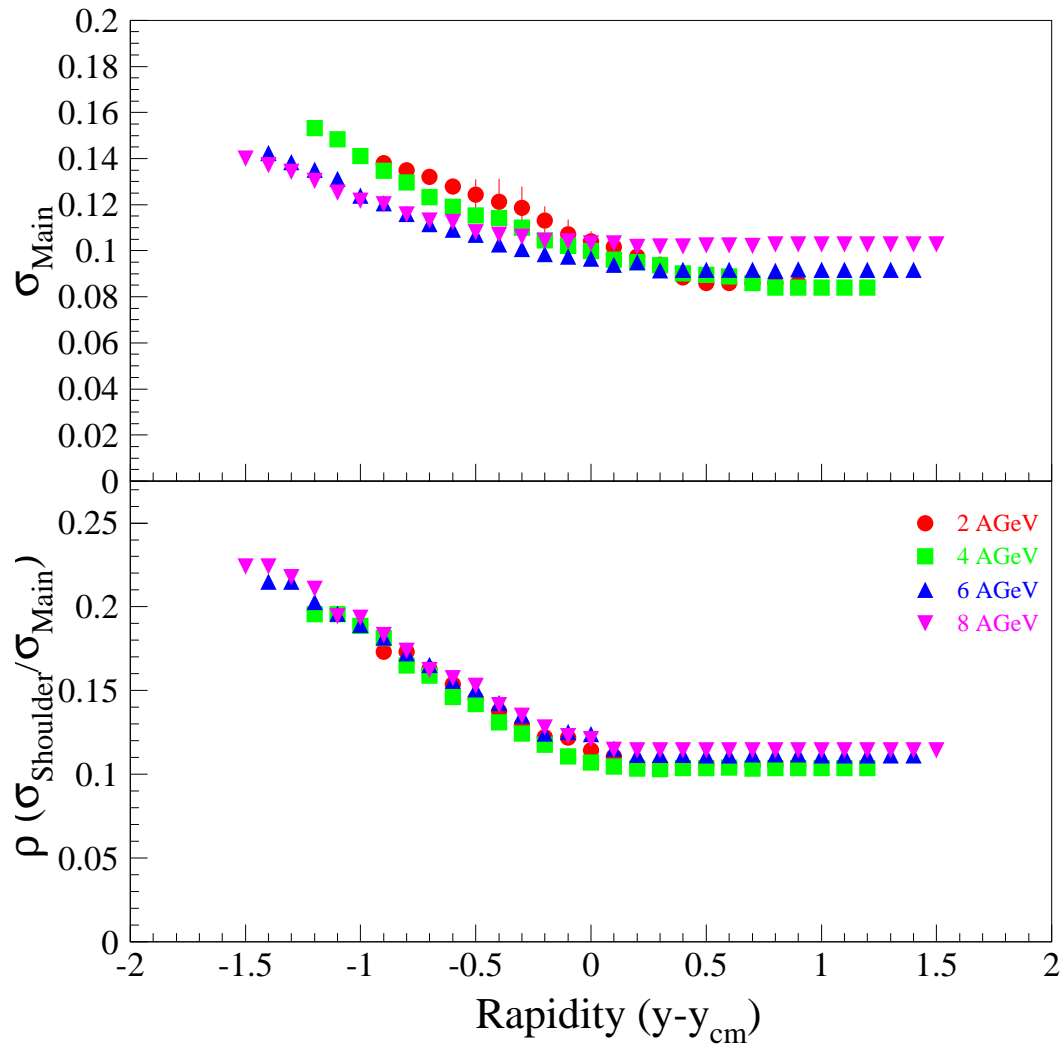
Figure A.2: σ and ρ from Equation A-1 as a function of rapidity for proton candidates at 2,4,6 and 8 AGeV.

Appendix B

Probabilistic Particle Identification (UCDPID)

The UCDPID routine was developed to provide the E895 Collaboration with a universal and reliable method of evaluating particle identification in secondary analyses. The basic philosophy of this approach to particle identification is to utilize the information about the well-identified particle species (such as the π^-) to help identify the other species. The EOS TPC's ability to measure $\langle dE/dx \rangle$ with a resolution ($\equiv \sigma$) of approximately 7% and its excellent momentum tracking make this possible.

The Bethe-Bloch model of energy loss is applied by individually fitting $\langle dE/dx \rangle$ distributions for the mean value as a function of graduated rigidity slices (narrower in the $1/\beta$ region, widening as the bands flatten out; from 0 to 15 GeV/c). Transforming

the rigidity to $\beta\gamma$, the observed mean value of $\langle dE/dx \rangle$ may be used to obtain the parameterized Bethe-Bloch prediction, Equation 4.4. The data used for the UCDPID analysis were cut on three track quality variables. Tracks with DCA > 2.5 cm, fewer than 50 hits, and less than 50% of their expected hits compared with the number of observed hits were rejected. The resulting Bethe-Bloch curves (Figures B.2, B.3, B.4, B.5) were fit with the Scott parameterization (Equation 4.4). A comparison of the prediction of the Scott parameterization with the measured mean values as a function of $\beta\gamma$ is shown in Figure B.1. The mean values extracted for each particle type in a given slice are plotted for each beam energy. The deviations, which are less than 5% everywhere, are worse for particles with smaller statistics. There is a slight (amplitude $\approx 2.5\%$) systematic oscillation for $\beta\gamma \leq 1.0$.

Particle types in this method include pions (both charged species), some kaons, protons, and deuterons. Positive species used are from the rigidity range p=0-1 GeV/c (30 rigidity slices) while the negative particle species are from the range p=0-15 GeV/c (80 rigidity slices). The particles identified with the resulting parameterization include the above-listed as well as correlated pions, correlated protons, (pairs of particles with nearly the same momenta that are nearby in space which ionize with twice the signal of a single particle), tritons and helions. Electron and positron $\langle dE/dx \rangle$ values are fixed with a linear parameterization which reproduces the $\langle dE/dx \rangle$-rigidity trajectory observed by the E910 experiment (using the EOS TPC and a time-of-flight detector)
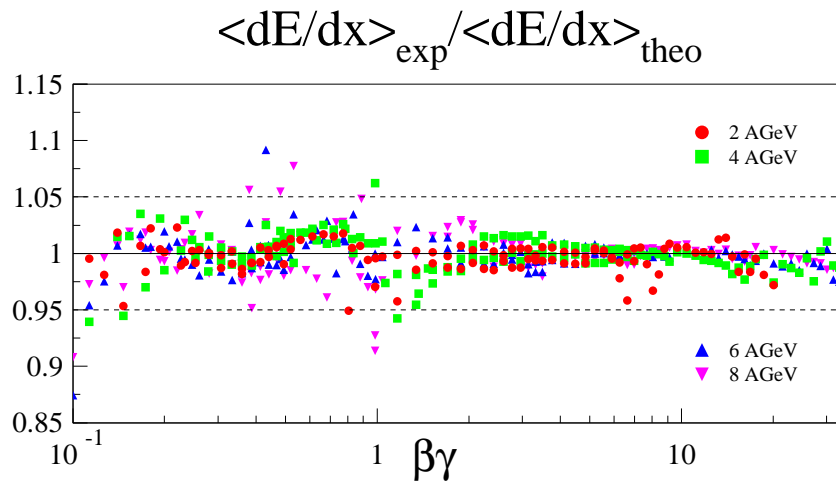
Figure B.1: Ratio of the observed mean value of $\langle dE/dx \rangle$ to the Scott parameterization (Equation 4.4) prediction as a function of $\beta\gamma$. The first set of Scott parameters is used for $\beta\gamma < 0.3$, while the second set of parameters applies for $\beta\gamma \geq 0.3$. The mean values extracted for each particle type in a given slice are plotted for each beam energy. The deviations are less than 5% everywhere.

in p-A collisions at the AGS.[Hiej97]

The Bethe-Bloch parameterization is used to extrapolate the individual particle bands into the region where they overlap. The $\langle dE/dx \rangle$ distributions are re-fit for the individual particle yields with Gaussian parameterizations for a given rigidity slice (all 80 slices, both positive and negative species). The non-Gaussian behaviour of the $\langle dE/dx \rangle$ distributions was ignored for this analysis.

The widths of the particle bands as a function of rigidity are shown in Figure B.6). In the fits for the relative amplitudes, the widths were fixed using a polynomial parameterization of the observed values. The positive pion yields were fixed in the
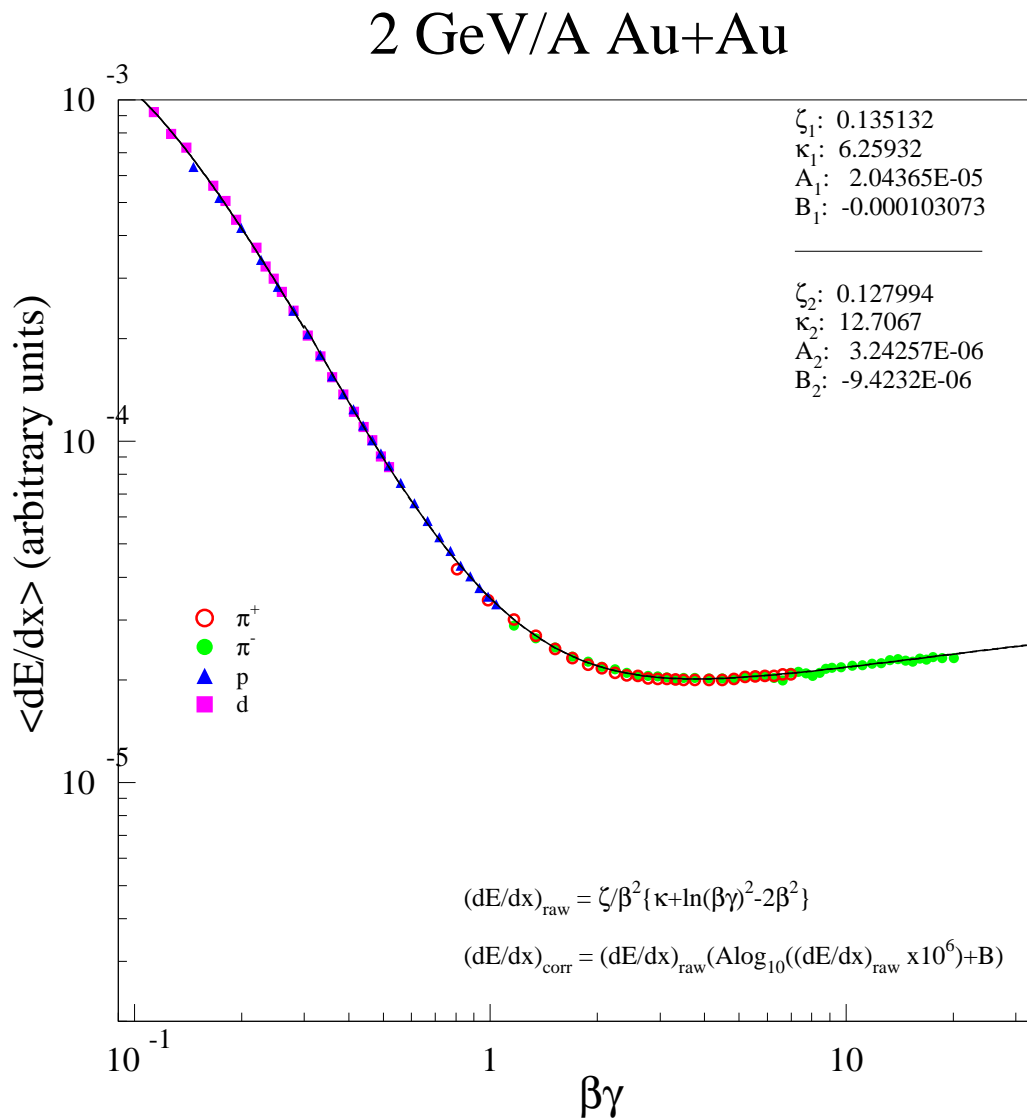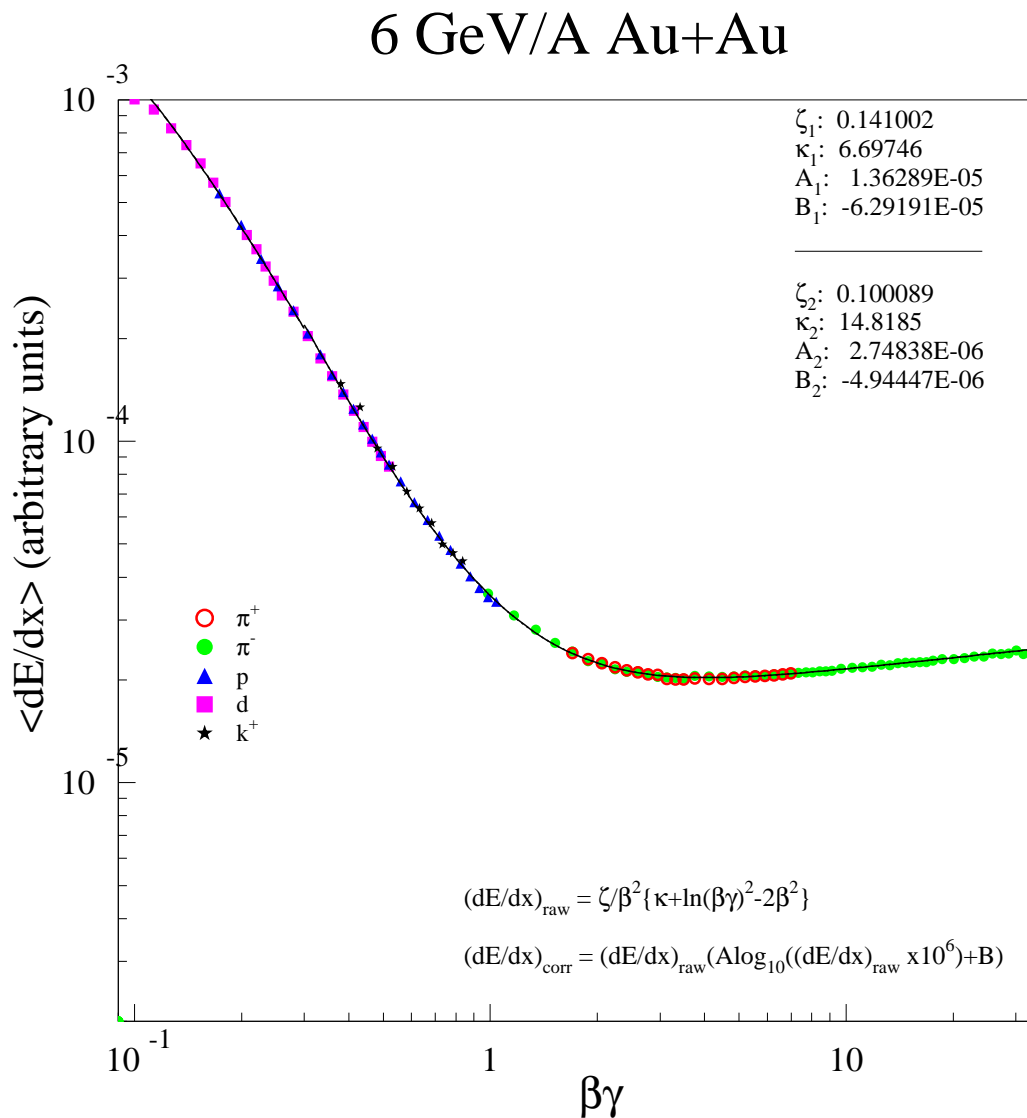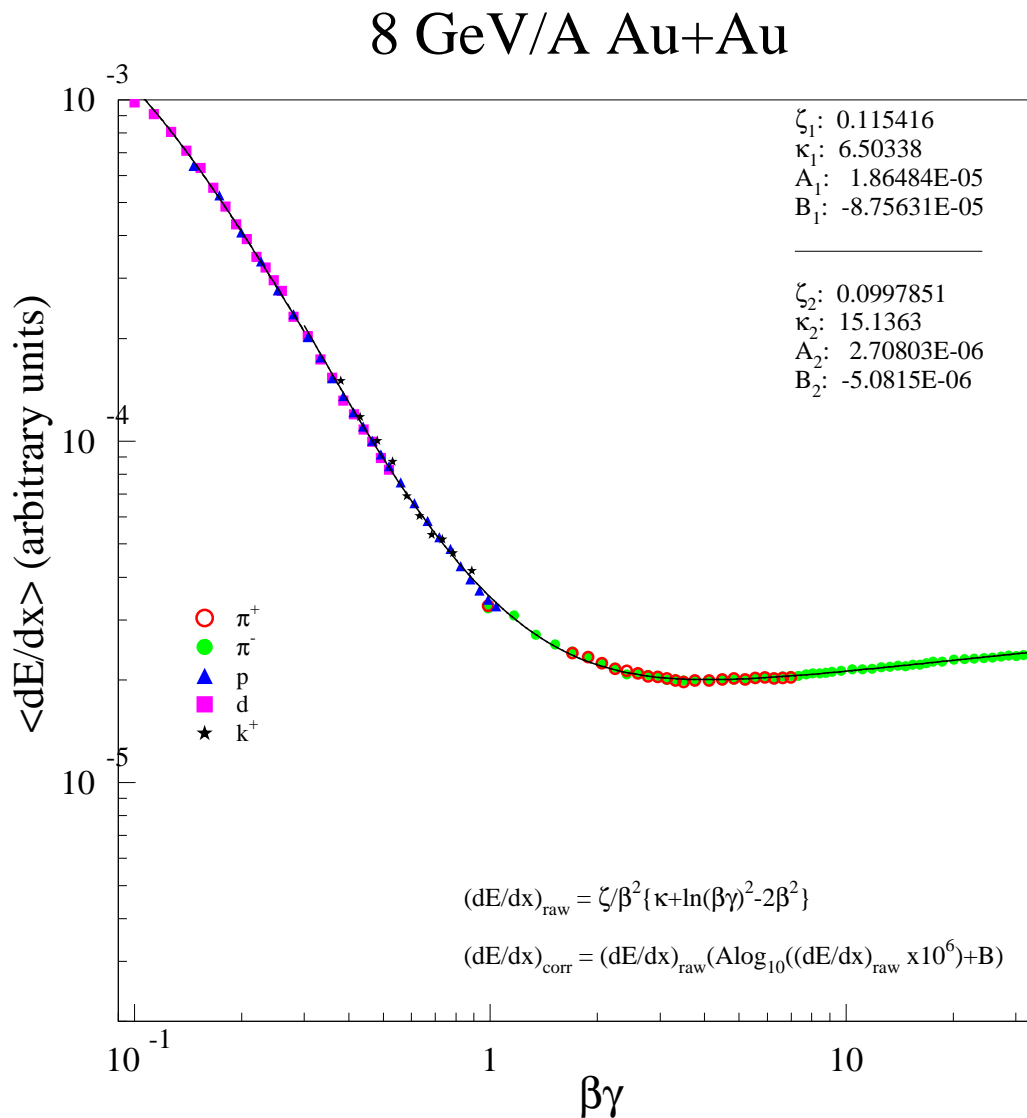
Figure B.2: Parameterized Bethe-Bloch function (Equation 4.4) of the average energy loss, fit to extracted mean values for pions (both positive and negative), kaons, protons and deuterons at 2 AGeV. The first set of Scott parameters is used for $\beta\gamma < 0.3$, while the second set of parameters applies for $\beta\gamma \geq 0.3$.
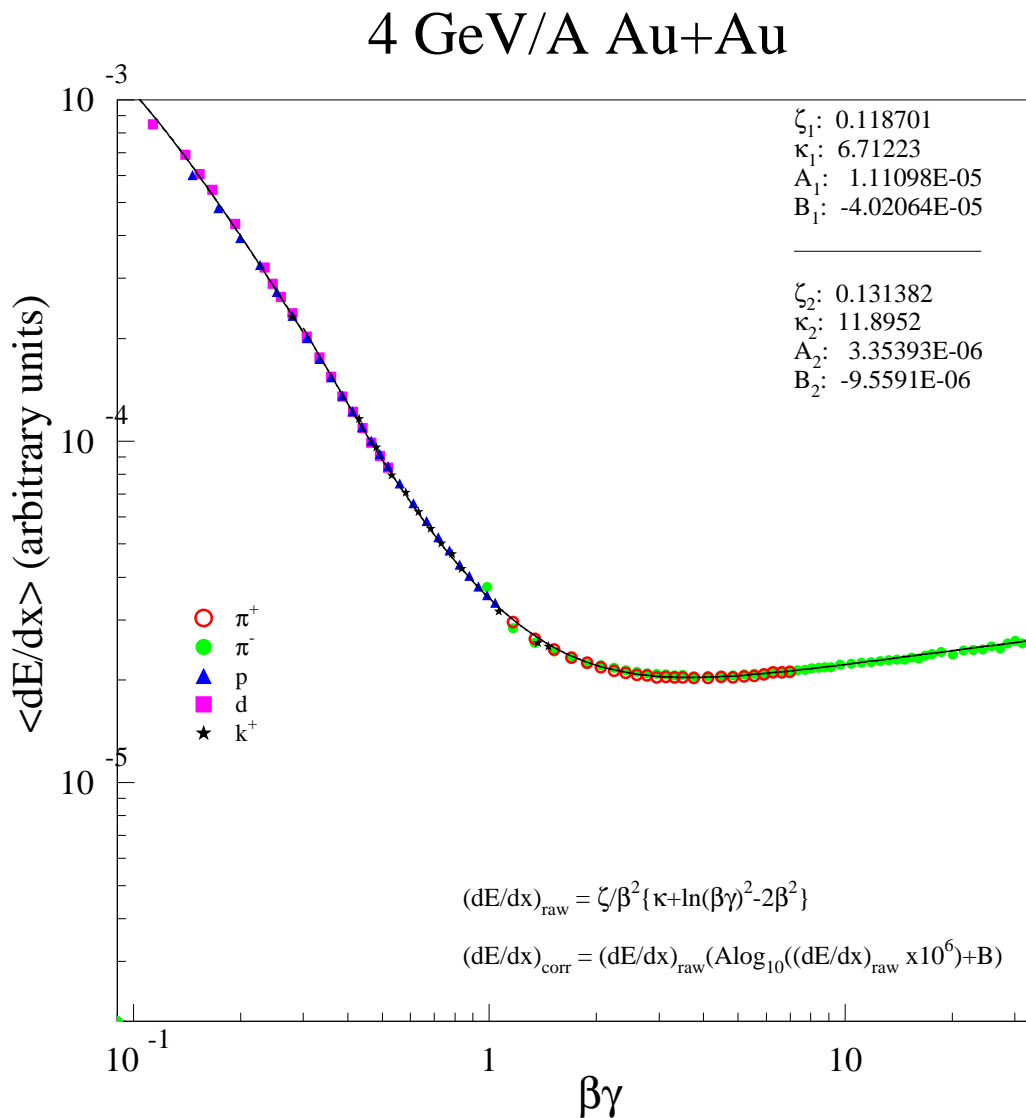
Figure B.3: Parameterized Bethe-Bloch function (Equation 4.4) of the average energy loss, fit to extracted mean values for pions (both positive and negative), kaons, protons and deuterons at 4 AGeV. The first set of Scott parameters is used for $\beta\gamma < 0.3$, while the second set of parameters applies for $\beta\gamma \geq 0.3$.

6 GeV/A Au+Au

ζ_1: 0.141002
κ_1: 6.69746
A_1: 1.36289E-05
B_1: -6.29191E-05

ζ_2: 0.100089
κ_2: 14.8185
A_2: 2.74838E-06
B_2: -4.94447E-06

$\langle dE/dx \rangle$ (arbitrary units)

○ π^+
● π^-
▲ p
■ d
★ k^+

$(dE/dx)_{raw} = \zeta/\beta^2\{\kappa+\ln(\beta\gamma)^2-2\beta^2\}$

$(dE/dx)_{corr} = (dE/dx)_{raw}(A\log_{10}((dE/dx)_{raw} \times 10^6)+B)$

$\beta\gamma$

Figure B.4: Parameterized Bethe-Bloch function (Equation 4.4) of the average energy loss, fit to extracted mean values for pions (both positive and negative), kaons, protons and deuterons at 6 AGeV. The first set of Scott parameters is used for $\beta\gamma < 0.3$, while the second set of parameters applies for $\beta\gamma \geq 0.3$.

Figure B.5: Parameterized Bethe-Bloch function (Equation 4.4) of the average energy loss, fit to extracted mean values for pions (both positive and negative), kaons, protons and deuterons at 8 AGeV. The first set of Scott parameters is used for $\beta\gamma < 0.3$, while the second set of parameters applies for $\beta\gamma \geq 0.3$.

final fits using a parameterization of the observed ratio of π^+/π^- as a function of rigidity (Figure B.7. The Gaussian amplitudes of each particle type as a function of rigidity are shown in Figures B.8, B.9, B.10, and B.11.

The mean $\langle dE/dx \rangle$, distribution width, and yield as a function of rigidity slice are combined into a parameter table which is called by a PID software analysis module. On a track-by-track basis, using the $\langle dE/dx \rangle$ and rigidity measured for the track, the three highest probability identities are computed from the tabulated information. These identities are stored along with the probability weighting for each assignment. Normalization is over all particle types (of a given charge) so the sum of the three saved weighting values is not necessarily exactly one. An example plot showing the most probable assignments for electrons, pions, kaons, protons, deuterons and tritons at 4 AGeV superposed on the full set of tracks is given in Figure B.12. Although only the most probable identification is shown, the user can select probability thresholds for each particle assignment.

\<dE/dx\> Distribution Widths
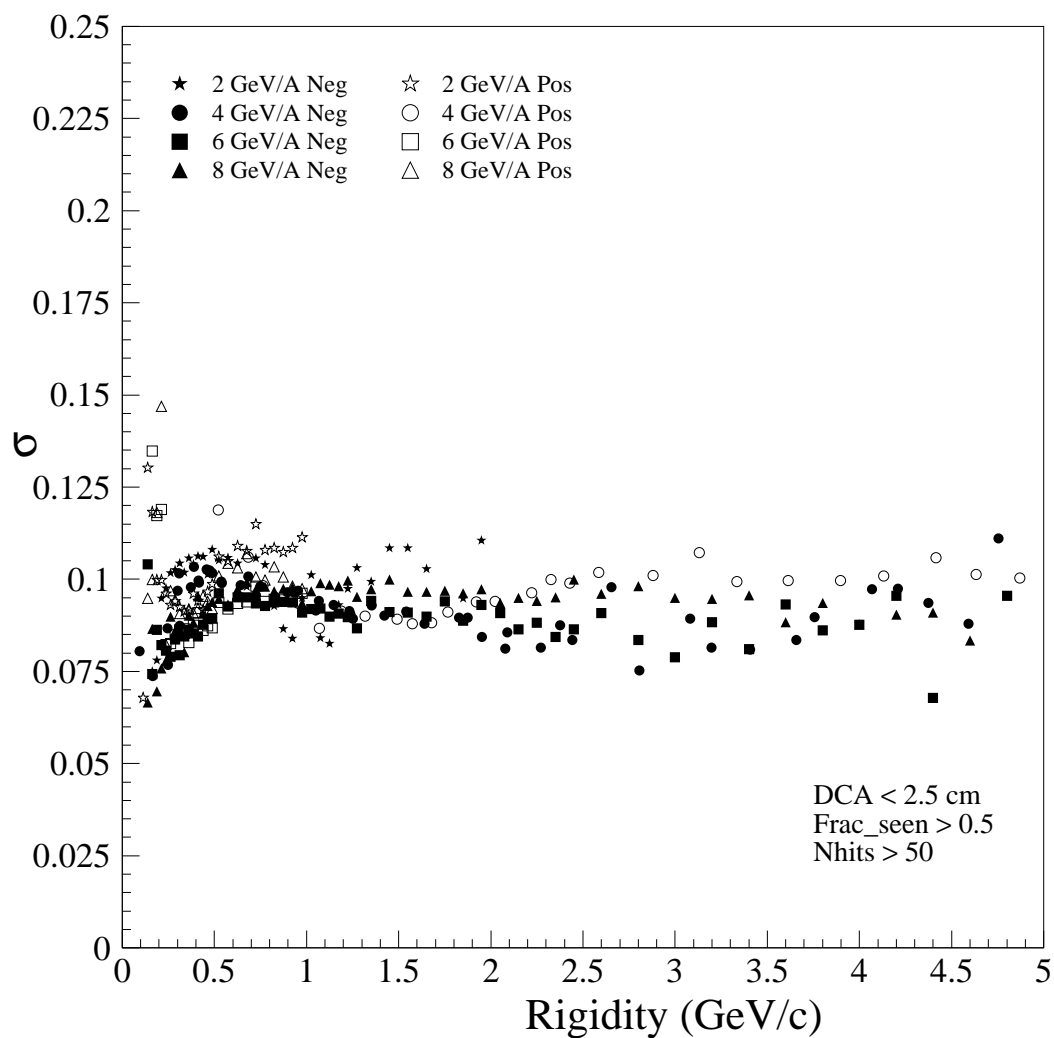
Figure B.6: ⟨dE/dx⟩ distribution widths as a function of rigidity for positive and negative particles at all energies.
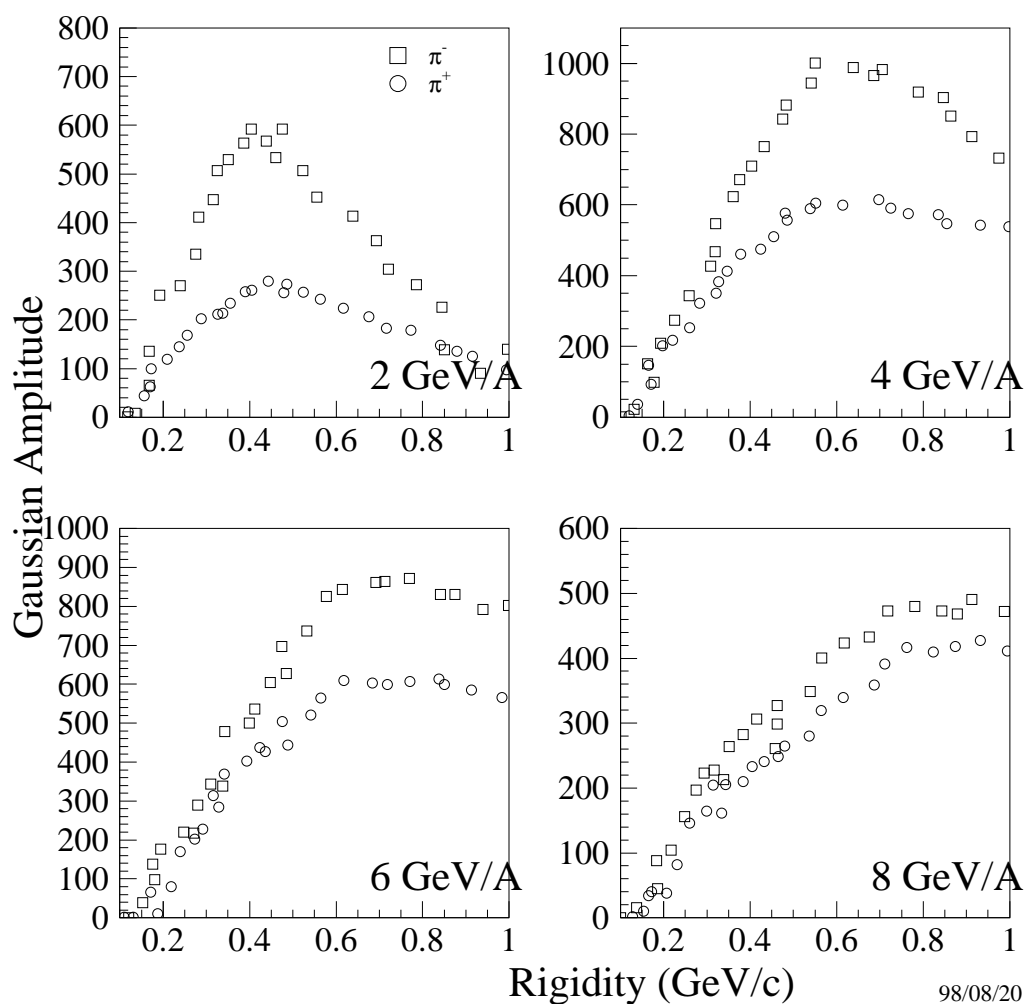
Figure B.7: Observed yields of π^+ and π^- from the UCDPID analysis as a function of rigidity ($r=p/Z$). A parameterization of their ratio was used to fix the positive pion yields in the region of confusion.
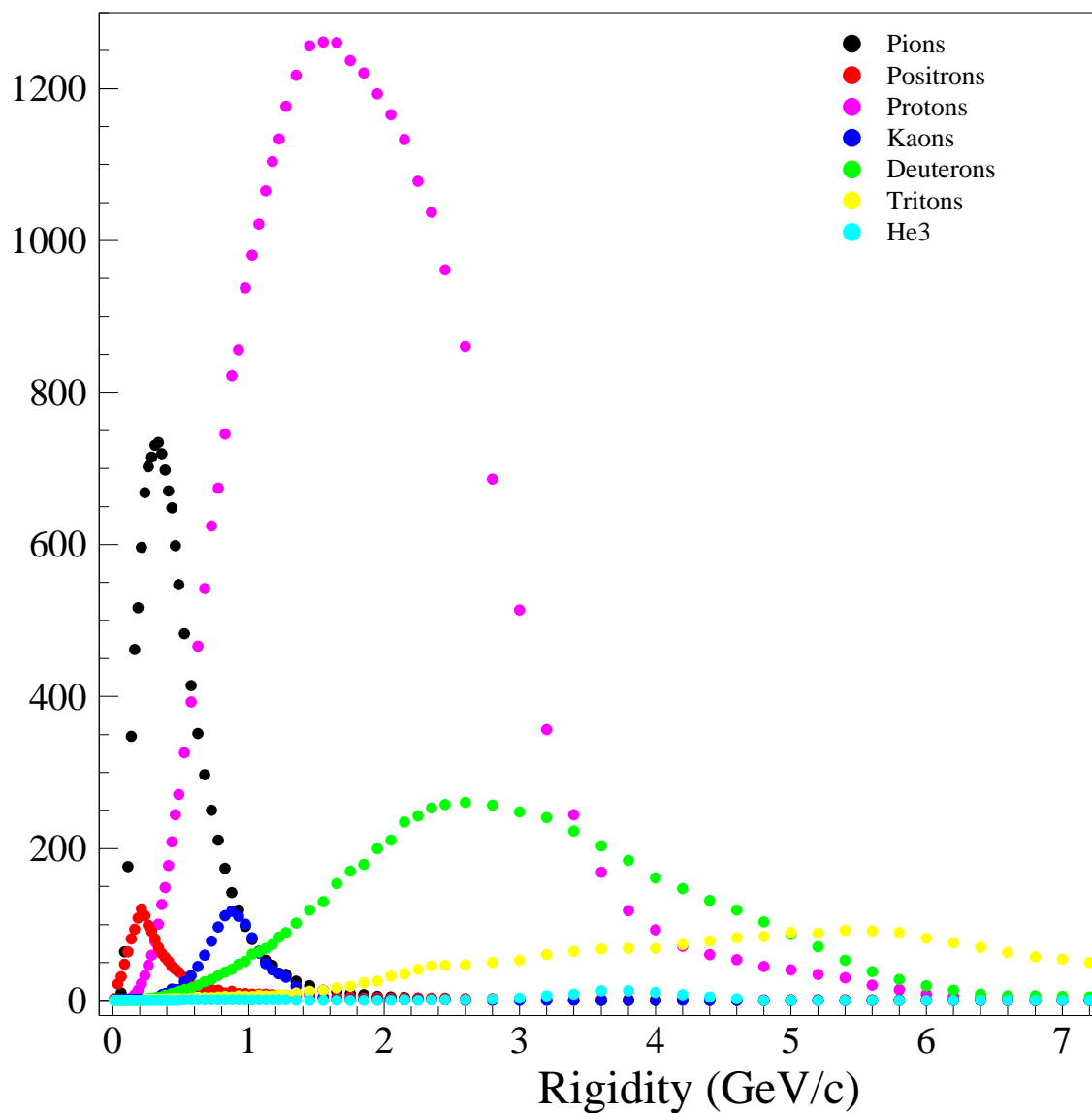
2 GeV Au+Au Amplitudes for Pid

Figure B.8: Amplitudes of all positive particles as a function of rigidity at 2 AGeV used by the UCDPID routine to assign probabilistic particle identification.

4 GeV Au+Au Amplitudes for Pid
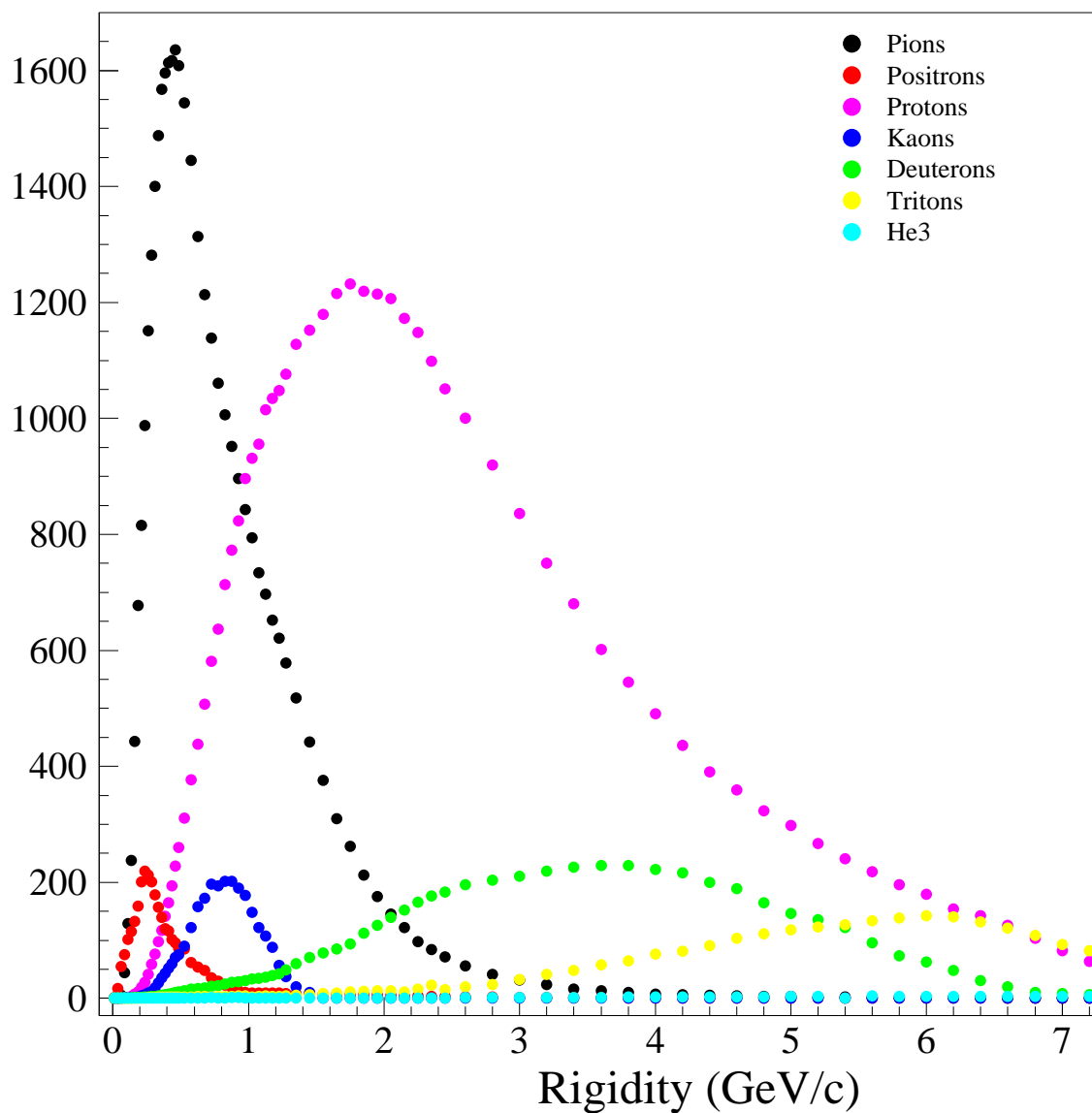
Figure B.9: Amplitudes of all positive particles as a function of rigidity at 4 AGeV used by the UCDPID routine to assign probabilistic particle identification.

6 GeV Au+Au Amplitudes for Pid
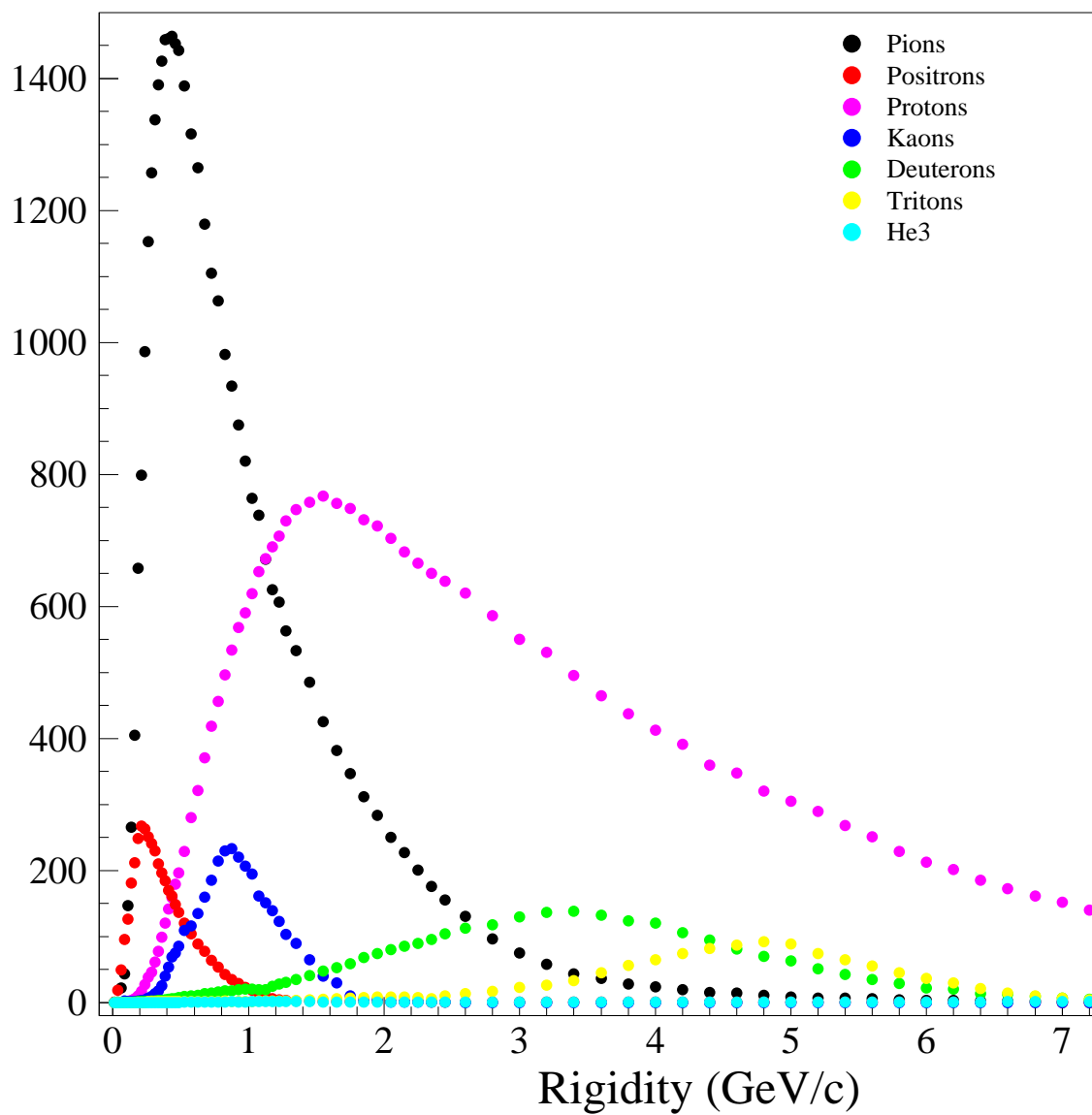
Figure B.10: Amplitudes of all positive particles as a function of rigidity at 6 AGeV used by the UCDPID routine to assign probabilistic particle identification.

8 GeV Au+Au Amplitudes for Pid
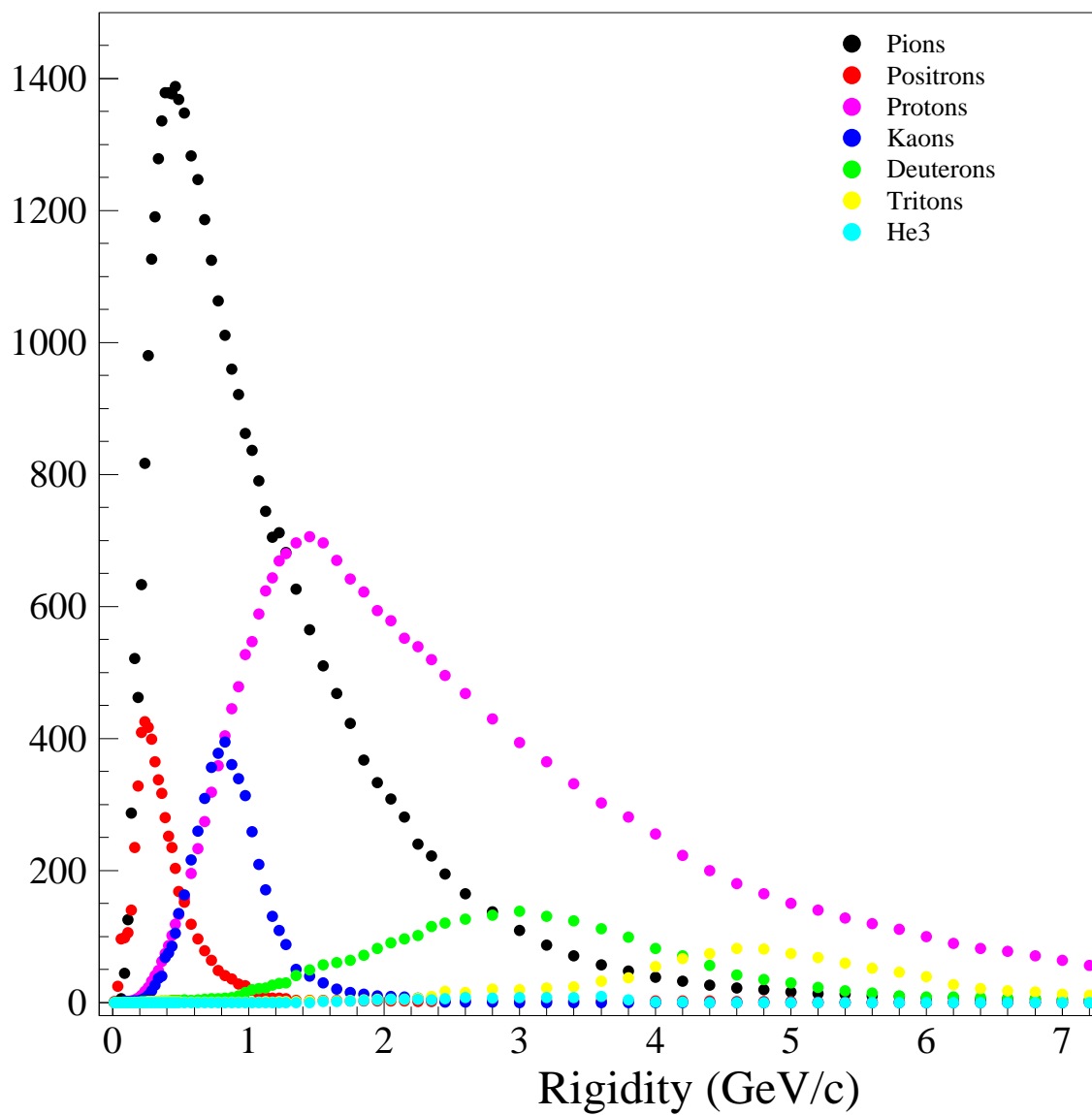
Figure B.11: Amplitudes of all positive particles as a function of rigidity at 8 AGeV used by the UCDPID routine to assign probabilistic particle identification.

4GeV Au+Au Most Probable

98/07/13 20.32
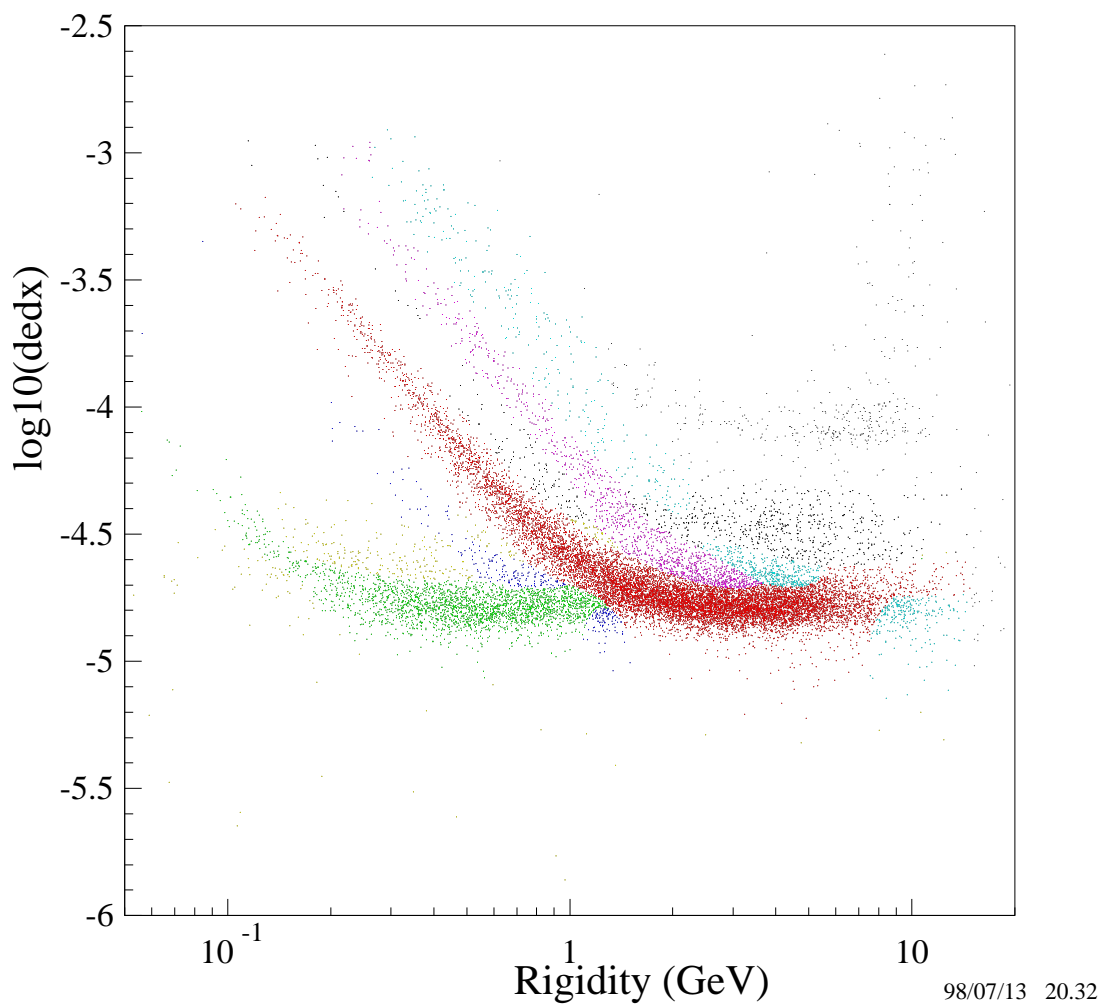
Figure B.12: Most probable identified particles, using the UCDPID routine. Positrons are shown in yellow, π^+ in green, K^+ in blue, protons in red, deuterons in magenta and tritons in light blue. The black points are tracks which are not identified with any of the listed particles.

Appendix C

Kaon Contamination

The kaons represent an important, but rather small fraction of the total number of observed particles in the collisions studied in this thesis. Their contribution is small enough to make them difficult to detect with a TPC over much of phase space, but large enough to be a nuisance for measuring other particle species. The goal is to be able to predict the number of kaons in a given (m_t-m_0,y) bin for any particle of interest mass assumption from the measured yields of kaons from E866/E917. The dN/dy and temperature parameters (Figures C.1, C.2, C.3 and C.4) reported by Dunlop[Dunl99] are used as a guide to compute the yield in a given (m_t-m_0,y) bin.[1] These raw yields are then combined with the E895 detection efficiency, scaled by the number of events used in the analysis, and corrected for the bin widths. A Gaussian

---

[1]The parameters were graphically extracted from figures in [Dunl99]. Since these parameters are a guide for removing contamination and are not intended for direct analysis, any differences between these values and the exact reported values should not be interpreted as significant.

parameterization of the dN/dy and the mathematical model used by E866/E917 to describe the m_t-m_0 distributions are

$$\frac{dN}{dy_k}(y_k - y_{cm}) = \frac{N_k}{\sigma\sqrt{2\pi}}e^{-\frac{1}{2}(\frac{y_k-y_{cm}}{\sigma_k})^2} \qquad \text{(C-1)}$$

$$\frac{1}{2\pi m_{t_k}}\frac{d^2N}{dm_{t_k}dy_k} = \frac{dN/dy_k(y_k - y_{cm})}{2\pi(m_kT_k + T_k^2)}e^{\frac{-(m_{t_k}-m_k)}{T_k}} \qquad \text{(C-2)}$$

The Jacobian to transform between the kaon (m_t-m_0,y) and, say, the pion (m_t-m_0,y), for pions and kaons of the same p_t and p_z, can be derived from the following relations:

$$p_{t_k} = p_{t_\pi}$$

$$m_{t_k}^2 = m_{t_\pi}^2 - m_\pi^2 + m_k^2$$

$$dm_{t_k} = \frac{m_{t_\pi}}{m_{t_k}}dm_{t_\pi} \qquad \text{(C-3)}$$

$$p_{z_k} = p_{z_\pi}$$

$$m_{t_k}\sinh(y_k - y_{cm}) = m_{t_\pi}\sinh(y_\pi - y_{cm})$$

$$m_{t_k}\cosh(y_k - y_{cm})dy_k = m_{t_\pi}\cosh(y_\pi - y_{cm})dy_\pi$$

$$dy_k = \frac{E_\pi}{E_k}dy_\pi \qquad \text{(C-4)}$$

The Jacobian factor is just the ratio of the energies of the two particles. There are 40 bins per unit of m_t-m_0 and 10 bins per unit of rapidity. The overall detection efficiency of pions and protons discussed in Chapter 6, denoted $\epsilon^{det}(m_t$-m_0,y$)_{particle}$,

must be applied to scale the total number of predicted kaons down to match the number expected to be observable by our detector in the given $(m_t\text{-}m_0, y)_{particle}$ window. Combining all of these factors, the total number of kaons in a given (pion mass assumption) $\langle dE/dx \rangle$ histogram can be expressed

$$\frac{\Delta^2 N}{\Delta m_{t_\pi} \Delta y_\pi} = \epsilon_\pi^{det} \frac{N_{events}}{400} 2\pi m_{t_\pi} \frac{E_\pi}{E_k} \frac{dN/dy_k(y_k - y_{cm})}{2\pi(m_k T_k + T_k^2)} e^{\frac{-(m_{t_k} - m_k)}{T_k}} \qquad \text{(C-5)}$$
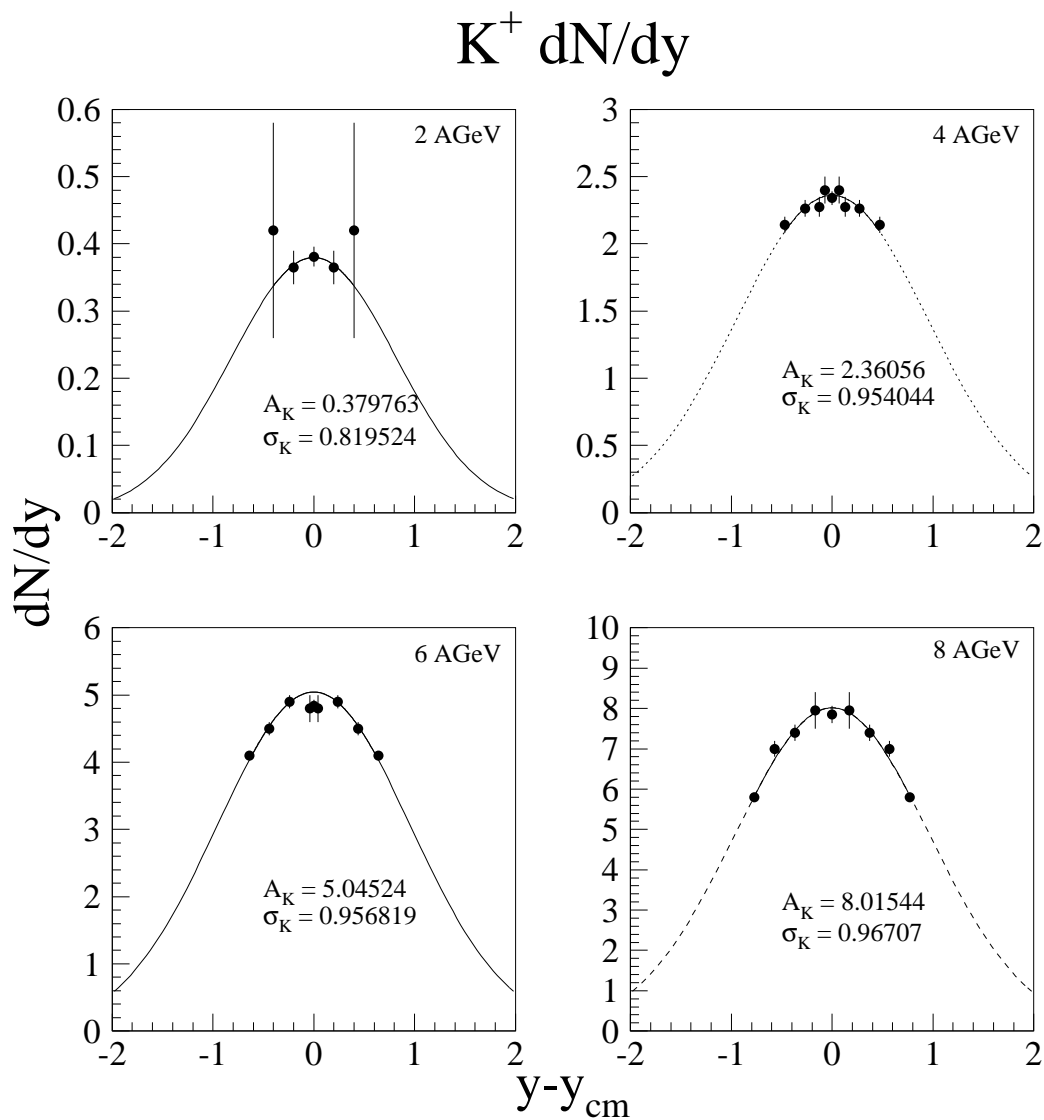
K$^+$ dN/dy

Figure C.1: K$^+$ dN/dy distributions adapted from E866/E917 measurements. [Dunl99]

K$^+$ Inverse Slopes
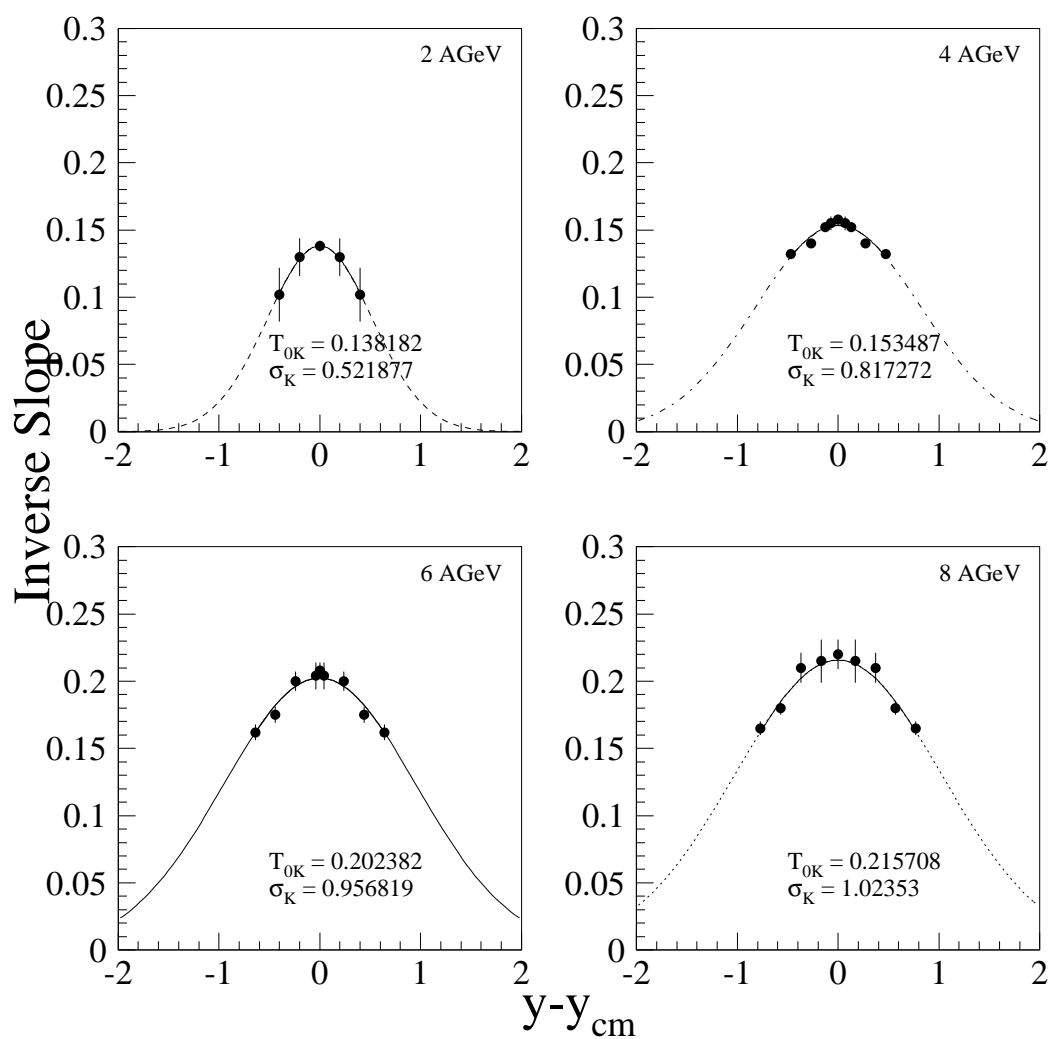
Figure C.2: K$^+$ Single Slope parameters as a function of rapidity adapted from E866/E917 measurements.[Dunl99]
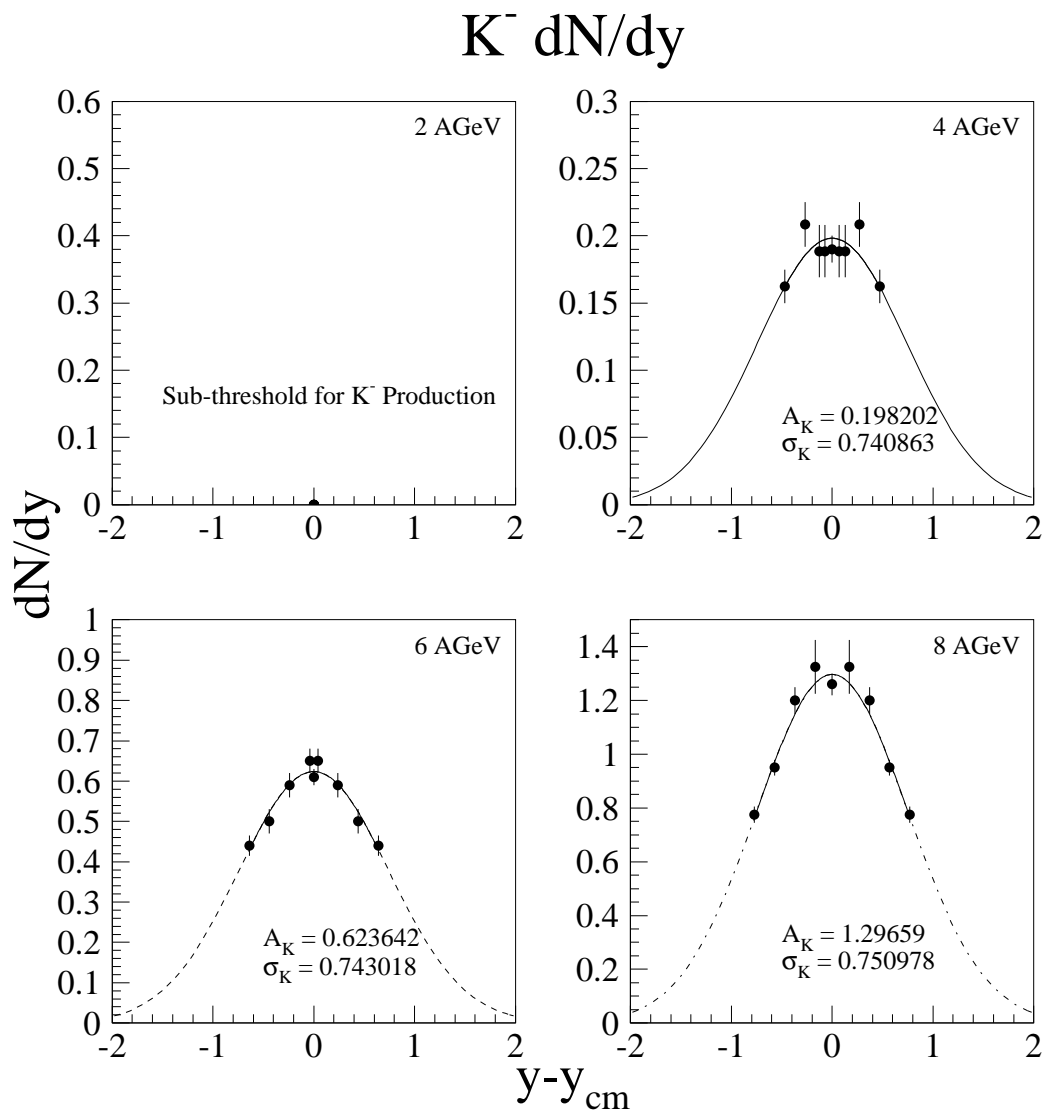
K⁻ dN/dy

Figure C.3: K⁻ dN/dy distributions adapted from E866/E917 measurements. [Dunl99]

K⁻ Inverse Slope
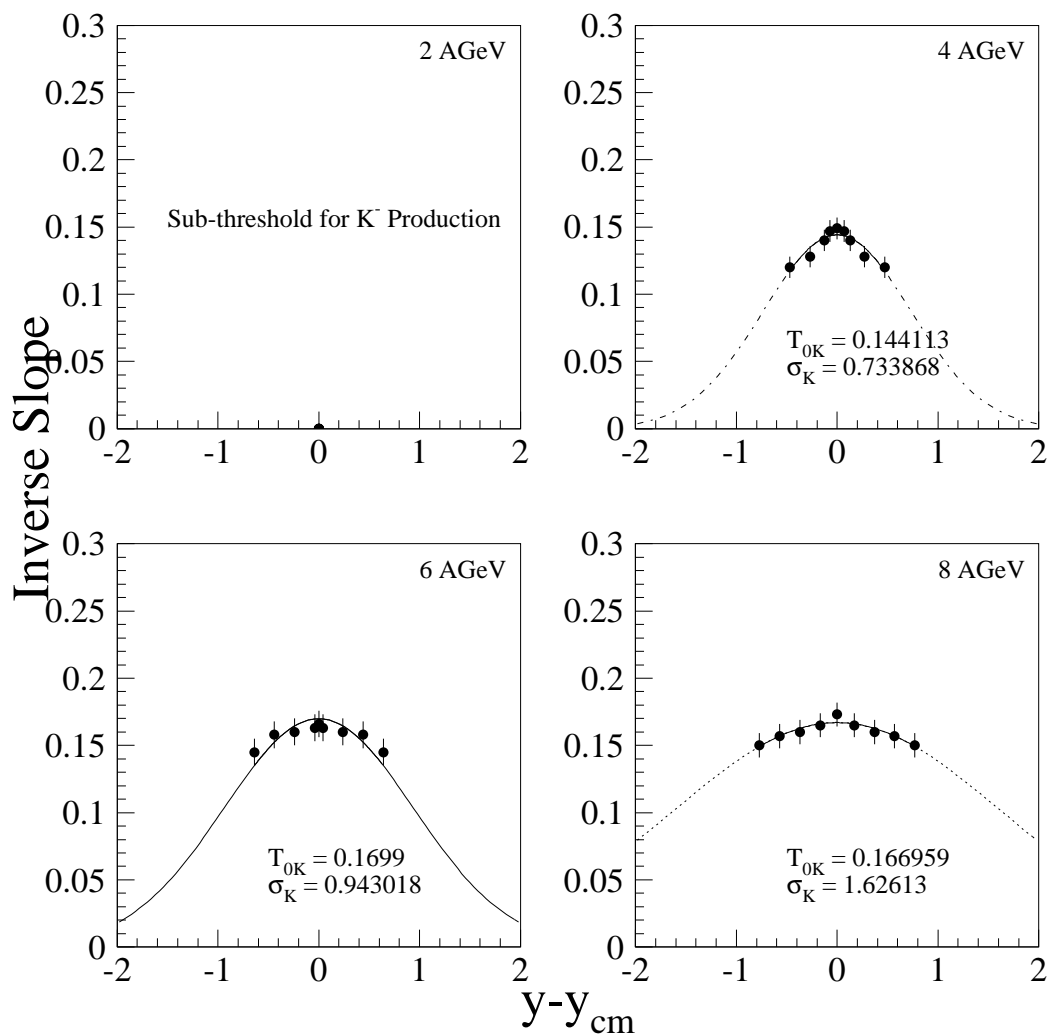
Figure C.4: K⁻ Single Slope parameters as a function of rapidity adapted from E866/E917 measurements.[Dunl99]

Appendix D

Correction Vectors

The complete detection efficiency corrections obtained from the loss-function (Eq. 6.6) fits are compiled in this appendix.

2 AGeV Pion Efficiency
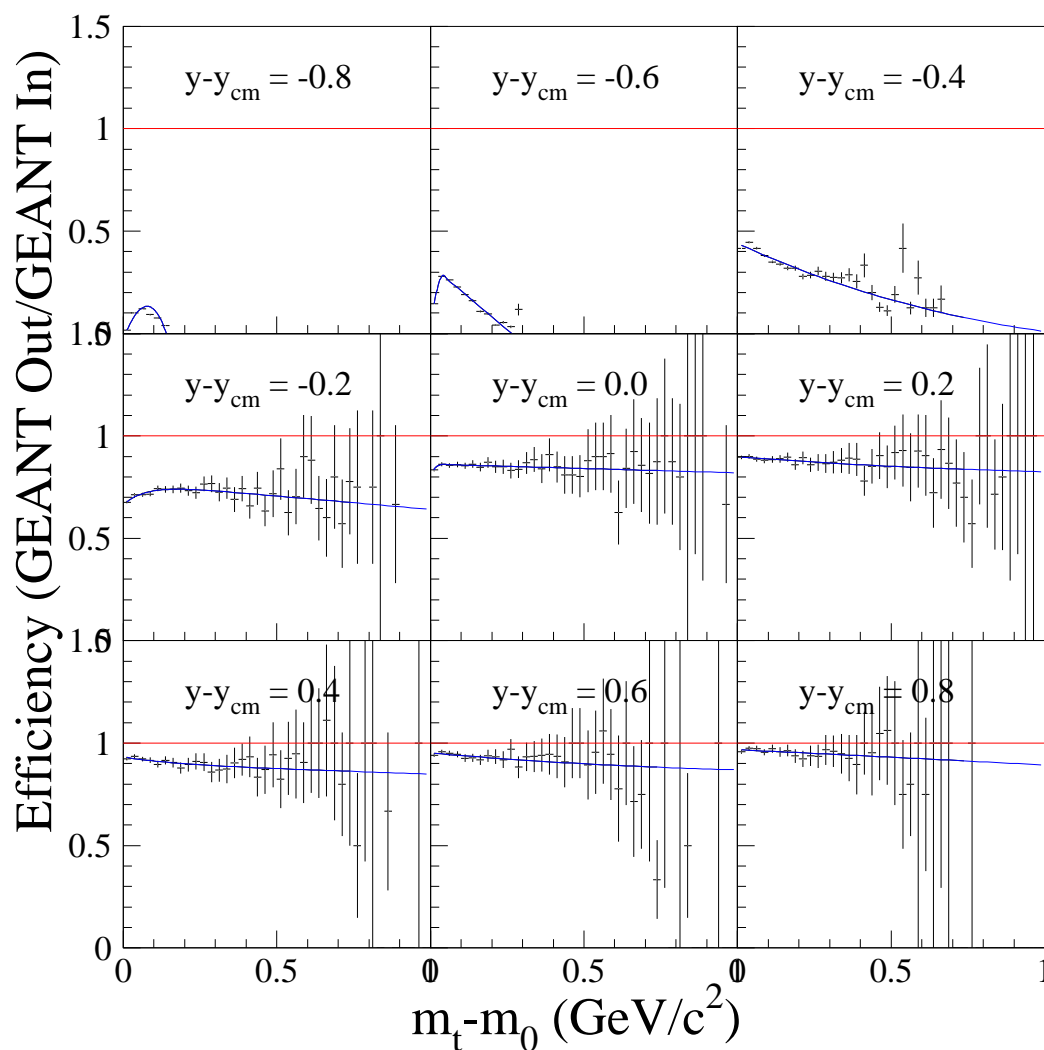
Figure D.1: 2 AGeV Pion Detection Efficiencies with Loss Function (Equation 6.6) fits at each embedded rapidity.
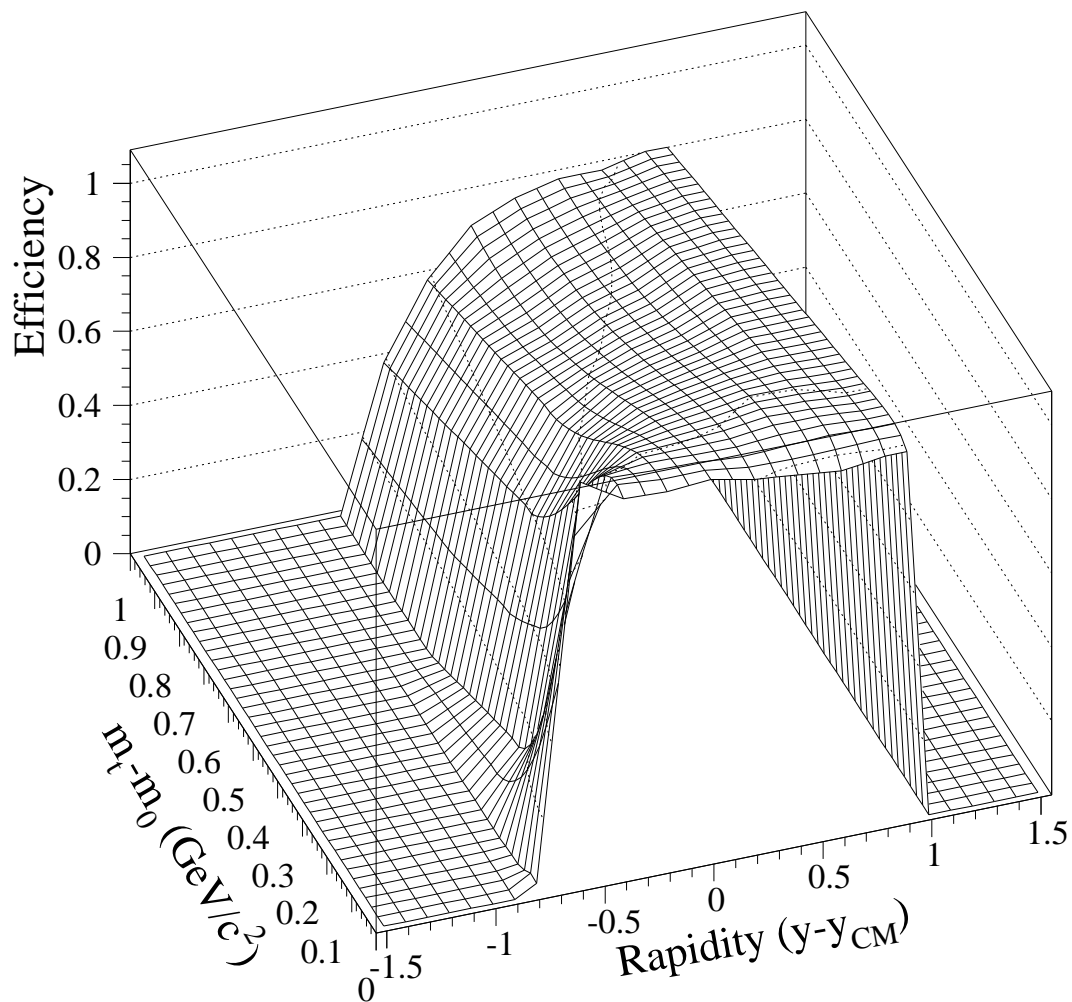
2 AGeV Pion Efficiency
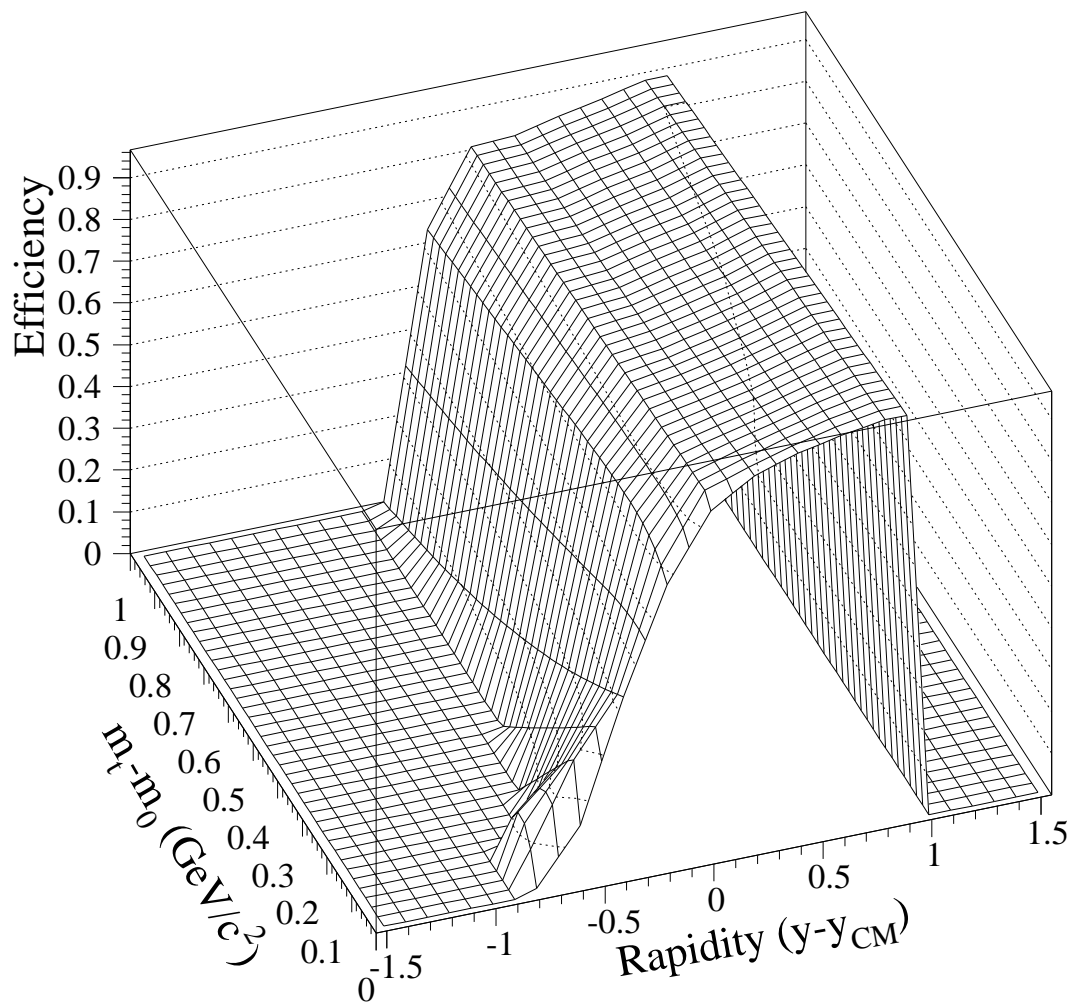
Figure D.2: 2 AGeV Pion Detection Efficiencies as a function of m_t-m_0 and rapidity.

2 AGeV Proton Efficiency
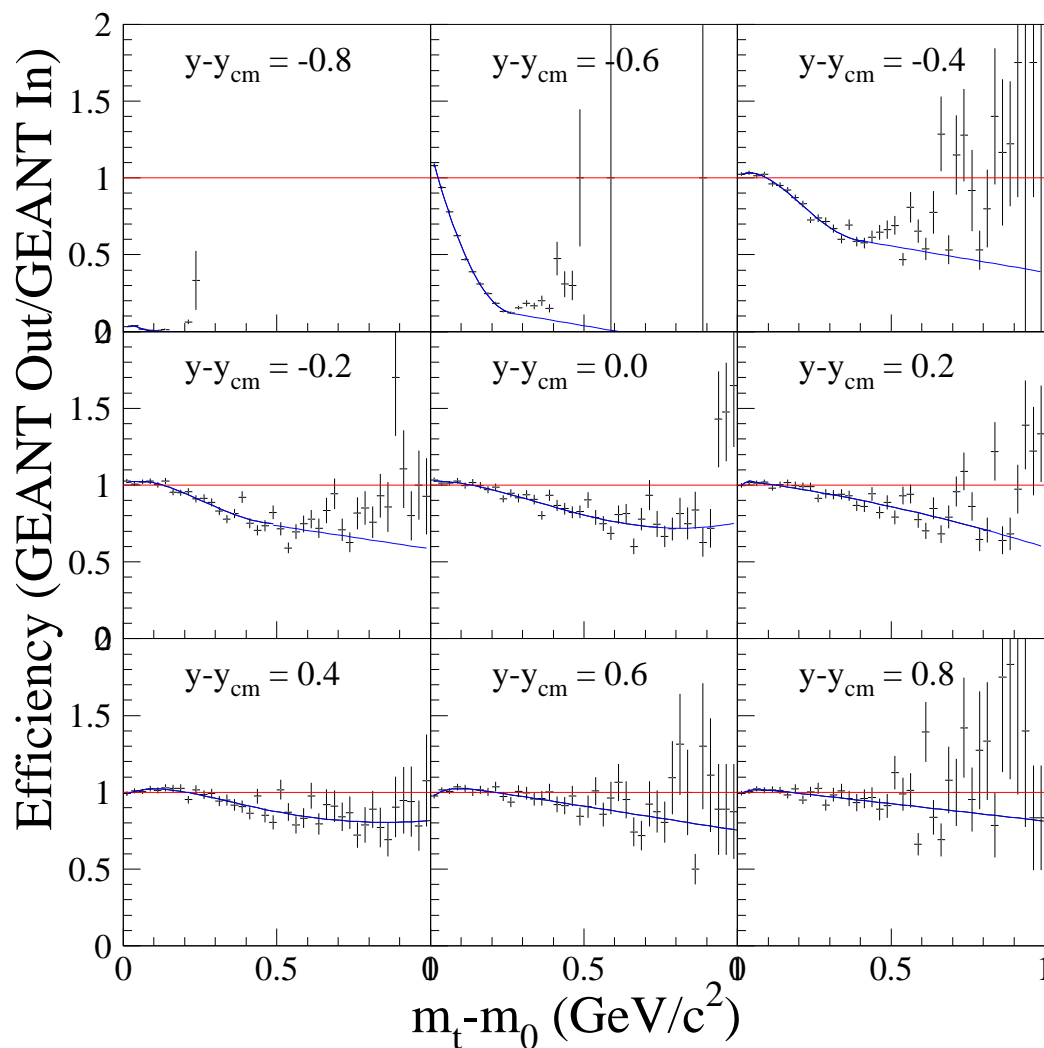
Figure D.3: 2 AGeV Proton Detection Efficiencies with Loss Function (Equation 6.6) fits at each embedded rapidity.

2 AGeV Proton Efficiency

Figure D.4: 2 AGeV Proton Detection Efficiencies as a function of m_t-m_0 and rapidity.
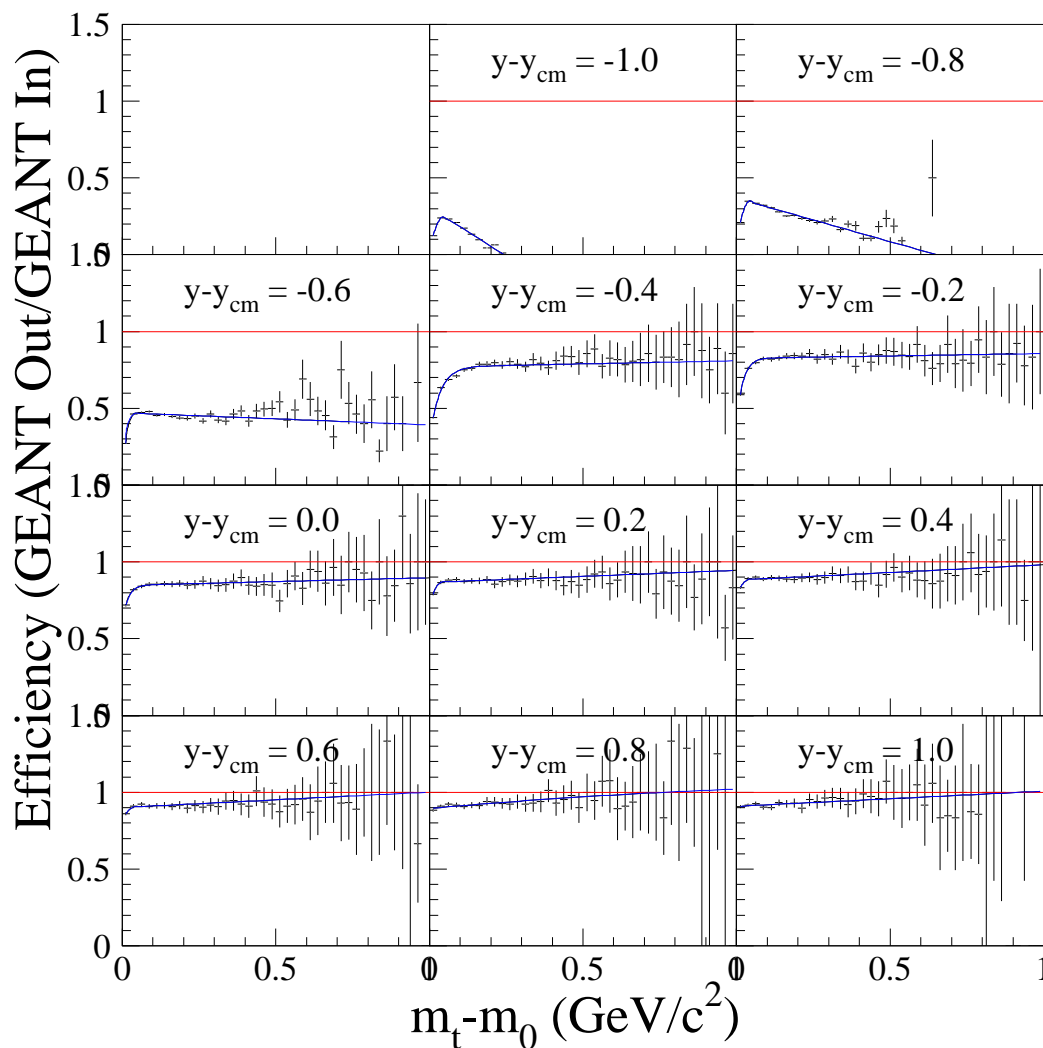
4 AGeV Pion Efficiency

Figure D.5: 4 AGeV Pion Detection Efficiencies with Loss Function (Equation 6.6) fits at each embedded rapidity.
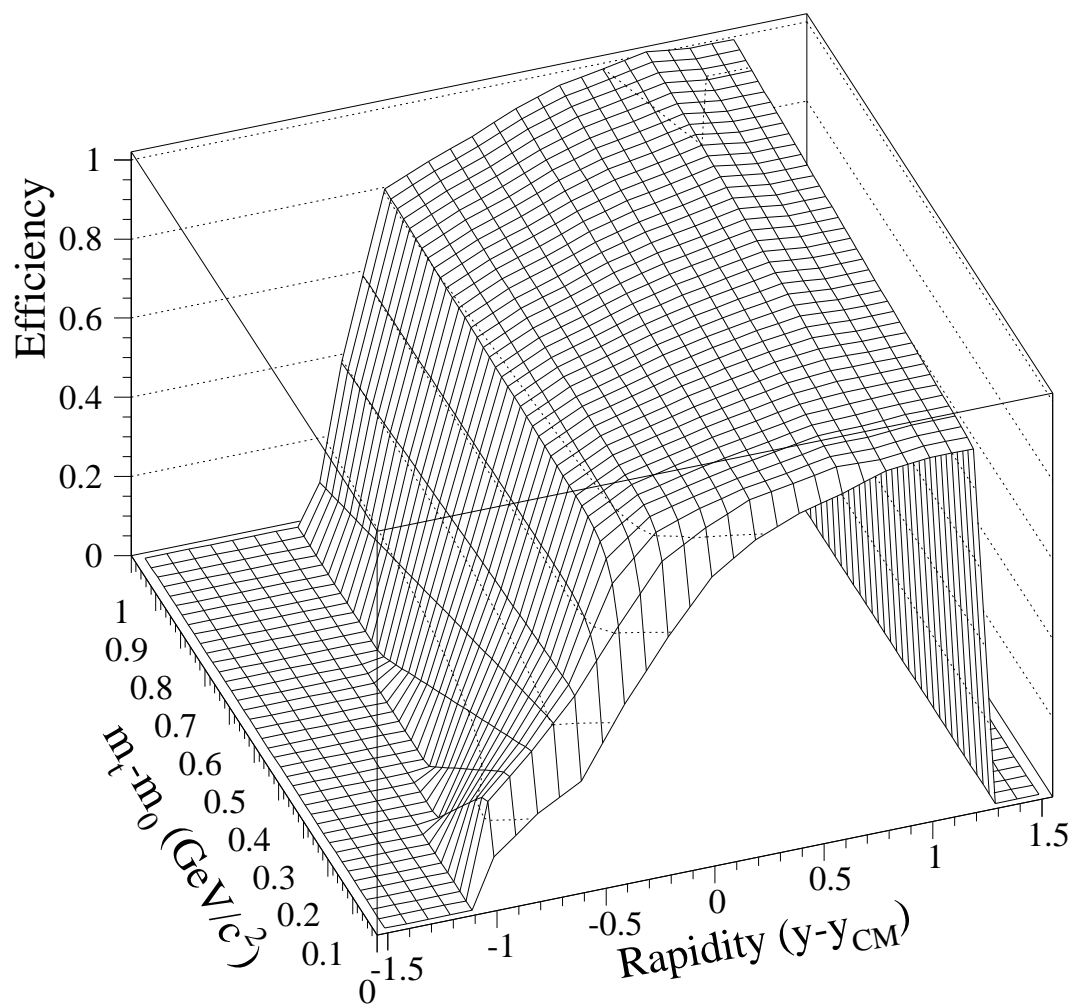
4 AGeV Pion Efficiency

Figure D.6: 4 AGeV Pion Detection Efficiencies as a function of m_t-m_0 and rapidity.

4 AGeV Proton Efficiency

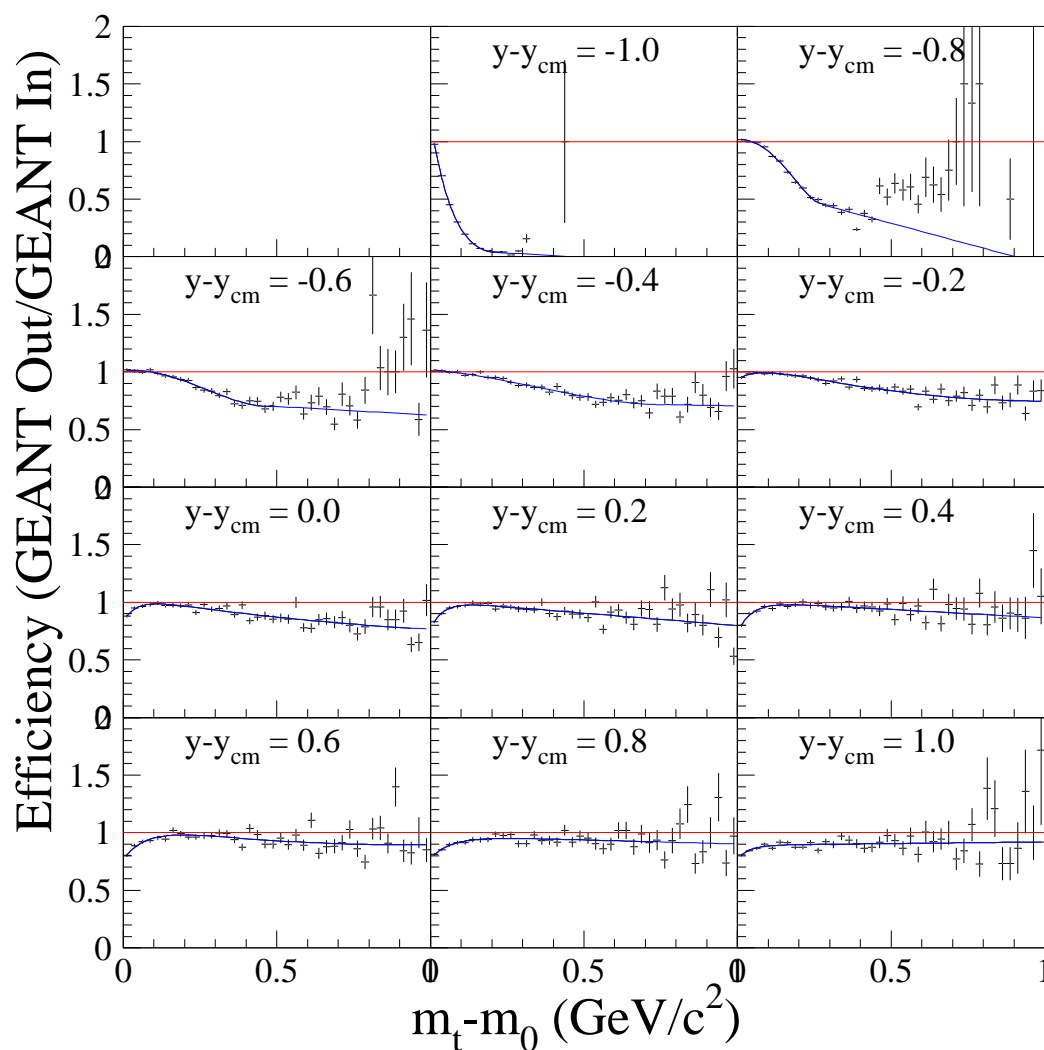Figure D.7: 4 AGeV Proton Detection Efficiencies with Loss Function (Equation 6.6) fits at each embedded rapidity.
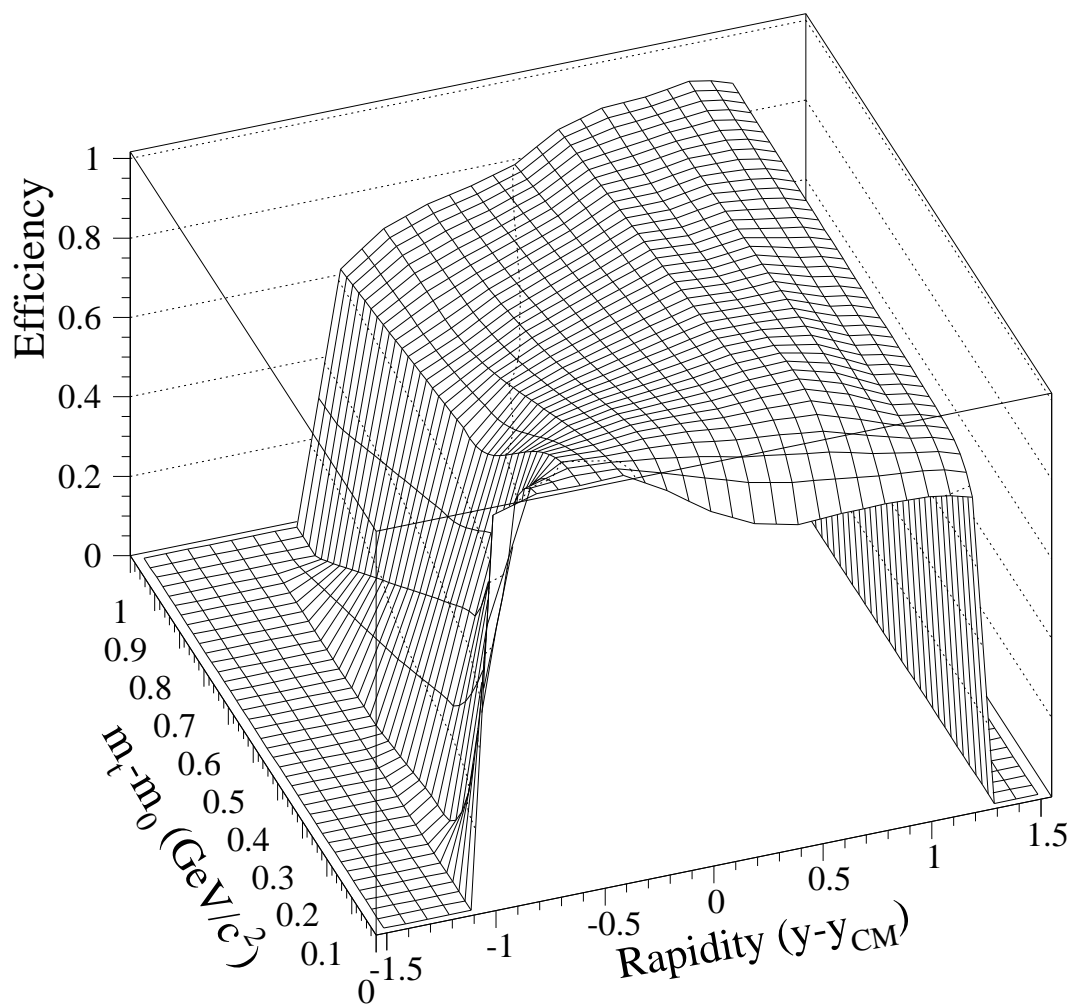
4 AGeV Proton Efficiency

Figure D.8: 4 AGeV Proton Detection Efficiencies as a function of m_t-m_0 and rapidity.
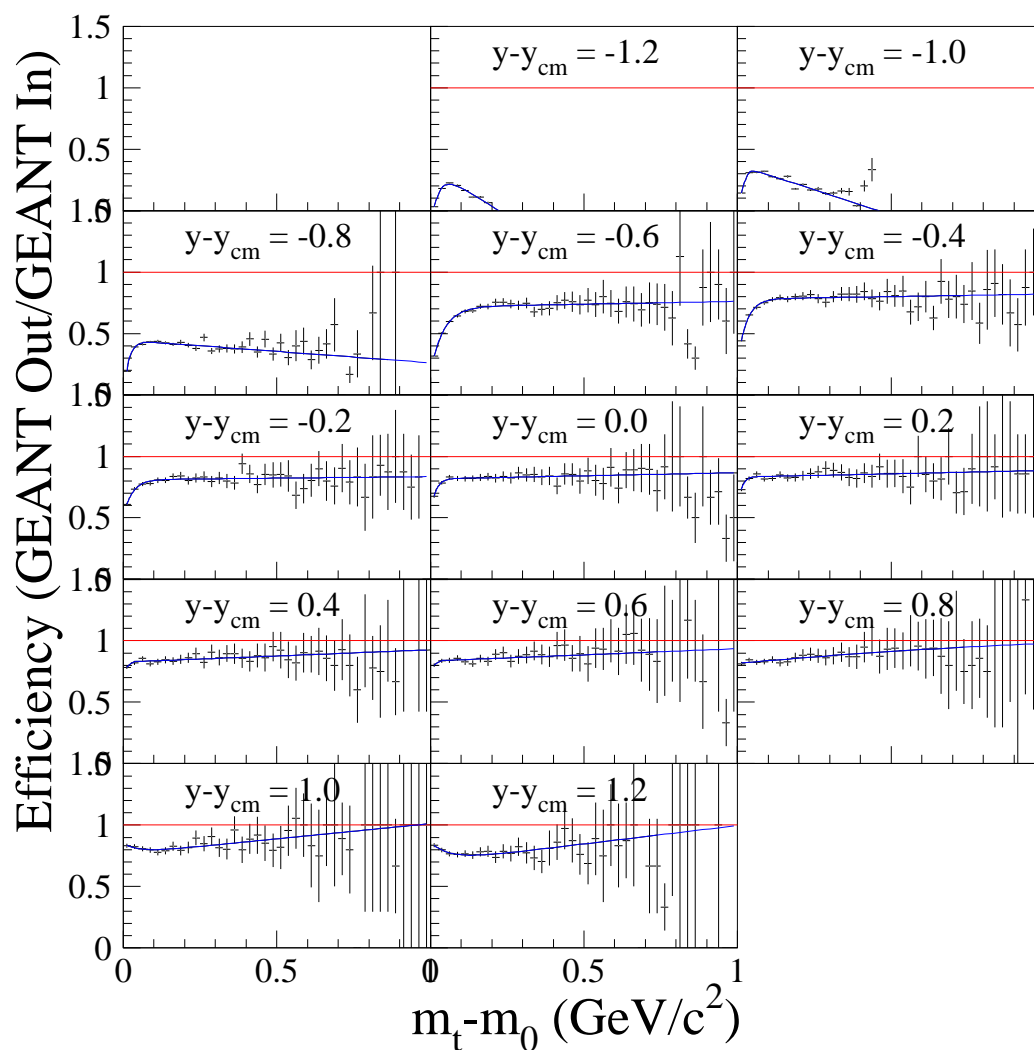
6 AGeV Pion Efficiency

Figure D.9: 6 AGeV Pion Detection Efficiencies with Loss Function (Equation 6.6) fits at each embedded rapidity.
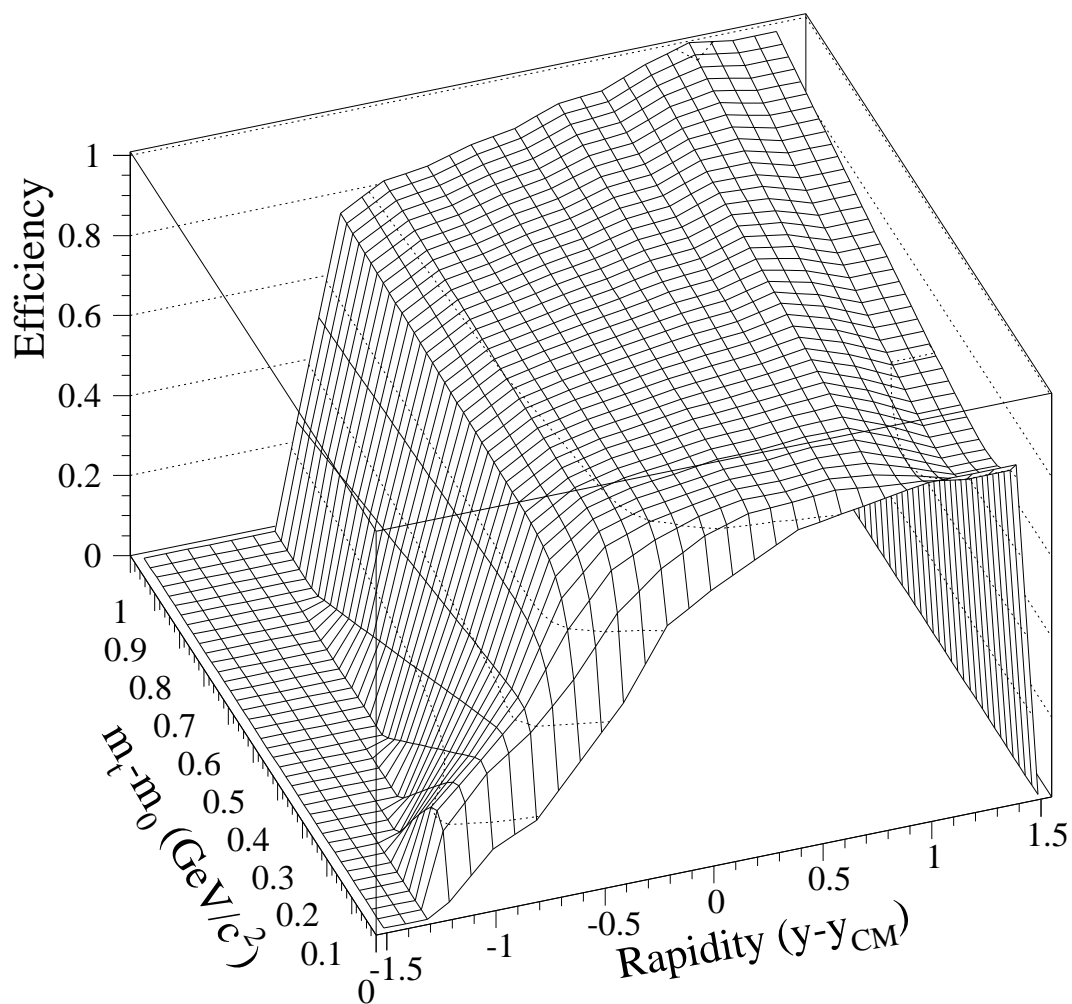
6 AGeV Pion Efficiency

Figure D.10: 6 AGeV Pion Detection Efficiencies as a function of m_t-m_0 and rapidity.

6 AGeV Proton Efficiency
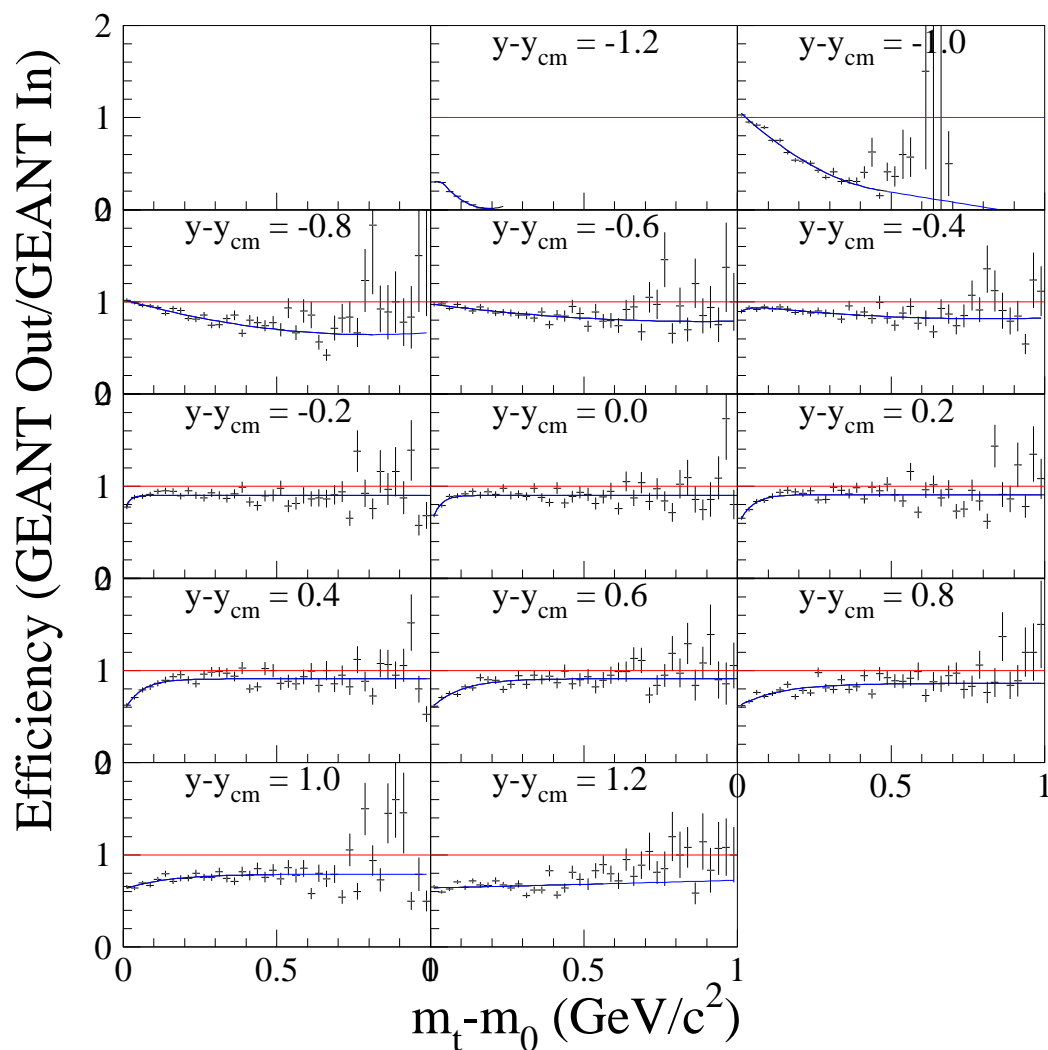

Figure D.11: 6 AGeV Proton Detection Efficiencies with Loss Function (Equation 6.6) fits at each embedded rapidity.
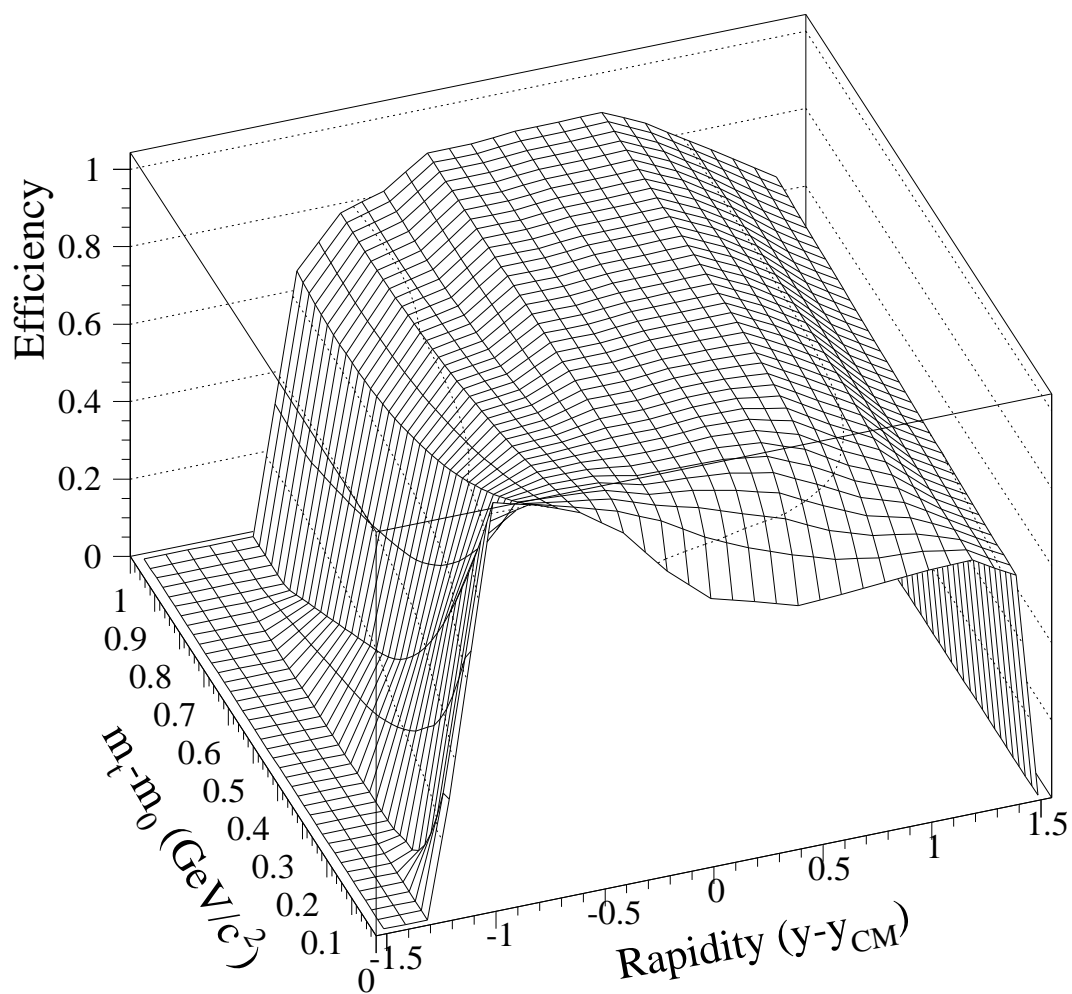
6 AGeV Proton Efficiency

Figure D.12: 6 AGeV Proton Detection Efficiencies as a function of m_t-m_0 and rapidity.

8 AGeV Pion Efficiency

Figure D.13: 8 AGeV Pion Detection Efficiencies with Loss Function (Equation 6.6) fits at each embedded rapidity.

8 AGeV Pion Efficiency

Figure D.14: 8 AGeV Pion Detection Efficiencies as a function of m_t-m_0 and rapidity.
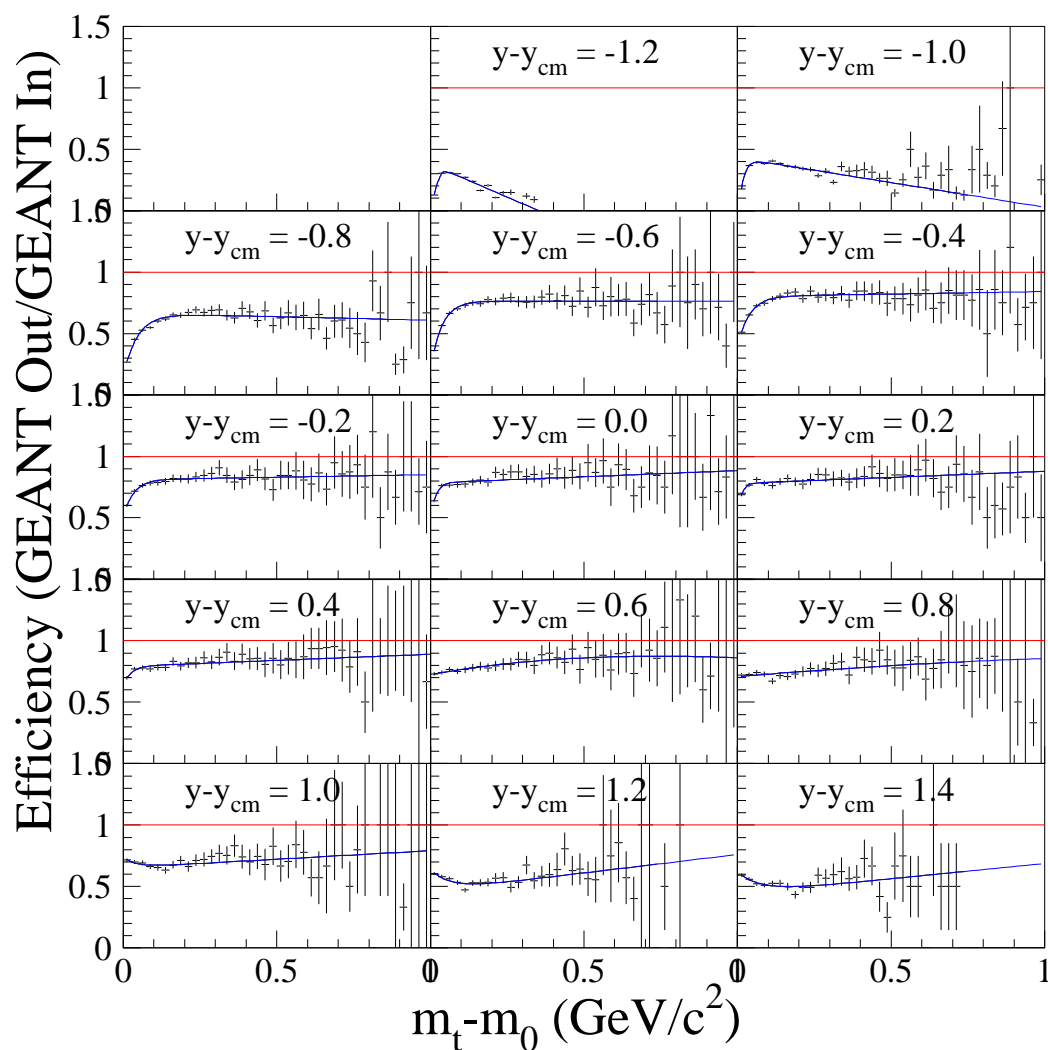
Figure D.15: 8 AGeV Proton Detection Efficiencies with Loss Function (Equation 6.6) fits at each embedded rapidity.
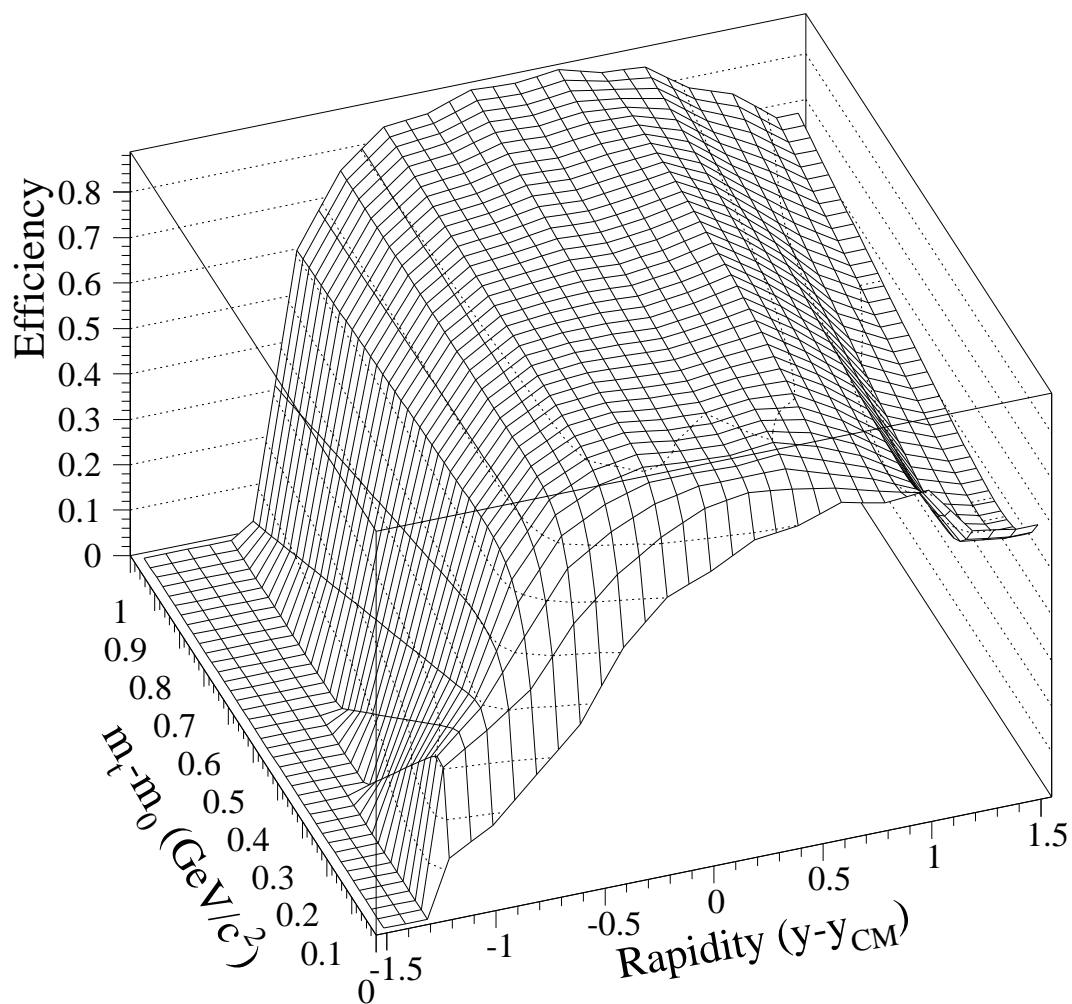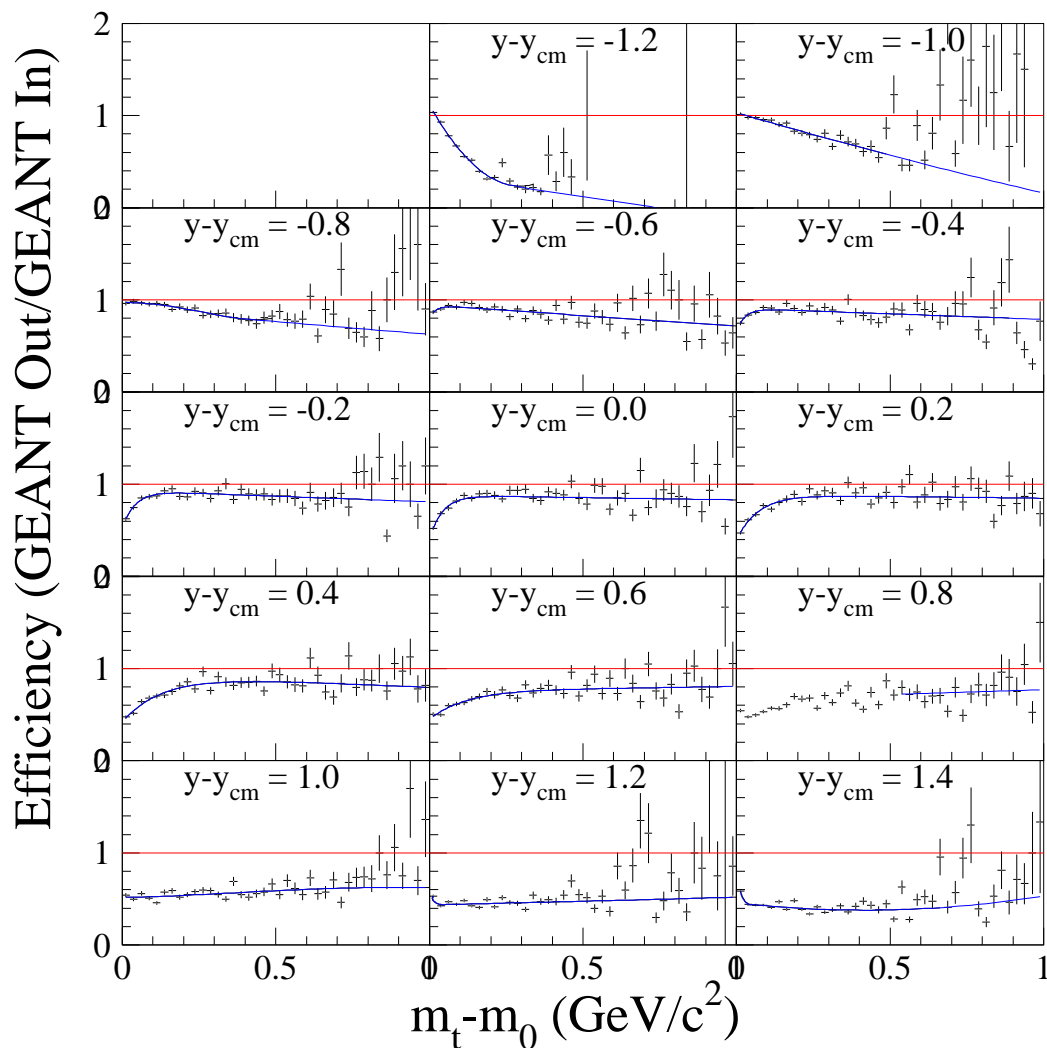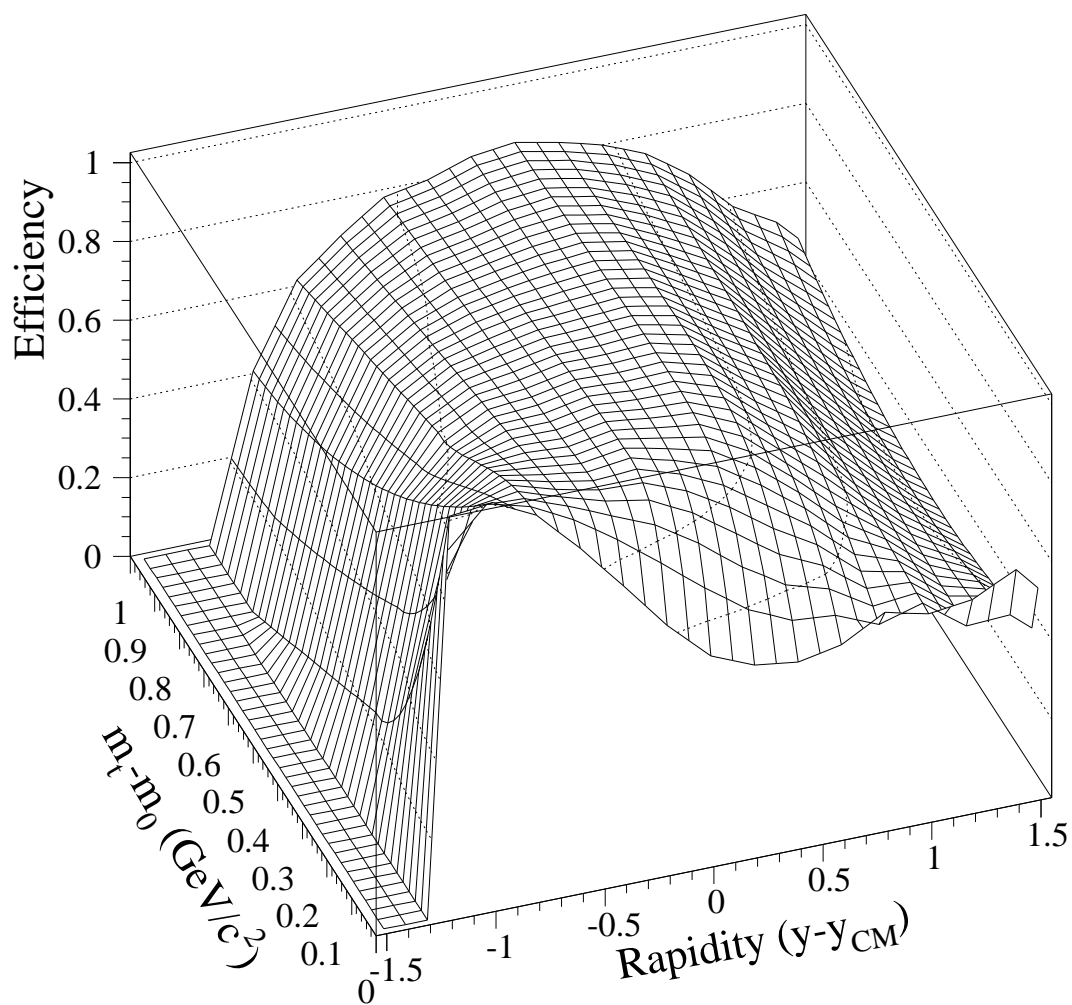
8 AGeV Proton Efficiency

Figure D.16: 8 AGeV Proton Detection Efficiencies as a function of m_t-m_0 and rapidity.

Bibliography

[Ahle00] L. Ahle, *et al.* (E886/E917 Collaborations), Phys. Lett. B **476**, 1 (2000)

[Alli80] W.W.M Allison and J.H. Cobb, Ann. Rev. Nucl. Sci. **30**, 253 (1980)

[Appe99] H. Appelshäuser, *et al.*, (NA49 Collaboration), Phys. Rev. Lett. **82**, 2471 (1999)

[Ayal99] Alejandro Ayala, Sangyong Jeon and Joseph Kapusta, Phys. Rev. C **59**, 3324 (1999)

[Bäch94] J. Bächler, *et al.*, (NA35 Collaboration), Phys. Rev. Lett. **72**, 1419 (1994)

[Back00] B.B. Back, *et al.* (PHOBOS Collaboration), Phys. Rev. Lett. **85**, 3100 (2000)

[Back01] B.B. Back, *et al.* (E917 Collaboration), Phys. Rev. Lett. **86**, 1970 (2001)

[Barn96] R.M. Barnett *et al.* (Particle Data Group), Phys. Rev. **D54**, 1 (1996)

[Barr94] J. Barrette, *et al.* (E814 Collaboration), Phys. Rev. **C50**, 3047 (1994)

[Barz98] H.W. Barz, J.P. Bondorf, J.J. Gaardhøje, and H. Heiselberg, Phys. Rev. C **57**, 2536 (1998)

[Bass98] S.A. Bass *et al.*, Prog. Part. Nucl Phys. **41** 225 (1998)

[Baue97] G. Bauer, *et al.*, Nucl. Instr. and Meth. **A386**, 249 (1997)

[Bjor83] J.D. Bjorken, Phys. Rev. **D27**, 140 (1983)

[Blum94] W. Blum and L. Rolandi, *Particle Detection with Drift Chambers* (Springer-Verlag, New York 1994)

[Blum95] T. Blum, *et al.*, Phys. Rev. D **51**, 5153 (1995)

[Brad98] P. Brady, J. Dunn, Eur. Phys. J. C **5**, 357 (1998)

[Brau95] P. Braun-Munzinger, J. Stachel, J.P. Wessels, N. Xu, Phys. Lett. **B 344**, 43 (1995)

[Busz84] Wit Busza and Alfred S. Goldhaber, Phys. Lett. **139B**, 235 (1984)

[Cask99] W.P. Caskey, Ph.D. Dissertation, University of California, Davis, 1999

[Cebr99] Private communications between D. Cebra and the E866 Collaboration. (1999)

[Cebr01] D.A. Cebra, *et al.*, (E895 Collaboration), *Manuscript in preparation.* (2001)

[Coop74] F. Cooper, G. Frye, Phys. Rev. D **10**, 186 (1974)

[Chri87] W.B. Christie, *et al.*, Nucl. Instr. and Meth. **A255**, 466 (1987)

[Dobl99] Harald Dobler, Josef Sollfrank, Ulrich Heinz, Phys. Lett. B **457**, 353 (1999)

[Dunl99] J.C. Dunlop, Ph.D. Dissertation, Massachusetts Institute of Technology, 1999

[Dunn97] J.W. Dunn, Ph.D. Dissertation, University of California, Davis, 1997

[Ferm50] E. Fermi, Prog. Theor. Phys. **5**, 570 (1950)

[Fern86] R. Fernow, *Introduction to Experimental Particle Physics* (Cambridge University Press, New York 1986)

[Gaźd95a] Marek Gaźdicki, Dieter Rörich, Z. Phys. C **65**, 215 (1995)

[Gaźd95b] Marek Gaźdicki, Z. Phys. C **66**, 659 (1995)

[GEAN94] Application Software Group, *GEANT User's Guide*, CERN (1994)

[Gyul81] M. Gyulassy and S.K. Kauffmann, Nucl. Phys. **A362**, 503 (1981)

[Hage73] R. Hagedorn, Cargese Lectures in Physics, VI, ed. E Schatzmann, 643 (Gordon & Breach, N.Y., 1973)

[Heff00] M. D. Heffner, Ph.D. Dissertation, University of California, Davis, 2000

[Herr99] Norbert Herrmann, Johannes P. Wessels, and Thomas Wienold, Annu. Rev. Nucl. Part. Sci. **49**, 581 (1999)

[Herr96] N. Herrmann, FOPI Collaboration, Nuc. Phys. **A610**, 49c (1996)

[Hiej97] Hiejima, Hiroyoshi for the E910 Collaboration, Poster given at Quark Matter 1997 in Tsukuba, Japan, titled π *Production in p+A Collisions at the AGS*, available at http://www.phy.bnl.gov/~e910/html/phys/qm97/qm97poster_hh.ps.gz (1997)

[Hofm95] M. Hofmann, R. Mattiello, H. Sorge, H. Stöcker, and W. Greiner, Phys. Rev. C **51**, 2095 (1995)

[Hong98] B. Hong, *et al.*, (FOPI Collaboration), Phys. Rev. C **57**, 244 (1998)

[Jone96] P.G. Jones and the NA49 Collaboration, Nuc. Phys. **A610**, 188c (1996)

[Land44] L.D. Landau, J. Phys. USSR **8**, 201 (1944)

[Land53] L.D. Landau, Izv. Akad. Nauk SSSR, Ser. Fiz. **17**, 51(1953)

[Leo94] W.R. Leo, *Techniques for Nuclear and Particle Physics Experiments, 2nd rev. ed.* (Springer-Verlag, New York 1994)

[Li95] Bao-An Li, Phys. Lett. B **346**, 5 (1995)

[Liko92] D. Liko, Star Note 0087, http://www.star.bnl.gov/ (1992)

[Lisa95] M.A. Lisa, *et al.*, (EOS Collaboration), Phys. Rev. Lett. **75**, 2662, (1995)

[Lisa96] M.A. Lisa, Star Note 0238, http://www.star.bnl.gov/ (1996)

[Lisa98] M.A. Lisa, *Output from the RQMD code at E895 energies*, http://vdgus1.mps.ohio-state.edu/~e895/RQMD/ (1998)

[Lisa00] M.A. Lisa, *et al.*, (E895 Collaboration), Phys. Rev. Lett. **84**, 2798 (2000)

[Liu98] H. Liu, *et al.*, (E895 Collaboration), Nucl. Phys. A **630**, 549c (1998)

[Lohse] T. Lohse and W. Witzeling, The Time Projection Chamber, European Organization for Nuclear Research, C.E.R.N., 1211 Geneva 23, Switzerland

[MPS95] R. Hackenburg, *MPS Users Information Page,* http://physgi01.phy.bnl.gov/~mps1/welcome_mps.html, Brookhaven National Laboratory (1995)

[Osad96] T. Osada, S. Sano, M. Bijyajima, and G. Wilk, Phys. Rev. C **54**, 54 (1996)

[Pugh86] H.G. Pugh, G. Odyniec, G. Rai and P. Seidl, EOS: A Time Projection Chamber for the Study of Nucleus-Nucleus Collisions at the Bevalac, **LBL-22314** (1986)

[Rai90] G. Rai *et al.*, IEEE Trans. Nucl. Sci. **37**, 56 (1990)

[Reis97] W. Reisdorf and H.G. Ritter, Annu. Rev. Nucl. Part. Sci. **47**, 663 (1997)

[Salm93] R.A. Salmeron, Nucl. Phys. B **389**, 301, (1993)

[Schn93] Ekkard Schnedermann, Josef Sollfrank and Ulrich Heinz, Phys. Rev. C **48**, 2462 (1993)

[Seyb01] Peter Seyboth, (NA49 Collaboration), Electronic Proceedings of the 17th Winter Workshop on Nuclear Dynamics, Park City, Utah, March 10-17, 2001 http://theo08.nscl.msu.edu/winterworkshop/proceedings/toc.htm (2001)

[Siem79] P.J. Siemens and J.O. Rasmussen, Phys. Rev. Lett. **42**, 880 (1979)

[Soll90] Josef Sollfrank, Peter Koch and Ulrich Heinz, Phys. Lett. B **252**, 256 (1990)

[Stac96] J. Stachel, Nucl. Phys. A **610**, 509c (1996)

[Stoc86] R. Stock, Phys. Rep. **135**, 259 (1986)

[Stöc86] H. Stöcker and W. Greiner, Phys. Rep. **137**, 277 (1986)

[Scot95] A. Scott, PhD Dissertation, Kent State University (1995)

[STAR92] STAR Conceptual Design Report, PUB-5347 (1992)

[STAR00] *STAR Hypernews Particle Identification Forum*, http://coburn.star.bnl.gov/HyperNews-star/get/pid.html (2000)

[Ster71] R.M. Sternheimer and R.F. Peierls, Phys. Rev. **B3**, 3681 (1971)

[VanH82] L. Van Hove, Phys. Lett. B **118**, 138 (1982)

[Vavi57] P.V. Vavilov, Sov. Phys. JETP **5**, 749 (1957)

[Vide95] F. Videbæk, Ole Hansen, Phys. Rev. C **52**, 2684 (1995)

[VerW82] B.J. VerWest and R.A. Arndt. Phys. Rev. C **25**, 1979 (1982)

[Wein98] W. Weinhold, B. Friman, W. Nörenberg, Phys.Lett. B **433** (1998)

[Wess97] J.P. Wessels, *Flow Phenomena at AGS Energies*, Talk at the Workshop 'QCD Phase Transitions', Hirschegg, Austria, January 13-18, 1997 (Available at the Los Alamos pre-print server: http://xxx.lanl.gov/ps/nucl-ex/9704004)

[Witt99] R. Witt, *et al.*, (E895 Collaboration), Proc. of the Relativistic Heavy Ion Minisymposium at the Centennial Meeting of the American Physical Society, Atlanta, Georgia, March 1999, ed. R. Seto (World Scientific, Singapore, 1999), p. 297

[Wong94] Cheuk-Yin Wong, *Introduction to High-Energy Heavy-Ion Collisions*, World Scientific (1994)